$CaCO_3$ CRYSTALLIZATION INFLUENCED BY ADDITIVES AND TEMPLATES

by

Qiaona Hu

A dissertation submitted in partial fulfillment
of the requirements for the degree of
Doctor of Philosophy
(Geology)
in The University of Michigan
2011

Doctoral Committee:

Professor Udo Becker, Chair
Professor James De Yoreo
Professor Rodney C. Ewing
Assistant Professor Gregory J. Dick
Associate Professor Hui Henry Teng

DEDICATION

To my parents, Zhili Hu and Liyun Han

ACKNOWLEDGEMENTS

I would like to express my gratitude to my dissertation committee chairperson, Udo Becker, for giving me the opportunity to study with him at the University of Michigan. He led me to the field of computational simulation meanwhile giving me continued support to explore other research areas. I am also grateful to my other two dissertation advisors, Jim De Yoreo and Henry Teng, for their constant support and patience, and their expertise and insights in the field of carbonate mineralization. They gave me great advice not only on research but also on how to live a fuller life. I am deeply influenced by their commitment to scientific exploration, their passion for life and their congeniality and generosity towards students and colleagues. I am also thankful to my other academic advisors both past and present, Rod Ewing, Youxue Zhang and Greg Dick, for their inspirational comments during my dissertation research. I would like to thank Jiaming Zhang, who generously shared with me the entire skill set of TEM operation and TEM sample preparation heavily relied upon in Chapters Two and Three of this dissertation. I would like to thank Mike Nielsen, Jinhui Tao, Debin Wang and Adam Wallace, who helped me on experiment design, FTIR operation and statistic data analysis, discussed in Chapter Four. Thanks also go to Fuxiang Zhang for his insight on XRD skills used in Chapter Two.

Thanks to all my fellow students and friends, especially Elizabeth Anderson Ferriss, Subhashis Biswas, Devon Renock, Jianwei Wang, Maik Lang, Kai Sun, Weixing

Li, Lindsay Shuller, Frannie Skomurski, Artur Deditius, Darius Dixon, Sandra Fernando, McLain Pray, Anna-Gay Nelson and Zsolt Rak at the University of Michigan, and Alejandro Fernandez-Martinez and Alexander Gagnon at the Lawrence Berkeley National Laboratory. They gave me not only invaluable scientific advice but also the sense of a community of like-minded scientists. I would not have got where I am without the long-term support from Anne Hudon and other office staff. They helped me on a myriad of issues, ranging from student registration and CPT to fellowship applications and tax returns, which have been of immense help to an international student.

Finally, I would like to express my greatest gratitude to my parents, Zhili Hu and Liyun Han. They have given me the most generous love and support I can ever ask for. Whenever I encounter difficulties, they are always there for me. I dedicate my dissertation to my parents.

TABLE OF CONTENTS

LIST OF FIGURES

LIST OF TABLES

ABSTRACT

$CaCO_3$ CRYSTALLIZATION INFLUENCED BY ADDITIVES AND TEMPLATES

by

Qiaona Hu

Chair: Udo Becker

Carbonate mineralization is a crucial topic for underground CO_2 storage and is instrumental for understanding the fundamental thermodynamics of crystallization. This thesis studies both the nucleation process and the development of polymorphs and morphologies of calcium carbonate ($CaCO_3$) precipitates in the presence of ammonium and on self-assembled monolayers (SAMs), in order to gain insight into how additives and templates control the mineralization.

Three polymorphs of $CaCO_3$ exist, and calcite is the most stable one while vaterite is the least stable one. However, if ammonium is present in the growth solution and its concentration is higher than a certain threshold (0.02 mol/L in this study), the formation of vaterite is strongly promoted and the vaterite crystals can be stabilized for as long as one month. Fourier transform spectroscopy (FTIR) studies further suggest that on

ammonium is incorporated into vaterite but not into calcite, implying that ammonium may serve as growth inhibitor of calcite. A semi-quantitative calculation based on experimental analysis demonstrates that the substitution of ammonium into vaterite structure is up to about 0.1 wt%.

The vaterite grains induced by ammonium are polycrystals, displaying a hexagonal layered morphology. The study of the development of this type of vaterite demonstrates that vaterite has a different growth mechanism than calcite. The growth of calcite is a layer-by-layer mechanism, governed by the addition of a single calcium and carbonate ions on kink sites along the growth step. However, vaterite development lacks this organized molecular attachment scheme. Instead, it proceeds by the aggregation of nano-clusters of a couple of nanometers. In the early stage of development, nano-clusters arrange together with random crystallographic orientations. This polycrystalline structure possesses a higher resistance to ionizing irradiation than calcite single crystals that tend to suffer radiation damage. As crystallization continues, the nano-clusters adjust their relative crystallographic orientations and align with each other into a more parallel arrangement.

The thermodynamic and kinetic barriers of calcite nucleation were evaluated on two types of SAMs, monolayers of 16-mercaptohexadecanoic acid (MHA) and 11-mercaptoundecanoic acid (MUA). In addition, whether the nucleation occurs via amorphous precursors during templating was analyzed. The experimental results reveal that (1) MHA and MUA both significantly reduce the effective surface energy of calcite from about 97 mJ/m^2 in solution to about 80 mJ/m^2 on both MHA and MUA, demonstrating that the preferred (012) and (013) orientations of calcite are caused by a

kinetic preference; and (2) at solute activities below the solubility limit of amorphous calcium carbonate, calcite forms directly without using ACC as a precursor.

CHAPTER ONE
INTRODUCTION

The motivation for the topic of this thesis stems from the importance to understand the relationships between the carbon cycle, biomolecular environments, and the climate of the Earth. Carbonate minerals represent the largest carbon reservoir and the most reactive biochemical deposits on the Earth's surface. Carbonate formation in the ocean, facilitated by marine organisms, influences geochemical processes in many aspects [1]. More importantly, in the threat of global warming, geological CO_2 sequestration becomes increasingly important as a potential method to reduce CO_2 emission. The transformation from CO_2 to stable carbonate minerals in deep aquifers is significant to geological CO_2 sequestration in the long term [2, 3]. Among the carbonates, calcium carbonate ($CaCO_3$) is the most abundant and widespread mineral, strongly associated with organic materials [4, 5]. $CaCO_3$ also has wide applications in industries such as cement, paper-making, and oil-field drilling fluids [6, 7]. For both biomineralization and industrial applications, the polymorphism and morphology of $CaCO_3$ are significant properties, which decide many other physicochemical properties such as thermodynamic stability, density, shape, mechanical strength, and solubility [8]. Elucidating the factors that promote certain polymorphs and morphologies, as well as their growth mechanism and structural characteristics will expand our knowledge on the mechanism of biomineralization and may improve the engineering applications of

vaterite as an industrial material [5, 9].

There are three major polymorphs of $CaCO_3$, calcite, aragonite, and vaterite. Calcite is the thermodynamically most stable phase at ambient conditions. However, vaterite, the least stable polymorph, can be induced and stabilized under certain conditions. In nature, vaterite has been found strongly correlated with biogenic activities. Its occurrences have been documented in fresh-water cultured pearls from mussels [10], organic tissues like gallstones, or human heart valves [11, 12]. Under laboratory conditions, vaterite can be produced in highly supersaturated Ca^{2+}-CO_3^{2-}-containing solutions [8, 13-17] or in the presence of certain organic additives and organic templates [18-26].

However, little attention has been paid to the role of inorganic molecules that may occur in solution in controlling polymorphism and morphologies. One example for such a process is the focus of Chapter two. The function of ammonium on polymorph selection of $CaCO_3$ and the role of different reaction vessel materials on $CaCO_3$ polymorph promotion have been investigated. Ammonia is a common inorganic molecule both in experimental setups under laboratory conditions and in natural environments, such as in soils with extensive protein decomposition and sewage treatment plants that nitrifying bacteria frequently associate with [27]. A traditional method of slowly diffusing NH_3 gas into Ca^{2+}- and CO_3^{2-}-containing solution is used to increase pH, resulting in the exclusive growth of calcite crystals of large size [28]. The general principle is that the diffused NH_3 increases the pH of the solution, thus increasing the carbonate concentration, and $CaCO_3$ precipitates when reaching supersaturation [29]. Very few studies describe that the ammonium in gas-diffusion experiments may play a

significant role in selecting $CaCO_3$ polymorphs, *e.g.*, by promoting vaterite formation, even in the absence of organic molecules [30]. Even in these few studies, it was not discussed to what degree ammonium is incorporated in the vaterite crystals and what role the concentration of ammonium plays. In Chapter two, the potential of ammonium for inducing vaterite formation, and the role of different reaction vessel materials on $CaCO_3$ polymorph promotion are being investigated.

Vaterite produced under various experimental conditions render different characteristics for vaterite crystallization, such as growth kinetics and crystal stability, among which the morphology may be the most uncertain one because it displays a great deal of variety. The most intensively reported morphology is the spherical shape [31, 32]. Many others, such as fried-egg shape, flower-like shape, and hexagonal flake shape are also frequently observed [20, 30, 33]. However, how these morphologies develop, what the texture of the resultant crystals is, and what the different shapes have in common remains to be addressed. In chapter two, vaterite induced by ammonium possesses a special morphology that displays 6-fold and looks like a flaky flower. In chapter three, the crystallographic characteristics and growth process of this type of vaterite are investigated.

Besides the polymorphism, organic additives and templates also govern the orientation of minerals growing on them. Researchers have long suspected that living organisms use special organic matrices to guide the crystallographic orientations of minerals, which are most easily controlled during the nucleation stage, for example, the cases of shells of bird eggs [34] and bones [35]. The biomaterials have biological functions as diverse as structural support, grinding and cutting, light harvesting, sound

hearing, and gravity sensing [36].

In recent years, biomineralization science has evolved from being collection of observations, into insights of mechanism such as the stereochemical relationships between template and mineral surface [37, 38]. Since real organic systems are extremely complicated, a simple model, SAMs (an organic thin film of organized amphiphilic molecules), is intensively used to obtain a solid understanding of how organisms control mineralization. Its individual molecule has one end of alkane-thiol to adsorb to {111} surfaces of gold, and the other end is terminated with carboxyl, hydroxyl, or amine moieties which are common functional groups in organic systems. It has been heavily reported that SAMs terminated by carboxylic groups favor the nucleation on non-natural faces [39].

A common explanation for control over nucleation by organic templates is that the interfacial energies of certain nucleation faces are minimized by the template [40-43]. However, the hypothesis that the interfacial energies of calcite are reduced by SAMs has not been proven by any experimental work yet. In Chapter four, the kinetic and thermodynamic controls imposed by two SAM matrices on the calcite nucleation and the resulting phase evolution at early times in the nucleation process are studied. Specifically, the differences in the precipitate density, interfacial energies for odd vs. even carbonyl number as in 16-mercaptohexadecanoic acid (MHA) and 11-mercaptoundecanoic acid (MUA) SAMs were analyzed.

Since no direct measurement technique is available to determine the interfacial energy, we used an indirect approach to evaluate the interfacial energy by measuring

nucleation rates (J_n) as a function of the supersaturation (σ) [44, 45].

The crystallization pathway controlled by organic templates is another unsolved topic. It has been reported that under some biomineralization conditions, the amorphous calcium carbonate (ACC) forms as the precursor of other more stable phases of $CaCO_3$ [46-50]. It is an ongoing debate whether ACC always forms as a transition phase at the early stage of crystallization, or ACC only develops under certain environmental growth conditions, such as high Ca^{2+} and CO_3^{2-} concentrations or high pH (*i.e.*, high supersaturations), which are the most likely conditions under which ACC formation has been observed [8, 51, 52]. In chapter four, the range of supersaturation within which ACC would form on MHA and MUA was analyzed in order to detect whether there is a certain threshold of supersaturation of salt solution for ACC to form on SAMs.

References

1. Berner, R.A. and J.W. Morse, *Dissolution kinetics of calcium carbonate in sea water; IV, Theory of calcite dissolution.* Am J Sci, 1974. **274**(2): p. 108-134.
2. OBES, *Basic research needs for geosciences: facilitating 21st century energy systems* 2007, Department of Energy, Office of Basic Energy Sciences: Bethesda, Maryland.
3. Xu, T.F., J.A. Apps, and K. Pruess, *Numerical simulation of CO_2 disposal by mineral trapping in deep aquifers.* Applied Geochemistry, 2004. **19**(6): p. 917-936.
4. Lowenstam, H.A., *On biomineralization / Heinz A. Lowenstam, Stephen Weiner*, ed. S. Weiner. 1989, New York :: Oxford University Press.
5. Braissant, O., et al., *Bacterially induced mineralization of calcium carbonate in terrestrial environments: the role of exopolysaccharides and amino acids.* Journal of sedimentary research, 2003. **73**(3): p. 485-490.
6. Hadiko, G., et al. *Influence of inorganic ion on the synthesis of hollow calcium carbonate*. in *Asian International Conference on Advanced Materials*. 2005. Beijing, People's R China: Trans Tech Publications Ltd.

7. Fuchigami, K., Y. Taguchi, and M. Tanaka, *Synthesis of calcium carbonate vaterite crystals and their effect on stabilization of suspension polymerization of MMA.* Advanced Powder Technology, 2009. **20**(1): p. 74-79.
8. Kitamura, M., *Crystallization and transformation mechanism of calcium carbonate polymorphs and the effect of magnesium ion.* Journal of Colloid and Interface Science, 2001. **236**(2): p. 318-327.
9. Lian, B., et al., *Carbonate biomineralization induced by soil bacterium Bacillus megaterium.* Geochimica et Cosmochimica Acta, 2006. **70**(22): p. 5522-5535.
10. Addadi, L., et al., *Mollusk shell formation: A source of new concepts for understanding biomineralization processes.* Chemistry-a European Journal, 2006. **12**(4): p. 981-987.
11. Kanakis, J., et al., *The crystallization of calcium carbonate on porcine and human cardiac valves and the antimineralization effect of sodium alginate.* Journal of Crystal Growth, 2001. **223**(4): p. 557-564.
12. Lowenstam, H. and D. Abbott, *Vaterite: a mineralization product of the hard tissues of a marine organism (Ascidiacea).* Science, 1975. **188**(4186): p. 363-365.
13. Kasuga, T., et al., *Preparation of poly(lactic acid) composites containing calcium carbonate (vaterite).* Biomaterials, 2003. **24**(19): p. 3247-3253.
14. Ogino, T., T. Suzuki, and K. Sawada, *The formation and transformation mechanism of calcium carbonate in water.* Geochimica et Cosmochimica Acta, 1987. **51**(10): p. 2757-2767.
15. Kralj, D., L. Brecevic, and J. Kontrec, *Vaterite growth and dissolution in aqueous solution III. Kinetics of transformation.* Journal of Crystal Growth, 1997. **177**(3-4): p. 248-257.
16. Colfen, H. and M. Antonietti, *Crystal design of calcium carbonate microparticles using double-hydrophilic block copolymers.* Langmuir, 1998. **14**(3): p. 582-589.
17. Grasby, S.E., *Naturally precipitating vaterite (μ-$CaCO_3$) spheres: unusual carbonates formed in an extreme environment.* Geochimica et Cosmochimica Acta, 2003. **67**(9): p. 1659-1666.
18. Fujiwara, M., et al., *Encapsulation of Proteins into CaCO3 by Phase Transition from Vaterite to Calcite.* Crystal Growth & Design, 2010. **10**(9): p. 4030-4037.
19. Didymus, J.M., et al., *Influence of low-molecular-weight and macromolecular organic additives on the morphology of calcium carbonate.* Journal of the Chemical Society-Faraday Transactions, 1993. **89**(15): p. 2891-2900.
20. Heywood, B.R., S. Rajam, and S. Mann, *Oriented crystallization of $CaCO_3$ under compressed monolayers. 2. morphology, structure and growth of immature crystals.* Journal of the Chemical Society-Faraday Transactions, 1991. **87**(5): p. 735-743.
21. Rieke, P.C., *Selection of phase and control of orientation during physisorption on surfaces of homogeneously formed calcium carbonate nuclei.* Materials Science & Engineering C-Biomimetic and Supramolecular Systems, 1995. **2**(3): p. 181-189.
22. Kun Park, H., I. Lee, and K. Kim, *Controlled growth of calcium carbonate by poly(ethylenimine) at the air/water interface.* Chemical Communications, 2004(1): p. 24-5.

23. Rudloff, J. and H. Colfen, *Superstructures of temporarily stabilized nanocrystalline $CaCO_3$ particles: Morphological control via water surface tension variation.* Langmuir, 2004. **20**(3): p. 991-996.
24. Lee, H.S., T.H. Ha, and K. Kim, *Fabrication of unusually stable amorphous calcium carbonate in an ethanol medium.* Materials Chemistry and Physics, 2005. **93**(2-3): p. 376-382.
25. Jada, A. and A. Verraes, *Preparation and microelectrophoresis characterisation of calcium carbonate particles in the presence of anionic polyelectrolyte.* Colloids and Surfaces A: Physicochemical and Engineering Aspects, 2003. **219**(1-3): p. 7-15.
26. Malkaj, P., J. Kanakis, and E. Dalas, *The effect of leucine on the crystal growth of calcium carbonate.* Journal of Crystal Growth, 2004. **266**(4): p. 533-538.
27. Belser, L.W., *Population ecology of nitrifying bacteria.* Annual Review of Microbiology, 1979. **33**: p. 309-333.
28. Becker, A., et al., *In-vitro crystallization of calcium carbonate in the presence of biological additives - comparison of the ammonium carbonate method with double-diffusion techniques.* Zeitschrift für anorganische und allgemeine Chemie, 2003. **629**(12-13): p. 2305-2311.
29. Addadi, L., et al., *A chemical-model for the cooperation of sulfates and carboxylates in calcite crystal nucleation-relevance to biomineralization* Proceedings of the National Academy of Sciences of the United States of America, 1987. **84**(9): p. 2732-2736.
30. Gehrke, N., et al., *Superstructures of calcium carbonate crystals by oriented attachment.* Crystal Growth & Design, 2005. **5**(4): p. 1317-1319.
31. Watanabe, J. and M. Akashi, *Controlled deposition of calcium carbonate particles on porous membranes by using alternating current system.* Journal of Colloid and Interface Science, 2008. **327**(1): p. 44-50.
32. Han, Y., et al., *Influence of initial $CaCl_2$ concentration on the phase and morphology of $CaCO_3$ prepared by carbonation.* Journal of Materials Science, 2006. **41**(14): p. 4663-4667.
33. Fricke, M., et al., *Vaterite polymorph switching controlled by surface charge density of an amphiphilic dendron-calix[4]arene.* Crystal Growth & Design, 2006. **6**(5): p. 1120-1123.
34. Fernandez, M.S., M. Araya, and J.L. Arias, *Eggshells are Shaped by a Precise Spatio-Temporal Arrangement of Sequentially Deposited Macromolecules.* Matrix Biology, 1997. **16**(1): p. 13-20.
35. Stupp, S.I. and P.V. Braun, *Molecular Manipulation of Microstructures: Biomaterials, Ceramics, and Semiconductors.* Science, 1997. **277**(5330): p. 1242-1248.
36. Mann, S., *Biomineralization: principles and concepts in bioinorganic materials chemistry.* Oxford University Press, Inc., New York,, 2001.
37. Addadi, L. and S. Weiner, *Interactions Between Acidic Proteins and Crystals: Stereochemical Requirements in Biomineralization.* Proceedings of the National Academy of Sciences of the United States of America, 1985. **82**(12): p. 4110-4114.

38. Aizenberg, J., et al., *Crystal progein interactions studied by overgrowth of calcite on biogenic skeletal elements.* Journal of Crystal Growth, 1994. **142**(1-2): p. 156-164.
39. Aizenberg, J., A.J. Black, and G.M. Whitesides, *Control of crystal nucleation by patterned self-assembled monolayers.* Nature, 1999. **398**(6727): p. 495-498.
40. Pokroy, B., V.F. Chernow, and J. Aizenberg, *Crystallization of Malonic and Succinic Acids on SAMs: Toward the General Mechanism of Oriented Nucleation on Organic Monolayers†.* Langmuir, 2009. **25**(24): p. 14002-14006.
41. Duffy, D.M., et al., *Effect of Bicarbonate Ions on the Crystallization of Calcite on Self-Assembled Monolayers.* The Journal of Physical Chemistry B, 2005. **109**(12): p. 5713-5718.
42. Kuther, J., et al., *Templated crystallisation of calcium and strontium carbonates on centred rectangular self-assembled monolayer substrates.* Chemistry-a European Journal, 1998. **4**(9): p. 1834-1842.
43. Han, Y.-J. and J. Aizenberg, *Face-Selective Nucleation of Calcite on Self-Assembled Monolayers of Alkanethiols: Effect of the Parity of the Alkyl Chain.* Angewandte Chemie International Edition, 2003. **42**(31): p. 3668-3670.
44. Travaille, A.M., et al., *Thermodynamics of Epitaxial Calcite Nucleation on Self-Assembled Monolayers.* The Journal of Physical Chemistry B, 2005. **109**(12): p. 5618-5626.
45. De Yoreo, J.J. and P.G. Vekilov, *Principles of Crystal Nucleation and Growth.* Reviews in Mineralogy and Geochemistry, 2003. **54**(1): p. 57-93.
46. Weiss, I.M., et al., *Mollusc larval shell formation: Amorphous calcium carbonate is a precursor phase for aragonite.* Journal of Experimental Zoology, 2002. **293**(5): p. 478-491.
47. Loosanoff, V.L., W.S. Miller, and P.B. Smith, *Growth and setting of larvae of venus-mercenaria in relation to temperature.* Journal of Marine Research, 1951. **10**(1): p. 59-81.
48. Beniash, E., et al., *Amorphous calcium carbonate transforms into calcite during sea urchin larval spicule growth.* Proceedings of the Royal Society of London Series B-Biological Sciences, 1997. **264**(1380): p. 461-465.
49. Politi, Y., et al., *Sea urchin spine calcite forms via a transient amorphous calcium carbonate phase.* Science, 2004. **306**(5699): p. 1161-1164.
50. Colfen, H. and S. Mann, *Higher-order organization by mesoscale self-assembly and transformation of hybrid nanostructures.* Angewandte Chemie-International Edition, 2003. **42**(21): p. 2350-2365.
51. Koga, N., Y.Z. Nakagoe, and H. Tanaka, *Crystallization of amorphous calcium carbonate.* Thermochimica Acta, 1998. **318**(1-2): p. 239-244.
52. Huang, S.C., K. Naka, and Y. Chujo, *A carbonate controlled-addition method for amorphous calcium carbonate spheres stabilized by poly(acrylic acid)s.* Langmuir, 2007. **23**(24): p. 12086-12095.

CHAPTER TWO
INFLUENCE OF AMMONIUM AND GROWTH SUBSTRATES ON $CACO_3$ POLYMORPH FORMATION AND TRANSFORMATION

ABSTRACT: $CaCO_3$ crystals were grown by increasing the pH of Ca^{2+}- and CO_3^{2-}-containing solutions in two ways (and, thus, supersaturating the solution with respect to calcium carbonate), either by diffusing ammonia gas into the solution or by adding 10% NaOH. Both methods were performed in glass and plastic dishes (which, in some cases, served as growth substrates), the latter made of polystyrene. Only calcite precipitated in both glass and plastic Petri dishes when using NaOH to increase pH. However, vaterite was predominantly formed if applying ammonia instead, implying an ability of ammonia to promote vaterite formation. When ammonia was applied, the fractions of vaterite crystallized depended on the material of the growth container with about 60-70% in glass Petri dishes but almost 100% in plastic Petri dishes, indicating the role the substrate plays in selecting the $CaCO_3$ polymorph in the presence of ammonia. The results of Fourier transform spectroscopy (FTIR) indicate that ammonium incorporates into the lattice of vaterite but not into that of calcite. The content of ammonium in vaterite has been estimated in a semi-quantitative way to be about 0.1 wt%. The vaterite formed using this growth method is metastable and it takes more than 10 days for vaterite to transform to calcite in a closed chamber, with or without the presence

of ammonia gas.

2.1. Background

Polymorphs of calcium carbonate ($CaCO_3$) occur widely in nature, and this polymorphism is of interest due to the mineral's widespread precipitation on the Earth's surface under both biological and geologic conditions [1, 2], as well as various industrial applications such as paper-filling and cement [3]. Among the three major polymorphs of $CaCO_3$ (calcite, aragonite, and vaterite), calcite is the thermodynamically most stable phase at ambient conditions. However, vaterite, the least stable polymorph, can be induced and stabilized under certain conditions. In nature, vaterite has been found in the environment associated with organisms, such as fresh-water cultured pearls from mussels, organic tissues like gallstones, or human heart valves [4, 5]. In addition, vaterite may form as a precursor of the other polymorphs calcite and aragonite, or as a transition state between amorphous calcium carbonate (ACC) and the more stable polymorphs [6]. Under laboratory conditions, vaterite can also be produced in highly supersaturated calcium carbonate-containing solutions or in the presence of organic matter [7].

Since the crystallization of vaterite is often closely related to organisms, analyzing vaterite formation will shed light on the mechanisms of biomineralization [1, 8]. In addition, because calcite and vaterite possess different thermodynamic stabilities and physicochemical properties, such as mechanical strength and solubility [9], they are used in different industrial applications. Therefore, understanding which factors will promote vaterite formation and how to control the precipitation of this polymorph is important for understanding the thermodynamics in general and in relation to industrial processes that use calcium carbonate such as the paper and oil industry.

In the past decade, it was found that organic additives and substrates are able to induce less stable $CaCO_3$ polymorphs, which may be a model for selective biomineralization. Many amino acids, peptides, and even larger organic molecules have been reported to be capable of promoting vaterite crystallization, such as aspartic acid, leucine, and octadecylamine monolayers [7, 10-14]. However, the exact mechanism of how organic molecules induce vaterite formation is still unclear. It may be because the Gibbs free energy of the formation of certain vaterite surfaces is decreased by organic molecules through favorable interactions of their functional groups with the atoms on the stabilized face of vaterite [15]. Another reason may be that the charged organic matter increases the rate of vaterite nucleation and growth by increasing the local supersaturation, thereby promoting vaterite formation according to Ostwald's rule [16].

However, little attention has been paid to inorganic molecules that may occur in solution, which is the focus of this study. A traditional method of slowly diffusing NH_3 gas into Ca^{2+}- and CO_3^{2}-containing solution is used to increase pH, resulting in the exclusive growth of calcite crystals of large size [17]. The general principle is that the diffused NH_3 increases the pH of the solution, thus increasing the carbonate concentration, and $CaCO_3$ precipitates when reaching the supersaturation status [18]. Very few studies describe that ammonia in gas-diffusion experiments may play a significant role in selecting $CaCO_3$ polymorphs, *e.g.*, by promoting vaterite formation, even in the absence of organic molecules [19]. Even in these few studies, it was not discussed to what degree ammonium is incorporated in the vaterite crystals and what role the concentration of ammonium plays. In addition, the transformation process of vaterite to calcite in ammonia diffusion experiments has not been dealt with. Ammonia is a

common inorganic molecule both in experimental setups under laboratory conditions and in natural environments, such as in soils with extensive protein decomposition and sewage treatment plants that nitrifying bacteria frequently associate with [20]. Understanding the role of ammonia will further a more comprehensive insight into the process of $CaCO_3$ formation and its kinetics. In this study, the potential of ammonium for inducing vaterite formation, and the role of different reaction vessel materials on $CaCO_3$ polymorph promotion have been investigated.

2.2 Experimental procedures

2.2.1 Crystallization experiments

Calcium carbonates were grown in glass and plastic Petri dishes by increasing pH of calcium carbonate-containing solution by either diffusing ammonia gas or adding 10% NaOH at room temperature, named "case-NH_3" and "case-NaOH", respectively. The salt solution was prepared by feeding 0.002 mol/L concentrations of $NaHCO_3$ and $CaCl_2{\cdot}2H_2O$, followed immediately by acidification using 10% HCl to a pH value of 3.6, at which the solution was undersaturated with respect to all the polymorphs of $CaCO_3$ (calculated using MINTEQ version 2.51 [21]). The acidified solution was well mixed thereafter and let stand for 15 min to reach equilibrium.

For the runs of case-NH_3, three plastic and three glass Petri dishes containing 55 mL salt solution were placed in a sealed 33-liter container with two open beakers of 20 g fresh NH_4HCO_3 powders. The NH_4HCO_3 powders release ammonia gas, which then diffuses into the salt solution and hence gradually increases the pH of the salt solution to promote $CaCO_3$ precipitation as in Eq. (2.1) and (2.2):

$$NH_4HCO_3\ (s) \rightarrow NH_3\ (g) + CO_2\ (g) + H_2O, \quad (2.1)$$

$$NH_3\ (g) \rightarrow NH_3\ (aq),$$

$$H_2O + NH_3\ (aq) \rightarrow NH_4^+\ (aq) + OH^-\ (aq). \quad (2.2)$$

In addition, CO_2 released from ammonium bicarbonate also slowly goes into the solution.

The increase of the pH of the salt solution by diffused NH_3 gas was recorded (Fig. 2.1A) and the experimental setup is shown in Figure 2.2. In order to analyze how much NH_3 and CO_2 gas is produced over time, the weights of the beaker and its containing NH_4HCO_3 powders were measured throughout the experiments.

For the control runs of case-NaOH, the plastic and glass Petri dishes containing 55 mL salt solution were placed in a sealed glove box (2 m^3) filled with pure N_2. Two open Petri dishes containing 20% NaOH were placed in the glove box for absorbing any CO_2 that may potentially exist, which would otherwise decrease the pH of the growth solution. Special attention was given to the fact that the rates of increasing the pH of the salt solution were the same as with the ammonia method in order to avoid potential kinetic differences between the two methods (Fig. 2.1B). During the titration of 10% NaOH, glass rods were used to stir the salt solution in the Petri dishes to uniform the pH.

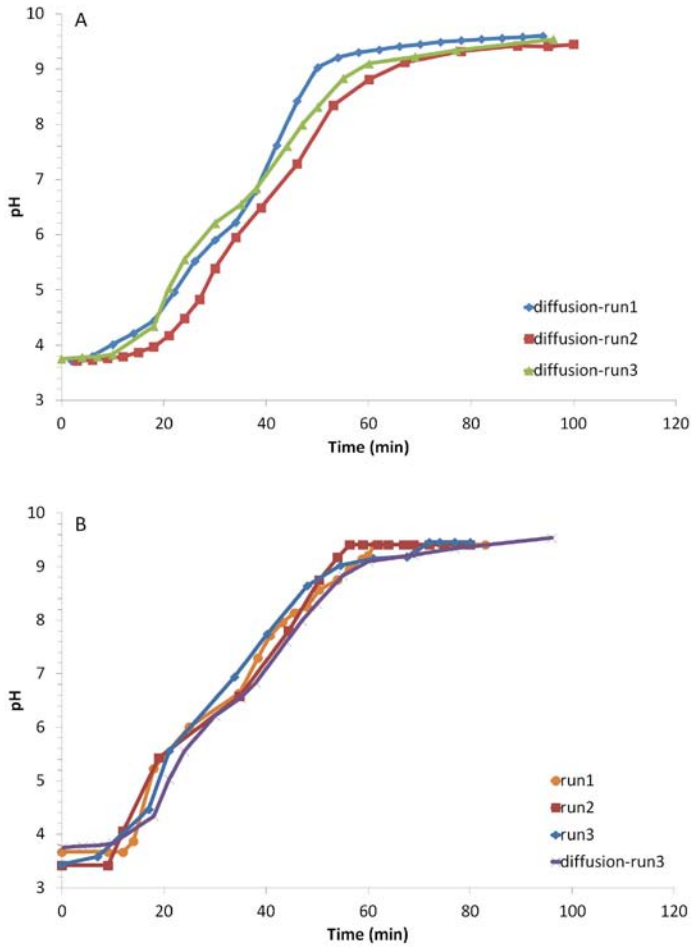

Figure 2.1 (A): Increase of the pH of salt solution over time in the crystallization experiments by the NH_3 diffusion method; (B) Increase of the pH of salt solution by adding NaOH diluted solution. The pH curve of the diffusion method in run 3 is plotted for comparison.

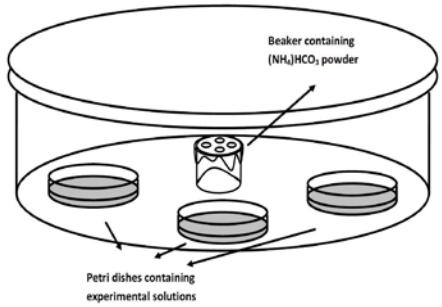

Figure 2.2. Schematic of the experimental setup for NH_3 diffusion method

Both case-NH_3 and case-NaOH growth experiments have been conducted three times each to assure the repeatability of results. Glass and plastic Petri dishes were purchased from Daigger and VWR, respectively. Prior to use, all the Petri dishes and beakers were soaked in 10% HCl for more than 12 hours, followed by rinsing in completely deionized water.

In order to obtain a deeper understanding of the ability of ammonium to promote certain polymorphs, a series experiments was conducted using the NH_3 diffusion method with various amounts of NH_4HCO_3 powder, named "case A", "case B", and "case C". In this set of experiments, we noticed that applying the NH_3 diffusion method does not always lead to a precipitation of a high percentage of vaterite. For example, a high percentage of calcite precipitates when the amount of NH_4HCO_3 applied is as small as a couple of grams, a result that is comparable to a number of studies reported in the literature [8, 17, 22]. This implies that ammonium is able to promote vaterite formation, but only if its concentration exceeds a certain threshold, which will be quantified later. All the other experimental settings were the same as for the NH_3 diffusion method mentioned before, except the amount of NH_4HCO_3 powder. In case A, 20 g NH_4HCO_3 fresh powder were applied, in case B 10 g, and case C 5 g, resulting in different amounts of ammonia gas produced. In order to measure the amount of ammonia that has escaped each beaker, the weights of each beaker and its containing NH_4HCO_3 powders were measured throughout the experiments. Subsequently, the polymorphs of the matured precipitates were analyzed by using both optical microscopy and XRD. Weights of beakers were only measured within the first 72 hours because thereafter, neither pH nor the precipitation changed for up to at least 13 days (after which vaterite starts

transforming to calcite) if the experimental conditions were not changed.

2.2.2 Sample analysis

Salt solutions in the Petri dishes were poured out and rinsed by ethanol. Then the precipitates on the bottom of the Petri dishes were harvest using the wood end of cotton tips. Optical microscopy, scanning electron microscopy (SEM, Hitachi S3200N), transmission electron microscopy (TEM, JEOL 2010F), and X-ray diffraction (XRD) were used to study the precipitated polymorphs. The morphology and polymorphism of the crystals were observed by using optical microscopy in situ every two hours in the first 10 hours and once a day after that for up to one month, and the final morphologies were observed using SEM. In order to study the time of the nucleation, the crystals were harvested on TEM copper grids from the solution and detected by TEM every 30 minutes starting from the beginning until six hours later. The grown crystals were removed carefully by using a clean blade and ground using mortar and pestle until the particle size was less than 1 μm for X-ray analysis. X-ray powder diffraction data were collected using an Enraf Nonius CAD4 diffractometer with a Cu anode and an accelerating voltage of 25 kV over an angular range of 2θ=10–65° and a 0.02 step size with a scanning rate of 2.0 deg/min. The XRD data of vaterite have been refined by using the Rietveld method as implemented in the software packages Fullprof and WinPLOTR [23] for analyzing the cell parameters.

Nitrogen weight percent determinations of both calcite and vaterite were performed on a Costech Elemental Analyzer ECS 4010 coupled to a Finnigan Delta V Plus mass spectrometer. Acetanilide with known nitrogen weight percent of 10.36% was used to calibrate the runs. Three samples of calcite and vaterite were analyzed,

respectively, around 4 mg each.

The crystals for FTIR analysis were soaked in 1% HCl for ten seconds to dissolve the outer layers of the crystals to eliminate the adsorbed NH_3 on the crystal surfaces, then rinsed and dried. Unpolarized IR spectra (from 6000 to 400 cm^{-1}) of randomly oriented crystals were taken using the AutoImage microscope system on the Perkin-Elmer Spectrum GX FTIR, with a MIR source, KBr beam splitter, and liquid nitrogen cooled MCT detector for 32 scans. Although no effort was made to orient the crystals, the measured sections were roughly (*001*) surfaces for vaterite due to its natural crystal habit. 35 spectra were taken for both calcite and vaterite each.

2.3 Results

2.3.1 Polymorphic composition

2.3.1.1 Case-NH_3 and case-NaOH

The courses of the pH of the salt solutions by diffusing NH_3 and by adding 1% NaOH are shown in Figure 2.1. Only 0.067 ml NaOH in total was used to increase the pH of each Petri dish solution to 9.6, which is much less than the total volume of the solution in each Petri dish (55 ml). Thus, the solution dilution resulting from the extra volume of NaOH is negligible. Figure 2.1 indicates that within one hour, the growth solution became supersaturated with respect to calcite, aragonite, and vaterite, who, for the given Ca^{2+} and total C concentrations, reach saturation at pH 7.50, 7.64, and 8.06, respectively. The maximum pH value, around 9.6, was reached within one hour and did not change afterwards. Optical microscopy revealed that it took about seven hours for crystals to appear.

In case-NaOH, regardless of the material of the Petri dishes, the crystals precipitating from solution were pure calcite as observed by optical microscopy and SEM analysis (Fig. 2.3 A), as well as corresponding XRD patterns (Fig. 2.4). In case-NH_3, however, under the same experimental condition, vaterite formed predominantly, especially in plastic Petri dishes (Table 2.1; Fig. 2.3 and 2.4).

2.3.1.2 Polymorph ratios as a function of different ammonium bicarbonate amounts

The production speed of NH_3 gas increased with the applied amount of NH_4HCO_3 powder. The final pH is always the same, around 9.6, regardless of the varying amount of NH_4HCO_3 powder applied. The amount of NH_3 evaporating over time can be obtained by the weight reductions of the NH_4HCO_3. Exposed to air, NH_4HCO_3 decomposes into H_2O, CO_2, and NH_3, causing a decrease in weight after the gas phase of CO_2 and NH_3 leave. The amounts of NH_3 and CO_2 gas dissolved in the H_2O that was generated by decomposing NH_4HCO_3 powder can be ignored, since the total amount of this kind of H_2O was very limited before $CaCO_3$ precipitates became fully mature in this study. Therefore, the mole number N of NH_3 produced in a given time can be obtained by Eq. (2.3):

$$N=\Delta m/(M_{NH3}+M_{CO2}), \tag{2.3}$$

where Δm is the reduced mass of the beaker containing NH_4HCO_3 in gram in a given time interval. M_{NH3} and M_{CO2} are the molar masses of NH_3 and CO_2, respectively.

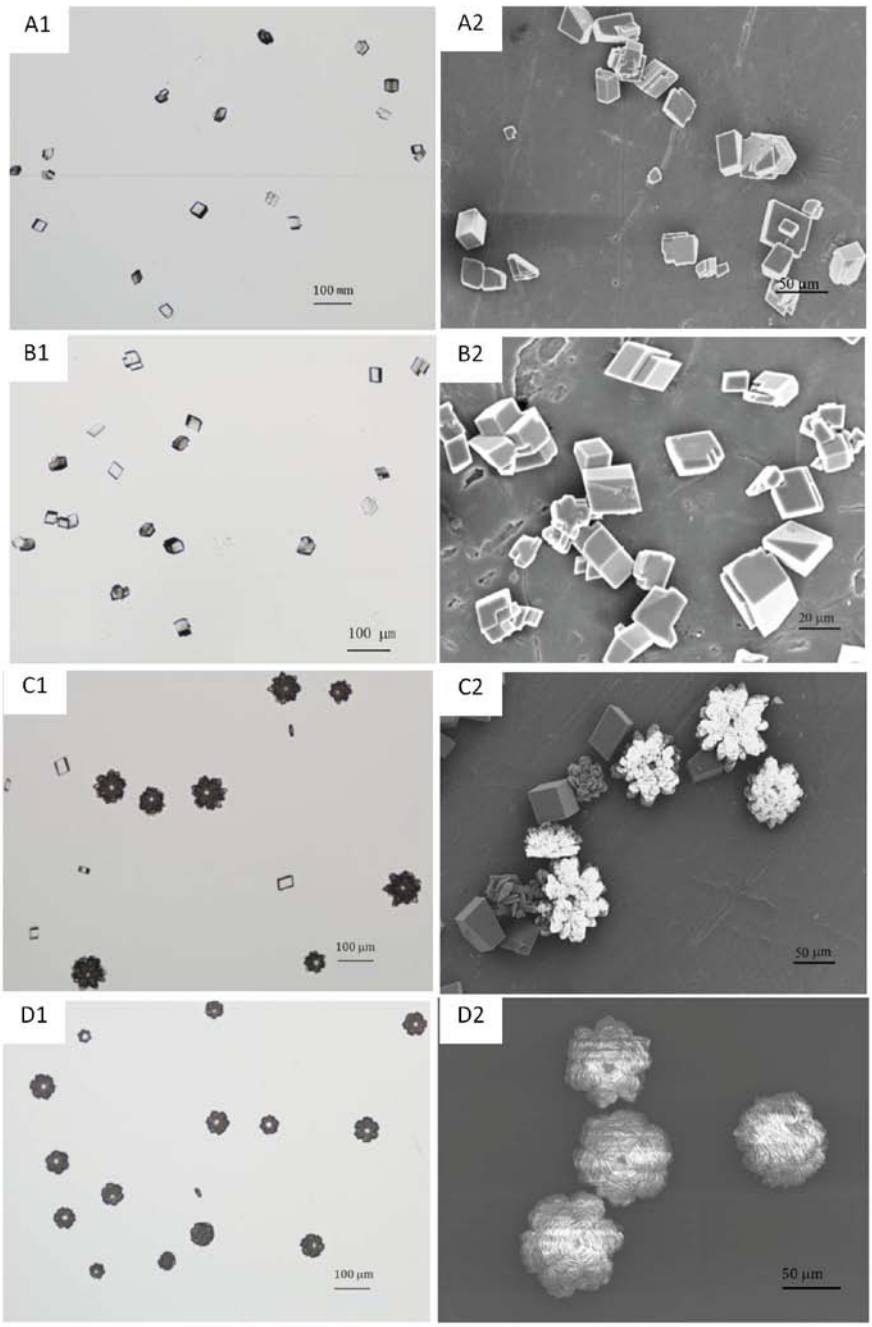

Figure 2.3 Optical and SEM images of $CaCO_3$ precipitates in different experimental runs. Calcite takes on a rhombohedral shape while vaterite grains display flaky crystal layers with a hexagonal morphology, similar to a 6-petal flower. (A1,A2): applying NaOH and glass Petri dishes, only calcite forms; (B1,B2): applying NaOH and plastic Petri dishes, only calcite forms; (C1,C2): applying ammonia and glass Petri dishes, both vaterite and calcite precipitate; (D1,D2): applying ammonia and plastic Petri dishes, nearly pure vaterite precipitates.

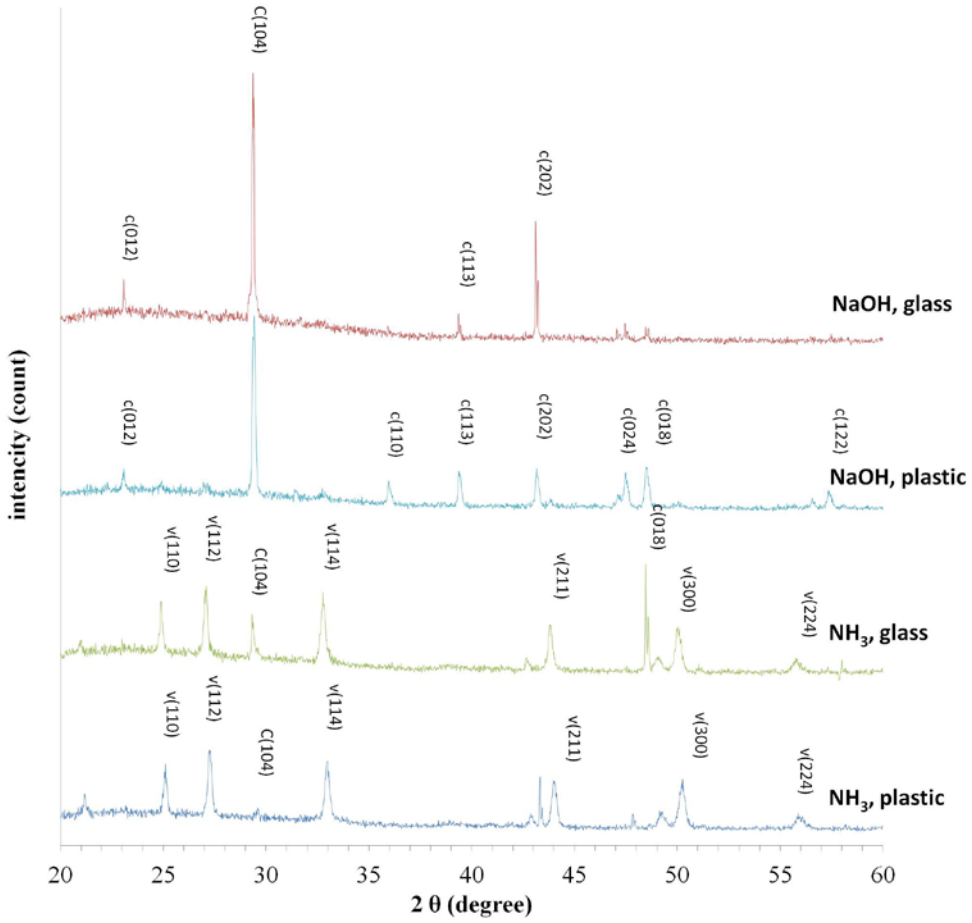

Figure 2.4 XRD patterns of the crystals harvested from different experimental runs, confirming that pure calcite precipitates if applying NaOH to increase the pH. In contrast, in the presence of ammonia, both calcite and vaterite develop in glass Petri dishes, and nearly pure vaterite precipitates in plastic Petri dishes. Numbers in parentheses indicate the Miller indices, and C and V denote calcite and vaterite, respectively.

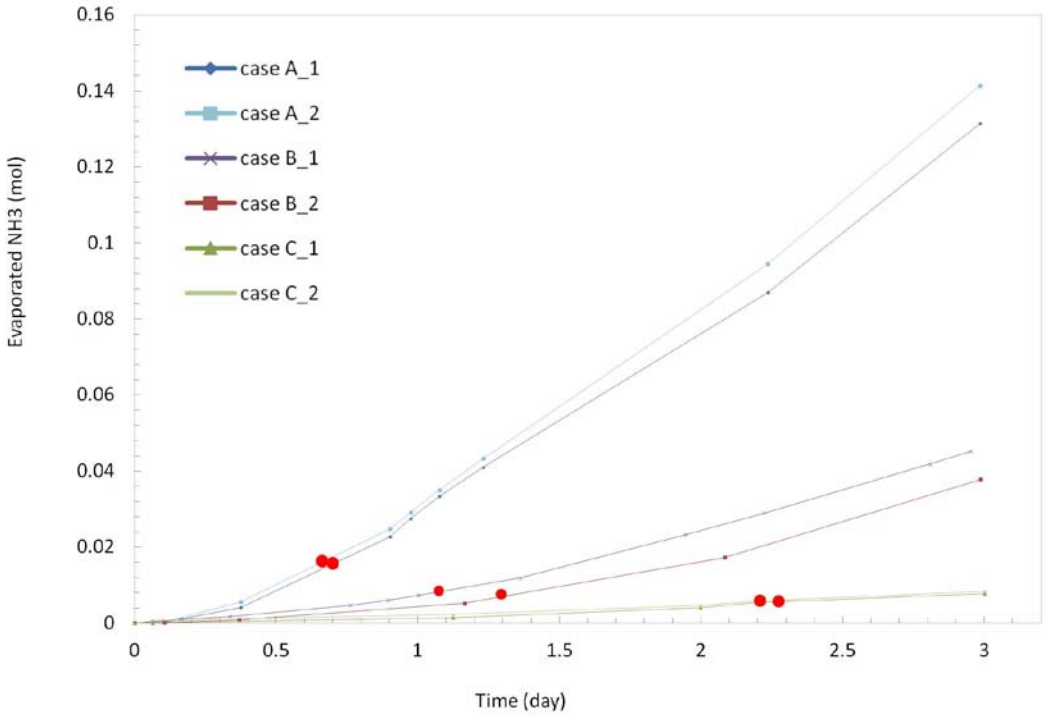

Figure 2.5 Number of moles of NH_3 gas evaporating throughout time in the runs applying NH_3 to increase pH. The red dots on each curve represent the time when $CaCO_3$ crystals matured. For case A, it merely took 16 hours for $CaCO_3$ precipitates to mature, for case B, 23-26 hours, and for case C, 53-54 hours. When the $CaCO_3$ crystals become matured, in case A, 1.7-1.9 10^{-2} mol NH_3 dissolved in the solution, in case B 0.8 -1.0·10^{-2} mol, and in case C only 7.1·10^{-3} mol.

The cumulative amounts of generated NH_3 in each case are illustrated in Figure 2.5. The curves of the two repeating runs in each case do not superpose well. Such lack of agreement may be due to the slightly-different exposure areas of the NH_4HCO_3 powder in the two runs. The decomposition rate of NH_4HCO_3, and hence the increase of pH of the salt solution, increases with NH_4HCO_3 powder's surface area, which is very difficult to keep the same in different runs.

The red dots in each curve represent the time when the $CaCO_3$ crystals "matured", that is, the morphology and size of $CaCO_3$ crystals not changing thereafter. As expected, the evaporated NH_3 increased with the amount of applied NH_4HCO_3. For case A (applying 20 g NH_4HCO_3), it merely took 16 hours for $CaCO_3$ crystals to be fully matured with a total amount of 1.7-1.9$\cdot 10^{-2}$ mol NH_3 produced, for case B (10g), 23-26 hours and 0.8 to 1.0$\cdot 10^{-2}$ mol NH_3 produced, and for case C (5g), 53-54 hours and only 7.1$\cdot 10^{-3}$ mol NH_3 produced.

The amount of dissolved ammonia can be obtained using Henry's law:

$$P/C=k, \tag{2.4}$$

where P is the partial pressure of NH_3 in equilibrium with the salt solution, C is the concentration of NH_3 in solution, and k is the equilibrium constant of ammonia (1.62 Pa m^3 mol^{--1} at 298K and 1 atm).

P and C can be obtained from:

$$P = nRT/V \tag{2.5}$$

$$C = n'/V' \tag{2.6}$$

$$n=N-n', \tag{2.7}$$

where R is the universal gas constant (8.314 $JK^{-1}mol^{-1}$), T is the temperature (298 K), n is the number of moles of NH_3 in the gas phase in the sealed container, V is the volume of the sealed container, 33 L, n' is the number of moles of NH_3 in the liquid phase, V' is the total volume of salt solution in nine Petri dishes, and N is the total number of moles of evaporated ammonia. With n'=0.938 N, 93.8% of the NH_3 gas dissolves in the solution. Therefore, before the crystals matured, the salt solutions absorbed the most NH_3 in case A (0.048-0.054 mol/L), and the precipitations had the highest percentage of vaterite (97%-100%). Salt solutions in case B absorbed medium amounts of NH_3 (0.022-0.028 mol/L), with the precipitations of a moderate percentage of vaterite (50% for the glass substrate and 65% for the plastic substrate on average). Salt solutions in case C absorbed the least amount of NH_3 (0.02 mol/L), with precipitations of the smallest percentage of vaterite (5% for glass substrate and 45% for plastic substrate on average).

2.3.2 Morphology and crystallography of the grown vaterite

The vaterite grains in this study display a layered structure with the "leaves" or "petals" arranged in a 6-fold symmetry, different from the commonly-observed spherical morphology that has been frequently reported [24, 25]. The SEM images in high magnification further show that each petal, about 10-20 μm in diameter, is not a single crystal but composed of smaller hexagonal pieces about 1 μm in diameter (Fig. 2.6).

The cell parameters obtained from XRD measurements show that the vaterite crystallizes in space group $P6_3/mmc$, with unit-cell parameters a = b = 4.1358(1) Å, c= 8.478(1) Å. This result is close to Kamhi's work that states that vaterite possesses the $P6_3/mmc$ space group with unit-cell parameters a = b = 4.13 Å, c = 8.49 Å [26].

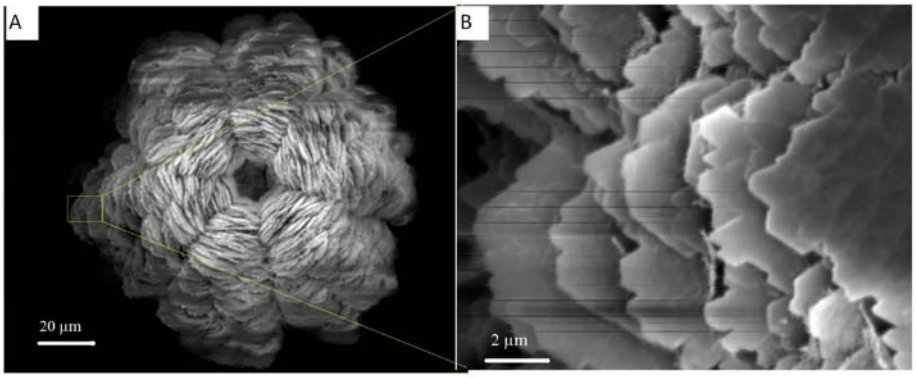

Figure 2.6 SEM images of a typical vaterite grain, showing a 6-fold symmetry and layered structure. Large (≈10 μm) terraces are composed of small hexagonal sheets (≈1 μm).

2.3.3 FTIR and total nitrogen analysis results

Total nitrogen analysis using a Costech Elemental Analyzer did not detect any nitrogen in either vaterite or calcite crystals, indicating the nitrogen concentrations are less than the detection limit of this technique which is about 1.0 wt% meaning that ammonium concentrations are lower than 1.3 wt% in both $CaCO_3$ polymorphs.

All 35 FTIR spectra of vaterite crystals have similar patterns, but the peak heights vary slightly from one another, which may be attributed to the different orientations of the crystal flakes. FTIR spectra of calcite also show similar patterns but different intensities, which may be due to the various thicknesses of calcite crystals. Since the outer layers of the crystals have been dissolved by diluted HCl before FTIR analyses, the adsorbed species (such as NH_4^+) which may be concentrated at the solid surfaces were removed. Thus, the bands displayed in the FTIR patterns indicate the chemistry of the bulk crystal instead of the chemistry on the surface. However, because vaterite is polycrystalline, it is possible that some ammonium is concentrated on the grain-boundaries between the crystallites. Spectra of both vaterite and calcite (Fig. 2.7) display the characteristic carbonate out-of-plane bending υ2, symmetric stretching υ1, asymmetric stretching υ3 and υ1+ υ3 bands at 876 cm^{-1}, 1086 cm^{-1}, 1438cm^{-1}, and 2508-2517cm^{-1}, respectively. The characteristic carbonate in-plane bending υ4 band appears in calcite FTIR patterns at 714cm^{-1} and 2 υ3 bands at 2877 cm^{-1} and 2986 cm^{-1}. The specific vaterite υ4, υ1+ υ4, and 2 υ3 bands can be observed at 744 cm^{-1}, 1837 cm^{-1} and 2975 cm^{-1}, respectively. These results are consistent with many other studies [27-29]. The two small peaks around 3450 cm^{-1} and 3590 cm^{-1} in the calcite spectra may be due to some minor impurities.

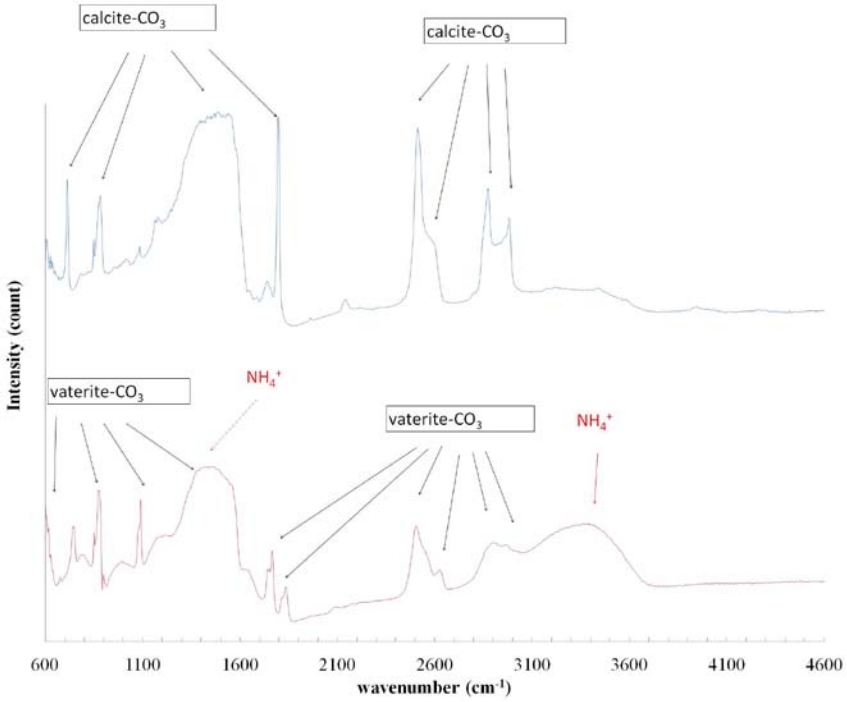

Figure 2.7 Typical FTIR patterns of calcite and vaterite. The FTIR pattern of calcite only displays the carbonate characteristic peaks, while the pattern of vaterite also shows NH_4^+-stretching bands around 3150-3400 cm^{-1}. The NH_4-bending bands (1400 and 1430 cm^{-1}) cannot be distinguished from the FTIR patterns, since they are overlaid by carbonate stretching bands.

Case In addition to the special carbonate bands of vaterite, characteristic vibration bands of ionic ammonium were observed in FTIR spectra of vaterite. NH_4^+ peaks are located in two major ranges of wave numbers [27, 30], one is around 1430 to 1400 cm^{-1}, corresponding to bending ($\upsilon 4$) in NH_4^+; and the other is around 3150-3400 cm^{-1}, corresponding to a series of N-H stretching ($\upsilon 1$, $\upsilon 3$, $\upsilon 2 + \upsilon 4$, $2\upsilon 2$) plus bending overtone ($2\upsilon 4$) in NH_4^+. Unfortunately, the NH_4-bending peaks overlap with strong carbonate stretching peaks. Hence, only the peaks around 3150-3400 cm^{-1} are used to determine the presence of ammonium. These peaks occur in the vaterite spectra but not in the calcite ones, demonstrating that there is ammonium in vaterite but not in calcite.

2.3.4 Stability of vaterite in the presence of ammonium

After the precipitates matured, the Petri dishes were either kept in the chamber filled with NH_3 gas or moved to another closed chamber filled with pure N_2 gas to eliminate the potential influence of NH_3 on $CaCO_3$ polymorph stabilities. The vaterite in the solution in both environments remained stable for more than ten days without any transformation to calcite, which is much longer than the time reported in the literature (ranging from a couple of minutes to four days, depending on whether vaterite is synthesized from highly supersaturated $Ca\text{-}CO_3$ solutions or by adding organic additives) [14, 24, 25, 31]. The duration for which vaterite was stable were somewhat different between the crystals grown in plastic or glass dishes. In plastic Petri dishes, after the crystals matured, transformation from vaterite to calcite did not start until the 13rd day. About sixteen days after the vaterite matured, 10 % of vaterite had transformed to calcite, after 22 days 20%, and after 29 days, all carbonate was calcite. In a glass Petri dish, vaterite was even more stable, in that it did not transfer at all for at least 15 days, and

about 20 days after the vaterite matured, 10% of it had transformed to calcite, after about 23 days 20%, and after about 40 days 95%.

2.4 Discussion

2.4.1 Vaterite growth induction and stabilization by ammonia

In order to understand the mechanism of how ammonia may influence or control surface and bulk stability and the resulting choice of polymorph for carbonate growth, it is necessary to understand the pathway on how ammonia is transported into the Petri dishes. At least four steps are involved: 1) decomposition of NH_4HCO_3 results in the release of NH_3 (and CO_2) gas; 2) NH_3 transport through air to the area of the Petri dishes; 3) NH_3 dissolution into solution at the air-liquid interface simultaneous NH_3 conversion to NH_4^+ depending on the pH; and 4) NH_3 and NH_4^+ diffusion (with possible convection) to the bottom of the Petri dishes where precipitation takes place. In order for ammonia to promote $CaCO_3$ precipitation, it needs to be able to reach the Petri dish bottom before $CaCO_3$ matures. In addition, since NH_3 or NH_4^+ bond differently to minerals, the ratio between the two affects $CaCO_3$ crystallization.

The time for NH_3 gas diffusing from the beaker to the Petri dishes, as well as the time from the surface to the bottom of the solution can be expressed by Fick's law (Eq. 2.8)

$$x=(Dt)^{1/2}. \tag{2.8}$$

Here, t is the diffusion time, D is the diffusion coefficient, and x is the diffusion distance. For NH_3 diffusion in the gas phase, D is $2.2\text{x}10^{-5}$ m^2/s at 298 K [32], and the distance, x, between the beakers and the Petri dishes, is 5 cm. Hence, even without

convection, NH_3 gas can diffuse from the beaker with NH_4HCO_3 powder to the solution in 2 minutes. For NH_3 diffusion in the liquid phase (the fourth stage), x is the height of solution in the Petri dishes, 5mm, and D is $1.64 \cdot 10^{-9}$ m^2/s [32]. Thus, dissolved NH_3 takes 4 hours to diffuse from the top to the bottom of the Petri dish. The interface reaction for ammonia dissolution in water is assumed instantaneous here.

Altogether, it takes NH_3 less than four hours to transfer to the site of $CaCO_3$ crystallization by pure diffusion, and it will be much shorter if convection takes place in addition to diffusion. Fig. 2.1 shows that in case-NH_3, the pH value reaches a plateau in about 60 minutes (shorter than 4 hours); thus, convection does enhance mass transport of ammonia and ammonium in the solution. Thus, the total transportation time is less than the time for $CaCO_3$ crystals to appear (7 hours according to the optical-microscopy results in case-NH_3). Among all the experiments using the NH_3 diffusion method, NH_3 gas was produced the quickest in case-A (exposure to four Petri dishes with NH_4HCO_3 powder), *i.e.*, $CaCO_3$ takes the shortest time to form, so in the slower exposure experiments (cases B and C), NH_3 also reaches the site of precipitation before $CaCO_3$ actually forms. Therefore, a significant portion of NH_3/NH_4^+ can potentially affect $CaCO_3$ crystallization.

The protonated form (NH_4^+) and free ammonia (NH_3) co-exist in chemical equilibrium, which is determined by pH, and the equilibrium constant, K_{eq}, as described in Eq. (2.9):

$$NH_4^+ \leftrightarrow NH_3 + H^+ \qquad K_{eq} = \frac{[NH_3][H^+]}{[NH_4^+]} \tag{2.9}$$

The equilibrium constant K_{eq} for this reaction is $10^{-9.25}$ at room temperature [33], thereby $[NH_3]/[NH_4^+] = (10^{-9.25})\cdot(10^{pH})$. Using TEM analysis, no nucleation was observed until one hour after the pH reached the final value of 9.6. At this pH, NH_3 and NH_4^+ are in equilibrium and the $[NH_4^+]/[NH_3]$ ratio is 0.44 in solution, indicating that the amounts of NH_4^+ and NH_3 are of the same order during nucleation and crystallization.

In order to understand the influence of the growth methods on the selection of the respective polymorph, we compare addition of NaOH solution with the addition of ammonia to increase pH and supersaturate the solution with respect to calcium carbonate. There is a difference in chemistry and potentially a difference in other factors, such as kinetics of alkalinization. However, in order to minimize kinetic effects, NaOH titration was performed in such a way that the pH increase rate was the same as with the NH_3 diffusion method. Thus, differences in solution chemistry are only due to the presence of NH_3. Chemical differences caused by adding 10% NaOH can be neglected, because Na^+ already existed in the reagent (0.002M $NaHCO_3$), and adding 10% NaOH contributes a Na^+ concentration increase of only $1.78\cdot10^{-6}$ M. Table 2.1 and 2.2 show that in experimental conditions that were the same except for the titrating agent, the precipitation was pure calcite when using the NaOH method, whereas substantive amounts of vaterite were formed when NH_3 was applied. Interestingly, aragonite, even though more thermodynamically than vaterite at ambient conditions, made up less than 1 % of the grown calcium carbonate. This implies that the addition of ammonia plays an important role in inducing and stabilizing vaterite and, thus, selecting a specific carbonate polymorph. Other studies have already established that soluble additives are able to promote certain crystals growth while inhibit the others [34-38]. Additives can influence

crystallization in general through two ways, either by interacting with the crystal surface (*e.g.*, by blocking kink sites or by stabilizing surface steps [39, 40], or by being incorporated into the crystal lattice [35]).

Table 2.1. Polymorphic composition of precipitation in different experimental runs

run type		**proportion %**		
		calcite	vaterite	aragonite
NaOH	glass	100	0	0
	plastic	100	0	0
NH_3	glass	30-40	60-70	0
	plastic	0-2	98-100	0

* "NaOH" and "NH_3" denote increasing pH through adding 10% NaOH and diffusing ammonia respectively. "glass" and "plastic" stand for applying glass Petri dish and plastic Petri dish respectively.

Table 2.2 Proportion of vaterite of the precipitates due to different evaporation rates of NH_3

run type	**vaterite percentage***					
	run 1			run2		
	glass-1	glass-2	glass-3	plastic-1	plastic-2	plastic-3
case A_1	100	97	97	100	100	100
case A_2	99.9	97	100	100	99.9	100
case B_1	70	75	80	95	98	98
case B_2	10	50	15	60	30	10
case C_1	5	15	1~2	60	55	55
case C_2	5	~0.5	5	60	15	30

* the remaining percentage was calcite with very little aragonite produced.

In light of the results using different ammonia exposures (case A, B, and C), it becomes apparent that the proportion of vaterite among the precipitation increased in conjunction with the total dissolved N-species before $CaCO_3$ crystals matured. In addition, ammonia/ammonium was only able to induce vaterite formation when the concentration of dissolved N-species is sufficiently high. In case C, when the accumulated N-species in the salt solution is as low as 0.02 mol/L when precipitation matures, calcite is the predominant phase. This phenomenon confirms the possibility of the formation of pure calcite by using the NH_3 diffusion method. Low NH_3 concentrations in previous studies are a likely cause of high percentages of calcite precipitation by diffusing NH_3 into $Ca\text{-}CO_3$ containing solutions.

2.4.2 Incorporation of ammonium into vaterite

To study the specific mechanism of how ammonia promotes vaterite formation and to what degree it is present in the grown carbonate, FTIR analysis was used to detect the existence and estimate the amount of the incorporated ammonia in the bulk of vaterite and calcite.

The FTIR results demonstrate that vaterite, but not calcite, incorporates NH_4^+ as evidenced by characteristic NH_4^+ stretching peaks that only appear in the FTIR spectra of vaterite. Peaks characteristic for NH_4^+ are located in two regions of the IR spectra, one around 1400 to 1430 cm^{-1} corresponding to the bending in NH_4^+, and another one around 3150-3400 cm-1corresponding to N-H stretching in NH_4^+ [27, 30]. Since the NH_4^+-bending peaks overlap with strong carbonate stretching peaks, the stretching peaks around 3150-3400 cm^{-1} are used to estimate the concentration of ammonium. The FTIR

patterns shown in Figure 2.7 reveal the existence of NH_4^+ in vaterite, but not in calcite crystals.

In addition to the confirmation of the existence of ammonium in the vaterite structure, the amount of ammonium in the lattice was roughly estimated. Because no calibration for ammonium in vaterite is available (and vaterite crystals are not oriented), ammonium concentration quantification in biotite calibrated using unpolarized IR spectra by Busigny et al. [27] was used to estimate semi-quantitatively the ammonium content in vaterite. This calibration is based on the linear correlation between the NH_4^+ content/crystal thickness and the absorbance, and there is no need for accurate thickness measurements. The Busigny method works best for host minerals 50 to 150 μm thick. Figure 2.3 C2 shows that the vaterite grains are about 50-60 μm thick and hence qualify for this method. In Eq. (7) of Busigny et al. [30]:

$$[NH_4^+](\text{ppm}) = 2 \times 1044.3 \times \frac{\mathbf{A}^{1086} - \mathbf{A}^{2367}}{\mathbf{A}^{3384} - \mathbf{A}^{2367}} - 320, \qquad (2.10)$$

A^{1086}, A^{3384}, and A^{2367} are absorbances corresponding to wavenumbers 1086 cm^{-1} (CO_3^{2-} vibration), 3384 cm^{-1} (NH_4^+ stretching), and 2367 cm^{-1} (spectrum baseline), respectively. Because the NH_4^+ bending peak at 1430 cm^{-1} used in the Busigny paper overlaps with carbonate stretching peaks, we chose the absorbance of NH_4^+ stretching vibration ν3 to bridge the concentration of NH_4^+ in vaterite instead. Since the absorbance at 3384 cm^{-1} is roughly half of the one at 1430 cm^{-1} in Busigny et al. [30], a factor '2' has been multiplied to correct for this peak sensitivity. All 35 FTIR patterns have been analyzed this way and the calculated ammonium concentrations per unit thickness range from 0.06

wt% to 0.10 wt% in vaterite, which is consistent with the result of total nitrogen analysis in this study that the ammonium concentration is lower than 1.3 wt%.

The uncertainty in the above semi-quantitative results is unknown, since the crystal structure, composition, and properties of vaterite are different from those of biotite. Nonetheless, linear molar absorptivities do not vary significantly from one phase to another. For example, linear molar absorptivities based on unpolarized IR spectra for O-H basic stretching are 8.8 L/(mol·mm) for rhyolite glass [41], 6.1 L/(mol·mm) for basalt glass [42], and 9.7 L/(mol·mm) for garnet [43], varying within a factor of 2. Another source of error may be due to the variable orientation of vaterite flakes in FTIR analyses. The SEM images reveal that many vaterite (*001*) flakes were not perpendicular to the IR beam. Nonetheless, our results indicate that ammonium is present in vaterite at a concentration of the order 0.1 wt%.

One reason for why NH_4^+ may not incorporate into the calcite lattice is that the ionic radius difference between NH_4^+ (1.50 Å) [44] and Ca^{2+} (1.00 Å) is larger than 15 % [45], which causes strain when substituting NH_4^+ for Ca^{2+}. However, to some extent, it is possible for NH_4^+ to enter the vaterite structure, since vaterite (2.54 g/cm^3) is less dense than calcite (2.71 g/cm^3) and more disordered [46], especially in terms of carbonate orientation (Wang and Becker, 2009), which makes the vaterite structure more tolerant to accept the additive entries. In addition, in calcite, Ca^{2+} is octahedrally coordinated by O atoms at a distances of 0.236 nm, whereas in vaterite, Ca^{2+} is coordinated by eight O atoms (six O atoms at distances of about 0.23–0.25 nm and two O atoms at 0.29–0.31 nm) [47]. This implies a larger site of Ca^{2+} in vaterite and the ability of vaterite to incorporate larger cations, such as NH_4^+, than calcite. If one NH_4^+ substitutes for one

Ca^{2+} in vaterite, to complement the expansion in size, one H^+ may bond to one CO_3^{2-} forming HCO_3^-, which is in turn smaller than the carbonate anion [45, 48]. Feng et al.[49] did observe HCO_3^- substitutions in both synthesized and natural calcite, and reported that HCO_3^- may balance local charge and accommodate local structure deformation near defects. Based on the discussions above, it is reasonable to suggest that the following coupled substitution may occur in vaterite: $NH_4^+ + HCO_3^- \rightarrow Ca^{2+} + CO_3^{2-}$. This minor substitution of ammonium may reduce the Gibbs free energy of vaterite and hence favor vaterite formation [36]. This hypothesis is being tested using molecular simulations that will be discussed in an upcoming paper. Alternatively, the presence of NH_3 and NH_4^+ may kinetically inhibit calcite growth and promote vaterite growth.

Observations on vaterite transformation to calcite indicate that the further supply of NH_3 gas has little influence on the stability of vaterite after vaterite matures. After the precipitates matured, the Petri dishes (containing solution and crystals) were either located in the chamber filled with NH_3 gas or in a chamber filled with pure N_2 gas (2 m^3). The stabilities of vaterite in the growth solution in both environments were almost the same. For the Petri dish (55 ml) placed in the sealed container filled with pure N_2, the ratio of ammonia released to the air as against the original dissolved ammonia in the solution could be obtained also through Henry's law (Eq. 2.4). The number of moles of ammonia in the gas phase (n) can be described by Eqs. (2.5) and (2.6), where V is the volume of the sealed container (2 m^3), V' is the total volume of salt solution in the Petri dishes (55 ml), and n' is the number of moles of NH_3 maintaining in the liquid phase.

Combining Eqs. (2.4), (2.5), and (2.6), it is obtained that 96.0% of the ammonia originally in solution would escape into the surrounding N_2 within hours in the case

where the Petri dishes were placed in a sealed container with N_2 gas (see discussion before on the time needed). This means that the solution cannot serve as a reservoir for ammonium adsorption to the surface any more. The fact that this reduction of dissolved ammonia did not affect the stability of vaterite indicates that the stability of grown vaterite may be not affected by the ammonia gas supply any more, but was affected by the incorporated ammonium in the vaterite lattice, or the N-species interacting with vaterite surfaces in the solution if the adsorption coefficient is high.

2.4.3 Substrate effects on polymorph selection

In addition to dissolved ammonia, the results listed in Table 2.1 show that the growth substrates are also capable of selecting polymorphs. While the ammonia content is the crucial factor, the growth substrate is a secondary one. In the presence of ammonia, a higher percentage of vaterite is grown in plastic Petri dishes compared to glass Petri dish substrates. Without ammonia, only calcite grows in either type of vessel. The fact that we find higher proportions of vaterite in the plastic (polystyrene) dishes is in agreement with Rieke [50] who reported that glass surfaces favor calcite while polystyrene surfaces favor vaterite growth. The fact that polymorphic compositions are significantly different on different substrates in the presence of ammonia implies that the ammonia-induced vaterite nucleates heterogeneously, since if ammonia promotes vaterite to nucleate directly from the liquid through the interactions with soluble species, the vaterite proportion of the precipitates would not notably vary with the substrates. It is not clear why polystyrene favors vaterite precipitation. One possible explanation may be that compared to glass, polystyrene adsorbs more ammonia which increases the local concentration of ammonia on the substrate surface and hence strengthens the ability of

ammonia to induce vaterite. Another possible reason may be that the surface of polystyrene absorbed with NH_4^+ reduces the interfacial energy of nucleation faces of vaterite.

The confirmed capability of ammonia to induce vaterite formation brings forward a serious problem when using the NH_3 diffusion method for the exclusive production of calcite. When using the ammonia diffusion method, high percentages of calcite only form at low NH_3 diffusion rates. This was confirmed by the results of the experiments with different diffusion rates of ammonia. This indicates that NH_3 only promotes vaterite formation when the NH_3 concentration exceeds a certain minimum value in the growth solution before $CaCO_3$ matures (higher than 0.02 mol/L in this study). The production rate of ammonia is highly sensitive to slight changes in the amount and the exposure area of the applied NH_4HCO_3 powders and to how hydrated the NH_4HCO_3 powders are. Therefore, when using the NH_3 diffusion method to grow calcium carbonate, the NH_3 gas itself has an influence on the selection of polymorphs, in addition to other environmental factors (pH, ionic strength, supersaturation etc.) and additives in solution, such as organic templates and growth modifiers that are discussed more often in the literature [25, 51-53]. This finding suggests that the NH_3 supply rate needs to be strictly limited to eliminate the influence of NH_3 as a growth modifier.

2.5 Conclusions

This study confirms the ability of ammonium/ammonia to promote the formation of vaterite over calcite. Ammonia/ammonium-induced vaterite displays flaky crystal layers with a hexagonal morphology. This study also shows that, in the presence of ammonia, the organic template, polystyrene, is more conducive to vaterite formation than

glass substrates under comparable conditions. More importantly, this study emphasizes the synergistic influence of the combination of the growth substrate and additives in solution. Based on the results of this study, changes in growth morphologies cannot only be attributed to organic additives or templates. Inorganic components in the growth solution, *e.g.*, ammonia when supplied by the NH_3 diffusion method and growth substrates from the reaction container or suspended materials may be equally powerful in promoting certain growth polymorphs. Thus, experiments have to be carefully designed to understand (and, if necessary, eliminate) the roles of ammonium and the substrate, especially if these are not growth modifiers to be studied. Otherwise, it may be impossible to tell whether the studied factors, such as organic additives, are the real causes that select vaterite over calcite.

FTIR results demonstrate that ammonium is incorporated into the vaterite lattice, but the substitution of ammonium is limited, on the order of 0.1 wt%. The analysis of the transformation of vaterite to calcite implies that, after vaterite matures, further supply of NH_3 gas has little influence on the stability of vaterite. The ammonium incorporated in the vaterite lattice, or the already-adsorbed N-species (if its adsorption coefficient is high) on the vaterite surface in the salt solution, might play the role of stabilizing the vaterite for a relatively long time, more than thirteen days.

References

1. Braissant, O., et al., *Bacterially induced mineralization of calcium carbonate in terrestrial environments: the role of exopolysaccharides and amino acids.* Journal of sedimentary research, 2003. **73**(3): p. 485-490.

2. Wolf, S.E., et al., *Phase selection of calcium carbonate through the chirality of adsorbed amino acids.* Angewandte Chemie International Edition, 2007. **46**(29): p. 5618-5623.
3. Dweck, J., et al., *Hydration of a Portland cement blended with calcium carbonate.* Thermochimica Acta, 2000. **346**(1-2): p. 105-113.
4. Kanakis, J., et al., *The crystallization of calcium carbonate on porcine and human cardiac valves and the antimineralization effect of sodium alginate.* Journal of Crystal Growth, 2001. **223**(4): p. 557-564.
5. Lowenstam, H. and D. Abbott, *Vaterite: a mineralization product of the hard tissues of a marine organism (Ascidiacea).* Science, 1975. **188**(4186): p. 363-365.
6. Rieger, J., et al., *Precursor structures in the crystallization/precipitation processes of $CaCO_3$ and control of particle formation by polyelectrolytes.* Faraday Discussions, 2007. **136**: p. 265-277.
7. Hosoda, N., A. Sugawara, and T. Kato, *Template effect of crystalline poly(vinyl alcohol) for selective formation of aragonite and vaterite $CaCO_3$ thin films.* Macromolecules, 2003. **36**(17): p. 6449-6452.
8. Lian, B., et al., *Carbonate biomineralization induced by soil bacterium Bacillus megaterium.* Geochimica et Cosmochimica Acta, 2006. **70**(22): p. 5522-5535.
9. Kitamura, M., *Crystallization and transformation mechanism of calcium carbonate polymorphs and the effect of magnesium ion.* Journal of Colloid and Interface Science, 2001. **236**(2): p. 318-327.
10. Didymus, J.M., et al., *Influence of low-molecular-weight and macromolecular organic additives on the morphology of calcium carbonate.* Journal of the Chemical Society-Faraday Transactions, 1993. **89**(15): p. 2891-2900.
11. Heywood, B.R., S. Rajam, and S. Mann, *Oriented crystallization of $CaCO_3$ under compressed monolayers. 2. morphology, structure and growth of immature crystals.* Journal of the Chemical Society-Faraday Transactions, 1991. **87**(5): p. 735-743.
12. Rudloff, J. and H. Colfen, *Superstructures of temporarily stabilized nanocrystalline $CaCO_3$ particles: Morphological control via water surface tension variation.* Langmuir, 2004. **20**(3): p. 991-996.
13. Lee, H.S., T.H. Ha, and K. Kim, *Fabrication of unusually stable amorphous calcium carbonate in an ethanol medium.* Materials Chemistry and Physics, 2005. **93**(2-3): p. 376-382.
14. Shen, Q., et al., *Crystallization and aggregation behaviors of calcium carbonate in the presence of poly(vinylpyrrolidone) and sodium dodecyl sulfate.* Journal of Physical Chemistry B, 2005. **109**(39): p. 18342-18347.
15. Gorna, K., et al., *Bioinspired mineralization of inorganics from aqueous media controlled by synthetic polymers.* Macromolecular Bioscience, 2007. **7**(2): p. 163-173.
16. Rodriguez-Navarro, C., et al., *Bacterially mediated mineralization of vaterite.* Geochimica et Cosmochimica Acta, 2007. **71**(5): p. 1197-1213.
17. Becker, A., et al., *In-vitro crystallization of calcium carbonate in the presence of biological additives - comparison of the ammonium carbonate method with double-diffusion techniques.* Zeitschrift für anorganische und allgemeine Chemie, 2003. **629**(12-13): p. 2305-2311.

18. Addadi, L., et al., *A chemical-model for the cooperation of sulfates and carboxylates in calcite crystal nucleation-relevance to biomineralization* Proceedings of the National Academy of Sciences of the United States of America, 1987. **84**(9): p. 2732-2736.
19. Gehrke, N., et al., *Superstructures of calcium carbonate crystals by oriented attachment.* Crystal Growth & Design, 2005. **5**(4): p. 1317-1319.
20. Belser, L.W., *Population ecology of nitrifying bacteria.* Annual Review of Microbiology, 1979. **33**: p. 309-333.
21. Allison, J.D., D.S. Brown, and K.J. Novo-Gradac, *MINTEQA2/PRODEFA2, a geochemical assessment model for environmental systems: Version 3. 0 user's manual*, in *US Environmental Protection Agency, Athens, GA*. 1991. p. 117
22. Jiménez-López, C., et al., *Chemical, mineralogical and isotope behavior, and phase transformation during the precipitation of calcium carbonate minerals from intermediate ionic solution at 25 ^{o}C.* Geochimica et Cosmochimica Acta, 2001. **65**(19): p. 3219-3231.
23. Roisnel, T. and J. Rodriguez-Carvajal, *WinPLOTR: A windows tool for powder diffraction pattern analysis.* Materials Science Forum, 2001. **378-381**(I): p. 118-123.
24. Kralj, D., L. Brecevic, and J. Kontrec, *Vaterite growth and dissolution in aqueous solution III. Kinetics of transformation.* Journal of Crystal Growth, 1997. **177**(3-4): p. 248-257.
25. Ogino, T., T. Suzuki, and K. Sawada, *The formation and transformation mechanism of calcium carbonate in water.* Geochimica Et Cosmochimica Acta, 1987. **51**(10): p. 2757-2767.
26. Kamhi, S., *On the structure of vaterite $CaCO_3$.* Acta Crystallographica, 1963. **16**(8): p. 770-772.
27. Busigny, V., et al., *Ammonium quantification in muscovite by infrared spectroscopy.* Chemical Geology, 2003. **198**(1-2): p. 21-31.
28. Thompson, H.W., et al., *Introduction to Infrared and Raman Spectroscopy.* Academic Press, New York, 1964.
29. Ahn, D.J., A. Berman, and D. Charych, *Probing the dynamics of template-directed calcite crystalization with in situ FTIR.* Journal of Physical Chemistry, 1996. **100**(30): p. 12455-12461.
30. Busigny, V., et al., *Quantitative analysis of ammonium in biotite using infrared spectroscopy.* American Mineralogist, 2004. **89**(11-12): p. 1625-1630.
31. Liu, D.X. and M.Z. Yates, *Formation of rod-shaped calcite crystals by microemulsion-based synthesis.* Langmuir, 2006. **22**(13): p. 5566-5569.
32. Cussler, E.L., *Diffusion: Mass Transfer in Fluid Systems*. 1997, Cambridge: Cambridge University Press.
33. Arbuckle, W.B. and J.E. Alleman, *Effluent toxicity testing using nitrifiers and microtox^{TM}*. Water Environment Research, 1992(3): p. 263-267.
34. Suchanek, W., et al., *Hydroxyapatite ceramics with selected sintering additives* Biomaterials, 1997. **18**(13): p. 923-933.
35. Bertonia, E., et al., *Nanocrystals of magnesium and fluoride substituted hydroxyapatite.* 1998. **72**: p. 7.

36. Mann, S., *Biomineralization: principles and concepts in bioinorganic materials chemistry.* Oxford University Press, Inc., New York,, 2001.
37. Reddy, M.M., *Crystallization of calcium carbonate in the presence of trace concentrations of phosphorus-containing anions : I. Inhibition by phosphate and glycerophosphate ions at pH 8.8 and 25°C.* Journal of Crystal Growth, 1977. **41**(2): p. 287-295.
38. Francis, M.D., et al., *Diphosphonates inhibit formation of calcium phosphate crystals in vitro and pathological calcification in vivo.* Science, 1969. **165**(3899): p. 1264-1266.
39. Becker, U., et al., *Selective attachment of monovalent background electrolyte ions and growth inhibitors to polar steps on sulfates as studied by molecular simulations and AFM observations.* Molecular Simulation, 2002. **28**(6): p. 607-632.
40. Becker, U., et al., *Interactions between mineral surfaces and dissolved species: From monovalent ions to complex organic molecules.* American Journal of Science, 2005. **305**(6-8): p. 791-825.
41. Dobson, P.F., S. Epstein, and E.M. Stolper, *Hydrogen isotope fractionation between coexisting vapor and silicate-glasses and melts at low-pressure.* Geochimica et Cosmochimica Acta, 1989. **53**(10): p. 2723-2730.
42. Pandya, N., D.W. Muenow, and S.K. Sharma, *The effect of bulk composition on the speciation of water in submarine volcanic glasses.* Geochimica et Cosmochimica Acta, 1992. **56**(5): p. 1875-1883.
43. Bell, D.R., P.D. Ihinger, and G.R. Rossman, *Quantitative analysis of trace OH in garnet and pyroxenes.* American Mineralogist, 1995. **80**(5-6): p. 465-474.
44. Collins, K.D., *Sticky ions in biological systems.* Proceedings of the National Academy of Sciences of the United States of America, 1995. **92**(12): p. 5553-5557.
45. Shannon, R., *Revised effective ionic radii and systematic studies of interatomic distances in halides and chalcogenides.* Acta Crystallographica Section A, 1976. **32**(5): p. 751-767.
46. Board, R. and H. Perrott, *Vaterite, a constituent of the eggshells of the nonparasitic cuckoos,Guira guira and Crotophagi ani.* Calcified Tissue International, 1979. **29**(1): p. 63-69.
47. Wang, J. and U. Becker, *Structure and carbonate orientation of vaterite ($CaCO_3$).* American Mineralogist, 2009. **94**(2-3): p. 380-386.
48. Zhang, Y. and Z. Xu, *Atomic radii of noble gas elements in condensed phases.* American Mineralogist, 1995. **80**(7-8): p. 670-675.
49. Feng, J., et al., *Observation of bicarbonate in calcite by NMR spectroscopy.* American Mineralogist, 2006. **91**(5-6): p. 957-960.
50. Rieke, P.C., *Selection of phase and control of orientation during physisorption on surfaces of homogeneously formed calcium carbonate nuclei.* Materials Science & Engineering C-Biomimetic and Supramolecular Systems, 1995. **2**(3): p. 181-189.
51. Mann, S., et al., *Controlled crystallization of $CaCO_3$ under stearic acid monolayers.* Nature, 1988. **334**(6184): p. 692-695.
52. Kasuga, T., et al., *Preparation of poly(lactic acid) composites containing calcium carbonate (vaterite).* Biomaterials, 2003. **24**(19): p. 3247-3253.

53. Pouget, E.M., et al., *The initial stages of template-controlled $CaCO_3$ formation revealed by cryo-TEM.* Science, 2009. **323**(5920): p. 1455-1458.

CHAPTER THREE
GROWTH PROCESS AND CRYSTALLOGRAPHIC PROPERTIES OF AMMONIA-INDUCED VATERITE

Abstract: Metastable vaterite crystals were produced by increasing the pH and consequently the saturation states of Ca^{2+}- and CO_3^{2+}-containing solutions using an ammonia diffusion method. SEM and TEM analyses indicate that vaterite grains produced in such a way are polycrystalline aggregates with a final morphology that has a 6-fold-symmetry. The primary structure develops within an hour and is an almost spherical assemblage of nanoparticles (5-10 nm) with random orientation, followed by the formation of hexagonal platelets (1-2 μm), which are first composed of nanoparticles and that develop more and more into single crystals. As determined using transmission electron microscopy, these hexagonal crystallites are terminated by (001) surfaces and are bounded by {110} edges. These hexagonal crystals subsequently stack to form the "petals" (20 μm wide, 1 μm thick) of the final "flower-like" vaterite morphologies. The large flakes gradually tilt towards the center as growth progresses so their positions become more and more vertical, which eventually leads to a depression in the center.

Since this sequence encompasses a number of morphologies observed in previous studies (spheres, hexagons, flowers *etc*.), they may actually represent different stages of this growth sequence rather than equilibrium morphologies for certain growth conditions.

3.1 Background

Calcium carbonate ($CaCO_3$) occurs widely on the Earth's surface and represents the largest geochemical reservoir for carbon [1, 2]. There are three major polymorphs of $CaCO_3$, calcite, aragonite, and vaterite. Vaterite, the least thermodynamically stable polymorph of $CaCO_3$, has been of great interest because its crystallization is strongly associated with biogenic activities. For example, vaterite occurrences are widely documented in carbonate mineralization mediated by soil bacteria [3, 4], in fresh-water cultured pearls from mussels [5], as well as in inorganic tissues like gallstones and human heart valves [6, 7]. In addition, vaterite can be an important precursor for other polymorphs, especially calcite, in biomineralization processes. In industrial settings, vaterite has been used extensively as a stabilizer in suspension polymerization, as material for regenerative medicine applications, and as an encapsulating substance suitable for pharmaceutical applications [8, 9]. Elucidating the vaterite growth mechanism and structure characteristics will expand our knowledge on how organisms control carbonate morphologies and polymorph selections and may improve the engineering applications of vaterite as an industrial material.

Various experimental conditions have been reported to promote vaterite synthesis. Facilitating factors include high supersaturation with respect to $CaCO_3$ [10-15], the presence of certain organic additives and organic templates [16-26] or inorganic additives (*e.g.*, NH_3) [27, 28], and high pH [29]. Different methods render different characteristics for vaterite crystallization, such as growth kinetics and crystal stability, among which the morphology may be the most uncertain one because it displays a great deal of variety. The most intensively reported morphology is the spherical shape [30, 31]. Many others,

such as fried-egg shape, flower-like shape, and hexagonal flake shape are also frequently observed [19, 27, 32]. However, how these morphologies develop, what the texture of the resultant crystals is, and what the different shapes have in common, remains to be addressed. In this study, the crystallographic characteristics and growth process of a flower-like vaterite, induced by the ammonia diffusion method, are investigated to shed light on the different stages of the crystallization mechanism of vaterite.

3.2 Experimental procedure

$CaCO_3$ crystals were cultivated using an ammonia diffusion method [4] in a closed container of 33 liters at ambient conditions. Nine open plastic Petri dishes, each containing 45 mL of 0.002 M $CaCl_2$-$NaHCO_3$ salt solutions, and one beaker, containing fresh NH_4HCO_3 powder, were placed in the container. The original pH of the salt solution was adjusted to 3.4 by adding 10% HCl such that initially, all Ca and carbonate species are in solution. Subsequent decomposition of NH_4HCO_3 in separate containers produced NH_3 gas, which diffused into the $CaCl_2$-$NaHCO_3$ salt solution, increasing the solution pH and, hence, the supersaturation with respect to $CaCO_3$.

Preliminary tests show the availability ammonia strongly influences the polymorph composition of the precipitates. The optimal condition for a high percentage of vaterite crystallization was determined by running a series of parallel experiments of different ammonia diffusion rates by varying the amount and exposure area of the NH_4HCO_3 powder. It was found that nearly 100% vaterite yield (confirmed by both optical microscopy and using a Scintag X1 X-ray diffractometer) can be achieved using two 100 mL beakers each containing 25 g fresh NH_4HCO_3 powder. The pH of the salt solution increases from the original value, 3.4, to the final one, 9.6, within an hour. The

supersaturations of the solution at the final pH with respect to all three polymorphs, calcite, aragonite and vaterite were 1.855, 1.717, and 1.289, respectively (calculated using MINTEQ version 2.51 [33], where the supersaturation state β is defined as

$$\beta = \ln\left(\frac{a(\mathrm{Ca}^{2+})a(\mathrm{CO}_3^{2-})}{K_{sp}}\right) \tag{3.1}$$

where $a(Ca^{2+})$ and $a(CO_3^{2-})$ are the activities of Ca^{2+} and CO_3^{2-}, respectively. Control experiments were conducted to examine the role of NH_3 on vaterite formation. This was done by adjusting the solution pH by adding NaOH instead of diffusing ammonia while maintaining the same rate of pH increase over the course of the experiment. It was found that calcite was the dominant phase in the control runs, indicating the ability of ammonia to promote vaterite formation.

Harvested vaterite crystals from each experimental run were dried and gold coated, and subsequently analyzed using field-emission-gun scanning electron microscopy (SEM, Hitachi S3200N). Specifically, crystals were collected every 30 minutes in the first four hours after the salt solution reached the final pH and every two hours thereafter until the crystals matured (in 16 hours). The development of the vaterite morphology was also observed using *in situ* optical microscopy every two hours throughout the growth process.

The crystallographic properties of vaterite in the initial (within first hour) and final (after 16 hours) stages were studied using transmission electron microscopy (TEM). Fine powder samples of vaterite were placed onto a holey carbon grid and analyzed using a JEOL 2010F instrument operating at 200 kV with minimized electron current density to avoid ionization. The chemical composition ($CaCO_3$) was confirmed by using energy-

dispersive spectroscopy. Bright and dark field imaging was used to study the morphology in details. The diffraction patterns and high-resolution TEM images were used to examine the crystal structures.

3.3 Results

3.3.1 Effect of NH_4^+/NH_3 on vaterite formation

While calcite was the dominant phase in the control runs where NaOH was used to adjust pH, vaterite was nearly the only polymorphic phase in the ammonia diffusion experiments (Fig. 3.1). The NH_3 diffusion method is typically used to prepare calcite crystals; however, our work shows that the existence of NH_3 will greatly influence the initial polymorph composition of the precipitates. High percentages of calcite are only formed at low NH_3 diffusion rates, while vaterite becomes the major component when NH_3 diffuses fast and reaches certain concentrations (higher than 0.02 mol/L in this study) in the growth solution before $CaCO_3$ matures. More details on this topic are discussed in Hu et al. (in rev.).

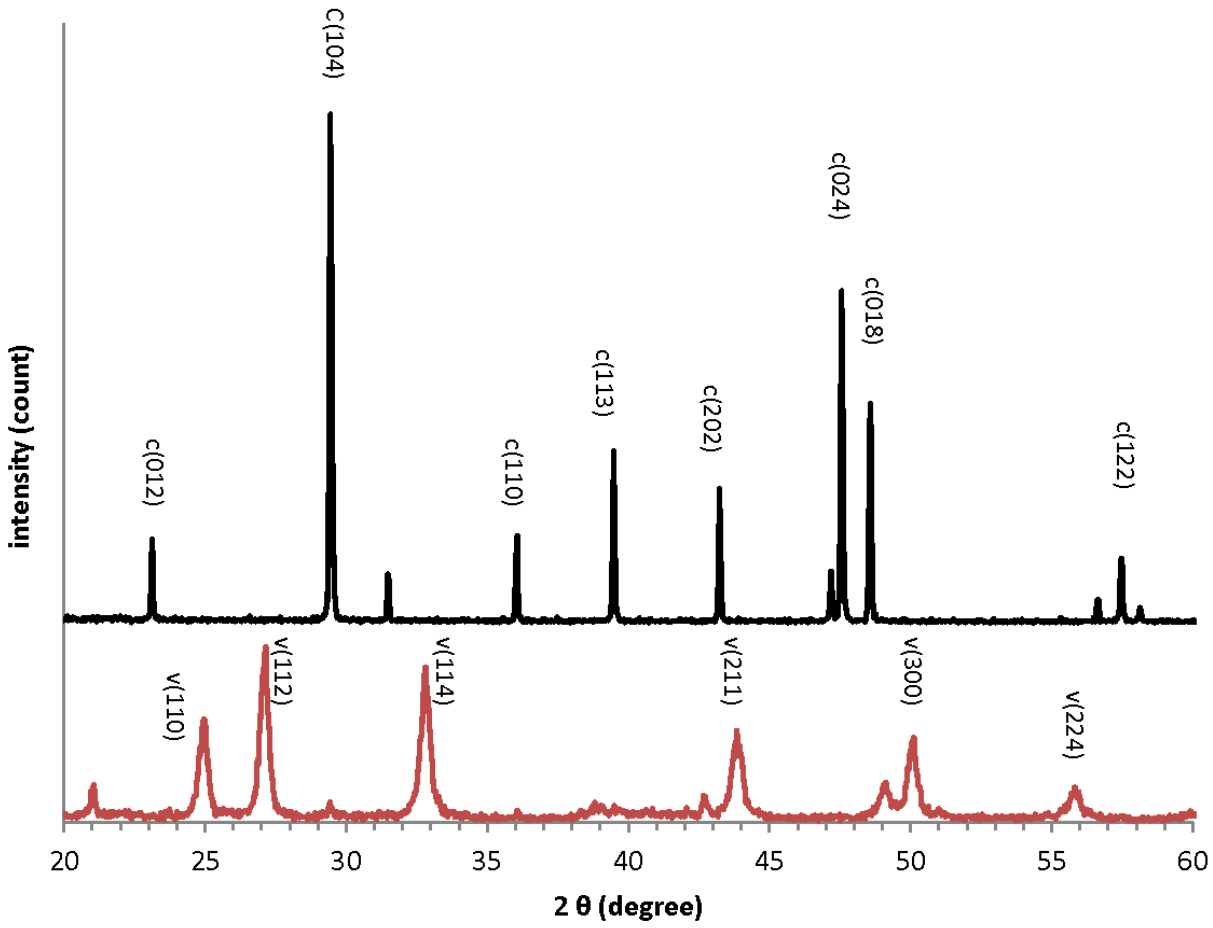

Figure 3.1 XRD results confirm that the precipitates are nearly pure vaterite in the experiential runs applied NH_3 diffusion method of high evaporation rate of NH_3 (A). In contrast, calcite is the dominant phase in the control runs absent of NH_3 but applying dilute NaOH to increase pH (B). Numbers in parentheses indicate the Miller indices, and C and V denote calcite and vaterite, respectively.

3.3.2 Evolution of crystal morphologies over time

SEM images (Fig. 3.2) of vaterite morphologies at different growth stages illustrate a dramatic change of shape over time. Quasi-spherical crystals about 2 μm in diameter were observed after the first hour (Fig. 3.2 A), followed by the development of thin horizontal slabs branching out from the spheres within the next 30 min, transforming the original grain into a roughly hexagonal plate about 10 μm in diameter (Fig. 3.2 B). Continuous growth of the slabs after that, with the ones at the peripheral area growing faster than the ones in the central region of the plate, causes the newly emerged layers to tilt progressively toward the center, resulting in a three-dimensional (3D) morphology with a pit in the center (Fig. 3.2 D). The grain reaches the size of about 20 μm in diameter after 4 hours, and about 60 μm after 16 hours when it fully matures. At the final stage, the vaterite grain displays flaky crystal layers with a 6-fold symmetry (Fig. 3.2 E). The leaves that formed last stand almost vertical surrounding the depression in the center (Fig. 3.2 E, shown with higher magnification in Fig. 3.2 F).

3.3.3 Evolution from growth unit assemblage to final morphology

For the spherical vaterite grains grown in the first hour, bright and dark field images taken of the same area illustrate that the crystals are composed of randomly oriented nanoparticles that show no clearly defined shape (Fig. 3.3 A and 3.3 B). The corresponding high-resolution TEM image (Fig. 3.3 C) reveals the discontinuity between the structure of individual nano-crystals (5 nm). The fast Fourier transformation pattern of the high-resolution TEM image demonstrates a polycrystalline texture and confirms the crystal structure as vaterite.

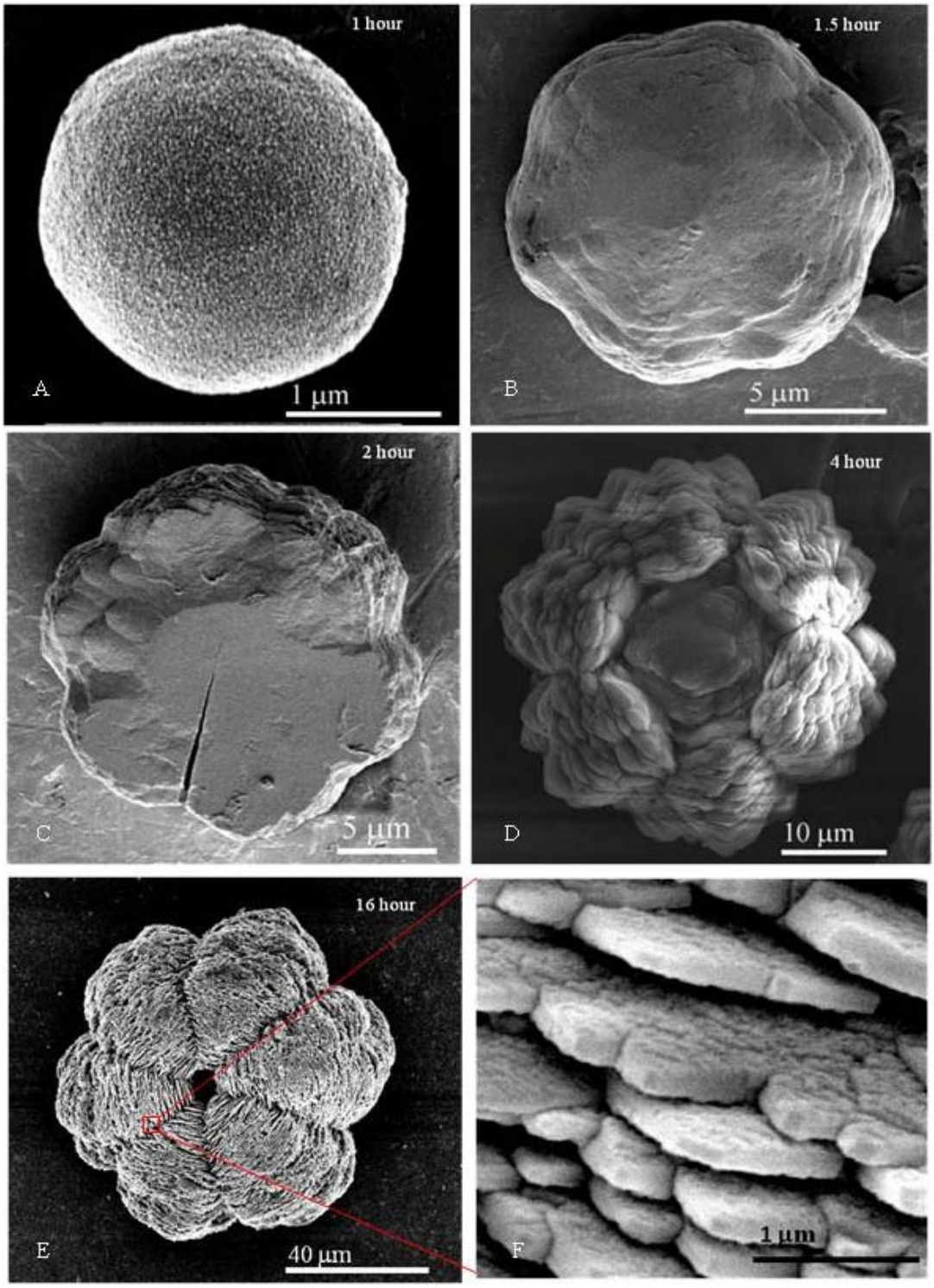

Figure 3.2 SEM images displaying the crystallization of vaterite grain as a function of time. The labels on the right corner of each image, indicate after how many hours the crystals were harvested, measured from the time the salt solution reached its final pH.

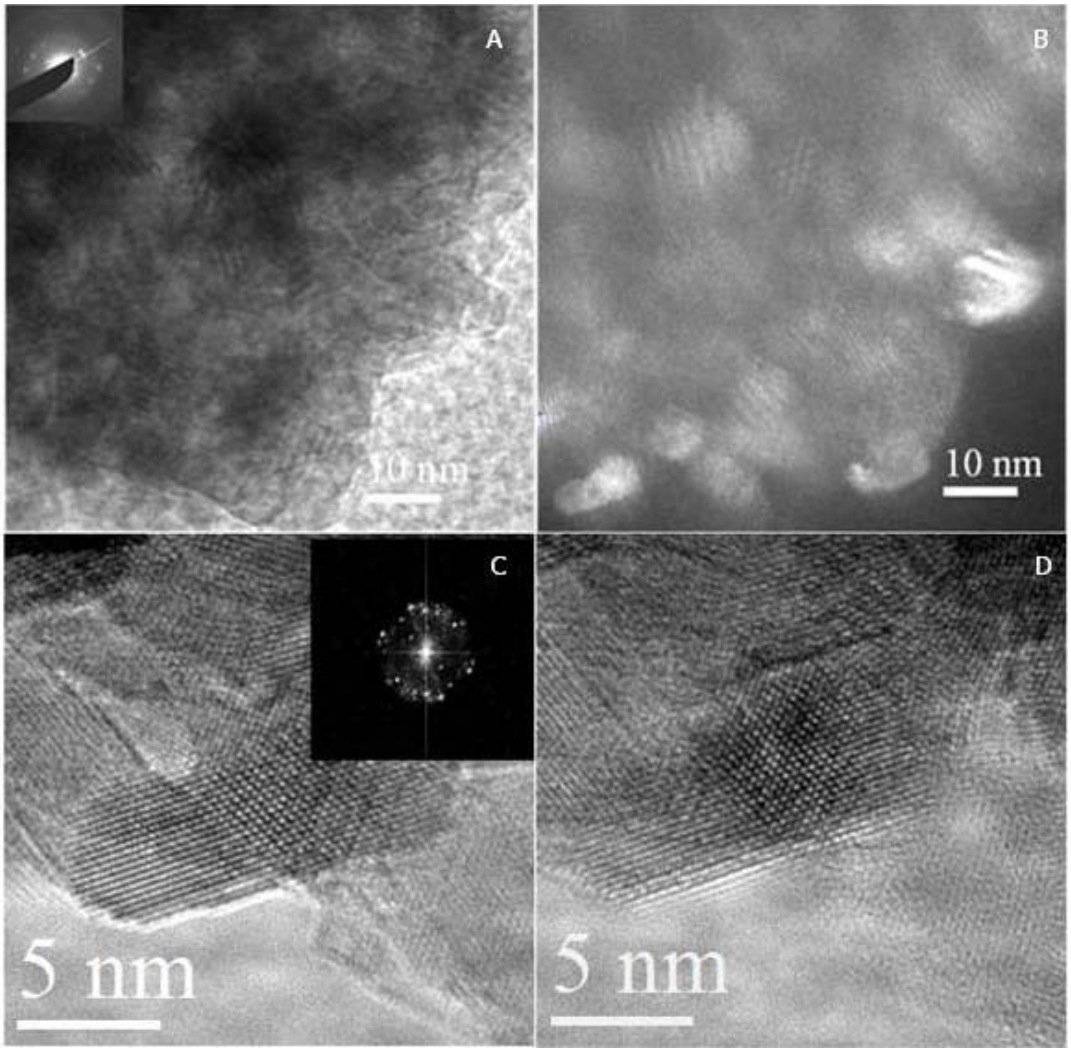

Figure 3.3 Bright (A) and dark (B) field TEM images, showing the vaterite nanocrystalline structure lack of uniform orientations forming at the first hour after the solution pH reaching the maximum value. C: corresponding high resolution TEM image. D: corresponding high resolution TEM image after the 10-minute electron beam bombardment, displaying a high resistance of nanocrystalline vaterite to the ionizing irradiation of the electron beam.

In contrast, the more mature grains collected at later stages possess a more distinctive texture. Low-magnification SEM images show that the vaterite grains are composed of large flakes, each about 10-20 μm in diameter (Fig. 3.4 B). High-magnification SEM and TEM images reveal that individual large flakes are formed by numerous small hexagonal platelets, each about 1 μm in diameter (Fig. 3.4 C, 3.3 D, and 3.5D). The corresponding diffraction patterns of the high-magnification TEM image demonstrate that the small hexagonal platelets are single crystals of vaterite with basal (001) faces and hexagonal boundaries parallel to {110}. A periodic arrangement of atoms of the hexagonal crystallites is revealed by the high-resolution TEM image shown in Figure (3.6 C), displaying long-range order of atoms on the vaterite (001) surface.

Although the matured vaterite possesses a secondary structure made of hexagonal platelets, the individual plates do not seem to be single crystals but rather assemblies of nanoparticles of about 5-10 nm in diameter (Fig. 3.2 F, Fig. 3.5), similar to the particle sizes on the spherical vaterite grains formed within the first hour. A series of high-magnification SEM images (Fig. 3.5) corresponding to the images in Figure 3.2 shows how the vaterite crystals grow through the re-organization of the nano-clusters. In the first hour, the vaterite grain is a spherical ball composed of randomly positioned/oriented nanoparticles. In the next three hours, the nanoparticles start to align themselves to form hexagonal pieces, but the hexagonal shape is not well developed as the boundaries are jagged, only showing blunt angles around 120° between two sides. After four hours, the hexagonal shape becomes increasingly clear and the edges become more and more straight. In the final stage, these hexagonal pieces have well developed, with perfectly

straight boundaries and the nanoparticles that are the original building blocks are tightly packed.

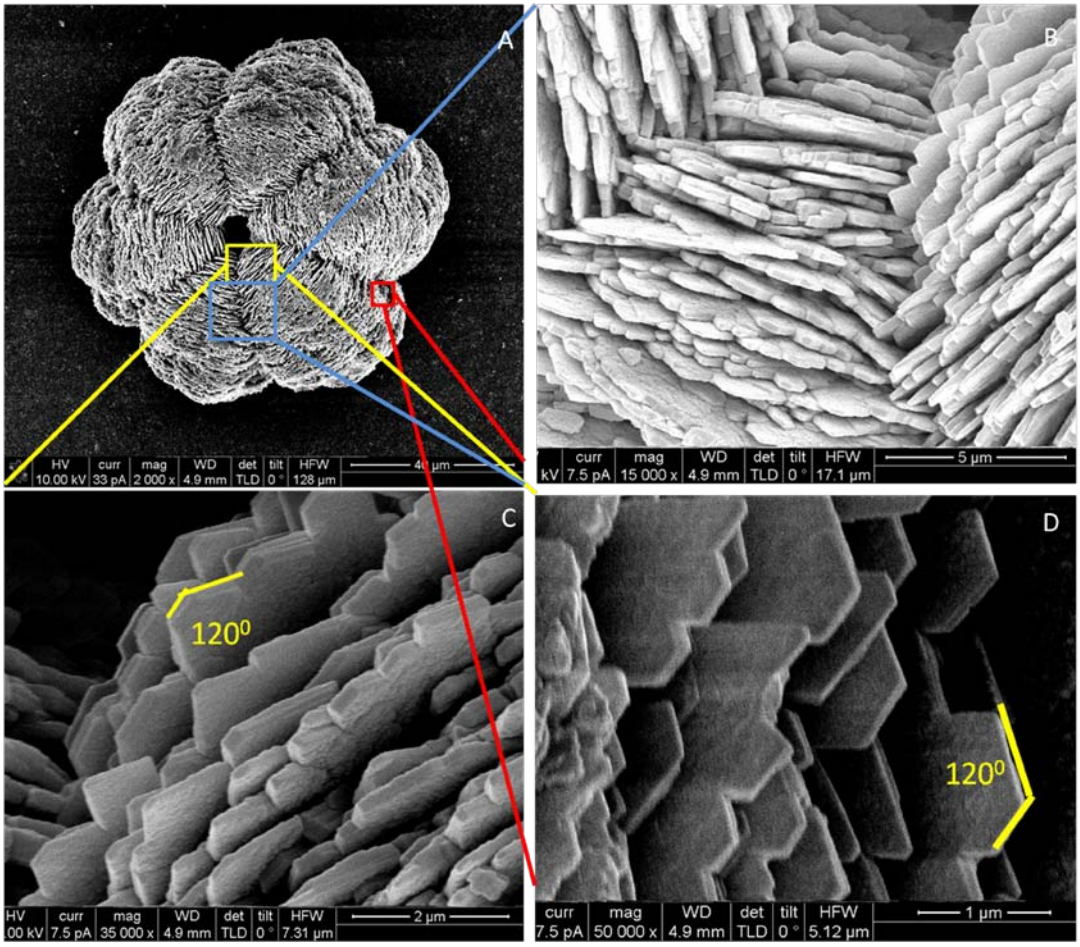

Figure 3.4 A and B: Vaterite grain is composed of large flakes (10-20 μm). C and D: Each large flake is composed of numerous small hexagonal pieces (1 μm).

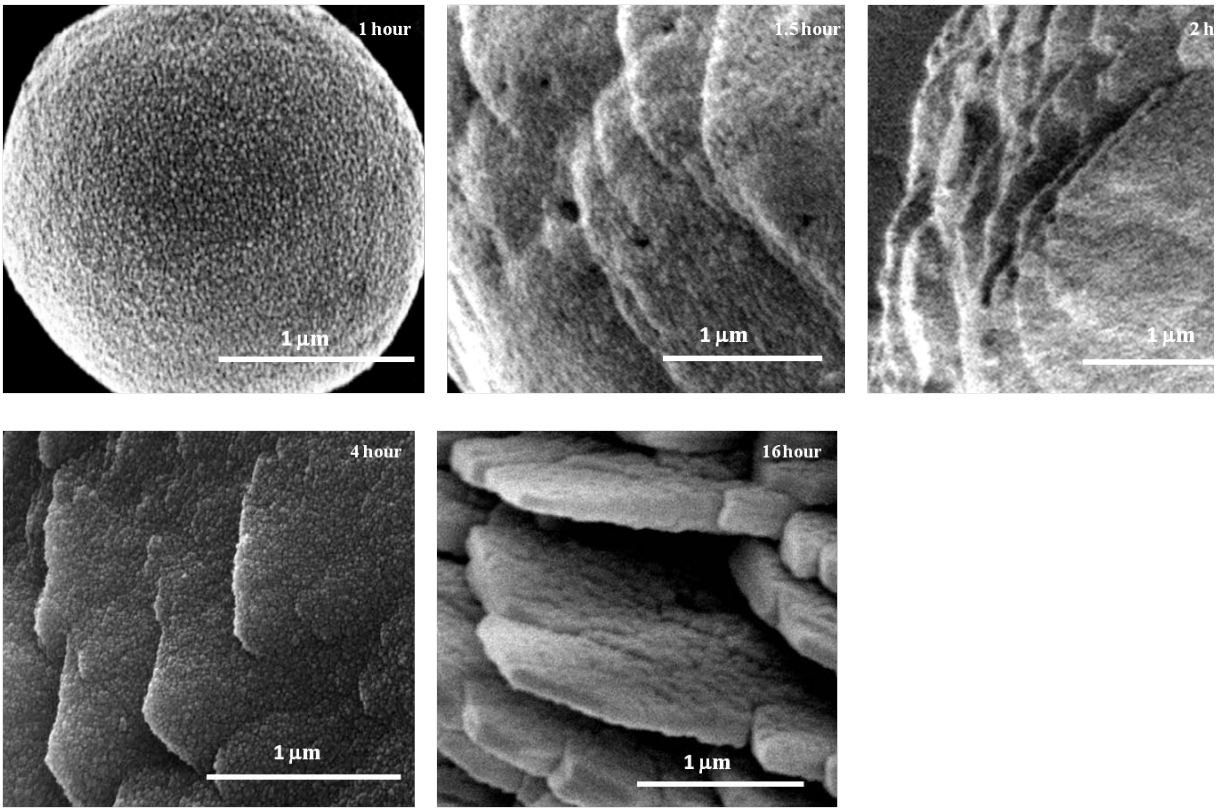

Figure 3.5 A series of high magnification SEM images of the vaterite as a function of time (note the constant scale bar).

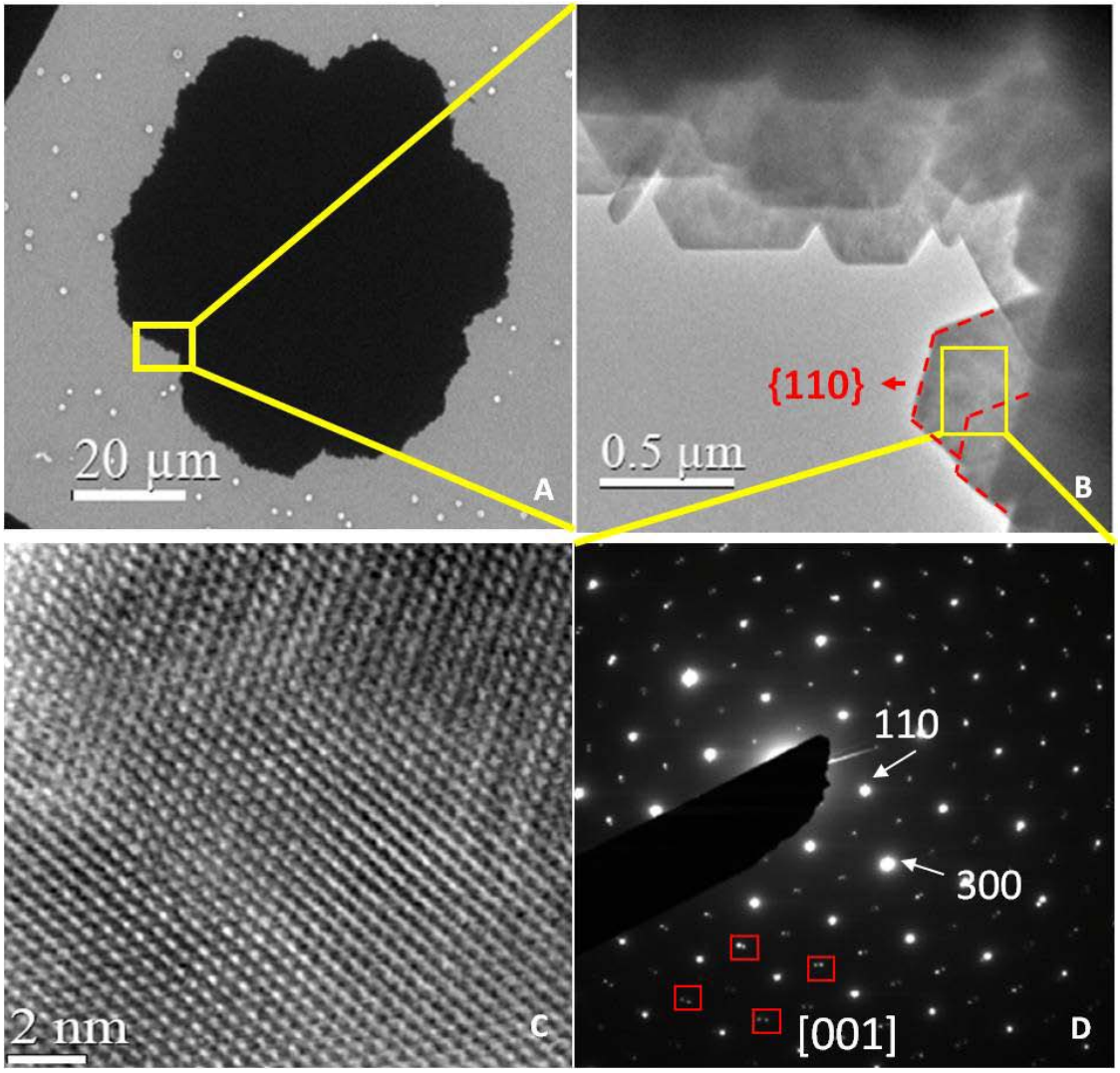

Figure 3.6 A and B: low and high magnification TEM images show the layered structure of vaterite and the unit bricks that are small hexagonal pieces of 1 μm. C: a high resolution TEM image shows atomic lattices of vaterite along [001], revealing an ordered arrangement of atoms. D: corresponding diffraction pattern along vaterite [001], demonstrating the hexagonal pieces shown in B terminates at {110}.

Meanwhile, the roughly spherical cores of the vaterite crystals preserve the disordered array of composing nanoparticles (Fig. 3.5), indicating a lack of dissolution and re-crystallization after the initial nucleation.

An interesting phenomenon is that aggregates of nanoparticles formed in the early stage show an unusually high resistance to the ionizing irradiation of electron beam from TEM. $CaCO_3$ in general is vulnerable to high temperature and electron bombardment. In this study, after an irradiation at a fluence of $1.25 - 2.5 \cdot 10^{12}$ electrons/cm^2, both single crystals of calcite (20-30 μm) or grown vaterite layers of crystalline structure (1-2 μm) begin to decompose. However, the nanocrystalline vaterite stays stable even after an irradiation at a fluence of $1.12 \cdot 10^{14}$ electrons/cm^2. The high-resolution TEM image (Fig. 3.3 D) displaying the crystallinity of nanoparticulate vaterite demonstrates that it is almost intact in comparison to the original one before the irradiation with $1.12 \cdot 10^{14}$ electrons/cm^2 (Fig. 3.3 C).

It is interesting to note that in the TEM diffraction pattern (Fig. 3.6 D), starting from the third nearest circle (*i.e.*, (400) spots) to the transmitted spot (in the center), two separate spots can be detected at each location of the diffraction spot. The double-spot phenomenon is not clearly resolved in the first two circles close to the transmitted spot due to the high intensities of the lower-order diffraction spots. The distances between the two split spots increase with the distance from the center (as illustrated). The contrasted color of the high-resolution TEM image (Fig. 3.6 B) demonstrates that the area where the diffraction pattern was taken (as illustrated) locates two small hexagonal pieces. Therefore, the TEM diffraction pattern actually depicts the crystallographic structures of two crystallites, which illustrates two phenomena: 1) these two hexagonal platelets have

the same structure, since the two sets of patterns are identical, and 2) the two crystallographic orientations diverge a little bit from each other because one diffraction pattern is rotated slightly with respect to the other.

3.4 Discussion

3.4.1 The hierarchical structure and the development of vaterite grains

SEM images show that the texture of grown vaterite in this study possesses a hierarchy of four levels. SEM analysis (Fig. 3.2 E and F) reveals that each grown vaterite grain is a 3D structure of 6-fold symmetry, like a flower of six petals. The primary structure is the basic level of this hierarchy and is the assemblage of nanoparticles (5-10 nm). The secondary structure is the next "level up" from the primary structure and is the stacking of hexagonal platelets (1-2 μm) which are initially composed of nanoparticles. These hexagonal pieces are single crystals. They grow together epitaxially and hence possess similar orientations. The tertiary structure is the arrangement of large stacked platelets (20 μm wide, 1 μm thick), which are built up by small hexagonal pieces, thus forming the six "petals" of the flower-like grain. The large flakes gradually tilt towards the center as growth progresses so their positions become vertical, which eventually forms a depression in the center. This quaternary structure is the last level of vaterite growth, referring to the 6-fold arrangement of six petals.

3.4.2 The building blocks of vaterite grains: nanoparticles

Therefore, we hypothesize that these nanoparticles (5-10 nm) are the building blocks of vaterite grains and that vaterite crystallization is a process of assemblage of these nano-clusters. Nanoparticles aggregate randomly in the first hour but line up later

along specific crystallographic orientations. To verify this hypothesis, SEM and TEM images of vaterite in high magnification were analyzed throughout the growth process.

Given the structure characteristics of vaterite in different growth stages revealed by SEM and TEM analysis (Fig. 3.3, Fig. 3.5), the nanoparticle (5-10 nm) may be the building unit of vaterite grains. The way that nanoparticles stack determines the overall shape of the vaterite grain. As vaterite develops, the way nanoparticles are stacked becomes increasingly crystallographically oriented, resulting in a phase change from poorly crystalline to crystalline. In the early stage (the first hour), clusters compact together with random orientations, forming a sphere about a couple of microns in diameter. This may be due to the high supersaturation that results in a high driving force for $CaCO_3$ nucleation. This phase with random aggregation of nanoparticles, similar to an amorphous phase, is not the most energetically favorable one due to interfacial strain. Therefore, as the crystals precipitate, the supersaturation status decreases and the subsequently formed nanoparticles tend to connect to each other in a crystallographically orientated way, which is thermodynamically more stable than random attachment. This process results in the development of single crystals (small hexagonal pieces) with an increasingly smooth surface and sharp boundaries. However, the loosely ordered sphere forming in the early stage stays to be an aggregation of nanoparticles, not dissolving and re-crystallizing into a more ordered phase thereafter. Figure 3.7, taken after the vaterite grain matured, reveals that those nanoparticles still keep their random orientation in the core area, indicating the core is disordered as well. The model of vaterite growth is illustrated in Figure 3.8.

This oriented attachment occurring after the initial stage of crystallization is a common growth mechanism for nanocrystals (also found in ZnS and TiO_2, anatase [34, 35]) reducing the overall crystal energy by removing the high energy surfaces.

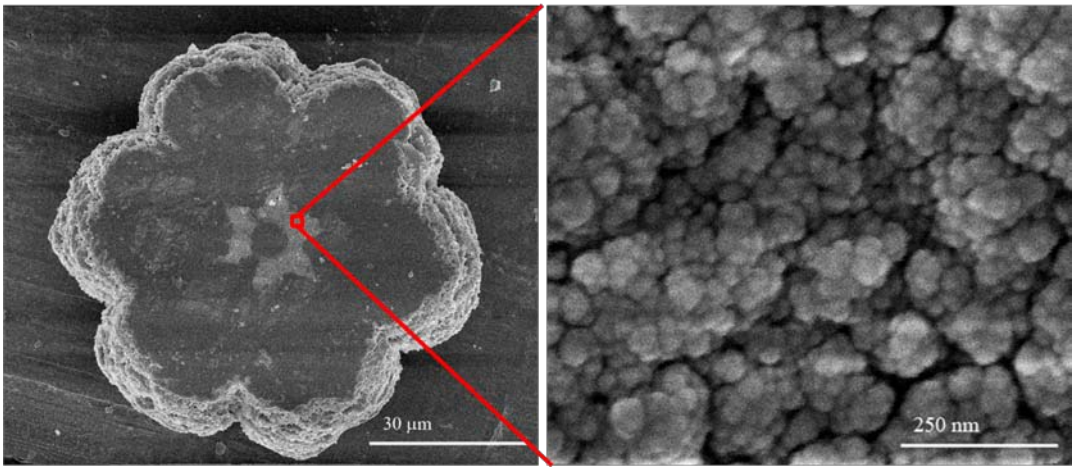

Figure 3.7 SEM image of a grain of vaterite upside down (left), showing the flat faces attaching to the Petri dish. In the center is the core area forming in the first two hours. The high magnification SEM image of the core (right), showing the irregular texture and the aggregation of nano-particles of random orientations.

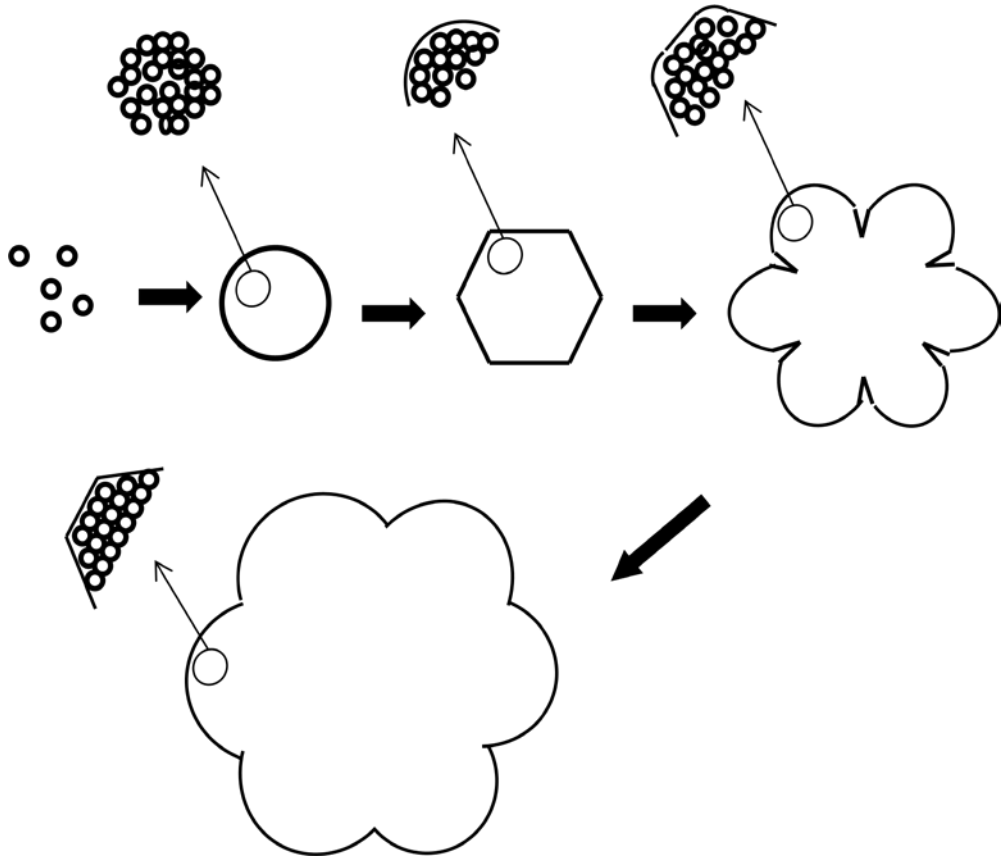

Figure 3.8 Schematic demonstrating the development of the 6-fold flower-like vaterite grain. The 2-D morphology of vaterite grain changes from spherical to hexagonal shape. The arrangement of the building blocks, nanoparticles, becomes increasingly ordered. See text for details.

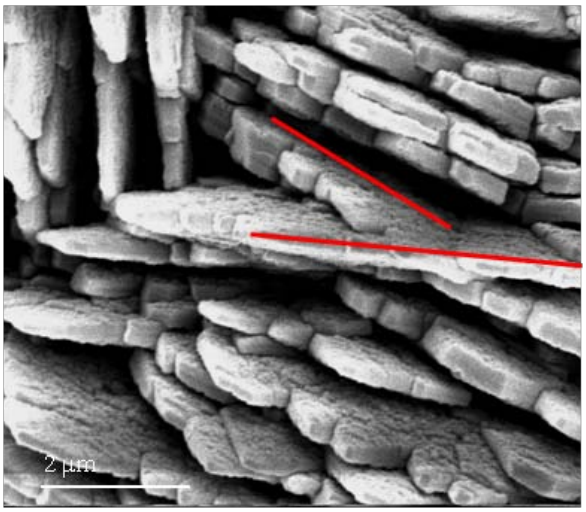

Figure 3.9 Dislocation occurring during the oriented attachments of crystallization.

Our observations described above reveal a fundamental difference between the growth mode of calcite and vaterite. A plethora of studies convincingly document the layer-by-layer growth mechanism for calcite crystallization. In particular, *in situ* imaging techniques such as atomic force microscopy show that the edges of the monolayer calcite remain smooth and maintains strong directionality during growth [36-42]. This suggests that the growth of calcite is in fact an ion-by-ion mechanism where the adsorption to an existing kink is highly favored with respect to the generation of a new kink. This implies that growth is highly favored to be spiral growth and the kink (or the continuous filling of the kink that travels around the spiral) leads to a layer-by-layer mechanism. For vaterite growth, however, the data show there is no such highly organized molecular attachment scheme. Instead, solute particles form clusters of certain sizes which then coagulate to propagate the lattice.

Thermodynamic suggest that the growth of vaterite is likely more entropically favored (in comparison with the growth of calcite) as the clusters at the moment of initial coagulation are randomly oriented. This further suggests that the crystallization of vaterite is probably a kinetically limited process as random aggregation of molecular clusters does not significantly lower the free energy of the system, whereas the growth of calcite is controlled more strongly by thermodynamics because oriented and simultaneous attachment of a group of molecules keeps the system's energy gain at the minimum.

The changes of the interior structures of vaterite in different growth stages may explain why the electron-beam resistance of vaterite varies from early to final growth stage. Compared to the fast thermal-decomposition of matured crystalline vaterite and calcite under the electron beam,[43, 44] our TEM studies show that nano-crystalline

vaterite displays much higher resistance to the ionizing irradiation. Similar phenomena were also discovered in other materials (Au, $MgGa_2O_4$, TiNi alloy) where particles with smaller particle size (< 20 nm) are more irradiation resistant than the larger-grained powders [45]. This may be because the aggregations of smaller-size materials contain more crystallite boundaries, where irradiation-induced defects annihilate more easily. Due to the small size of nanoparticles, defects generated by irradiation within the particles are easy to diffuse to the nanoparticle margins and annihilate there [46, 47]. In contrast, defects in larger particles have a stronger tendency to accumulate in the bulk, leading to radiation-induced decomposition, disorder, and amorphization [45, 48-50].

3.4.3 Dislocations caused by the stacking of nanoparticles

Having the nanoparticles, instead of atoms, as the building blocks may explain why vaterite grains contain a large number of dislocations. While crystal growth from single ions allows for the ordered attachment that leads to the formation of single crystals, the aggregation of larger units such as nanoparticles tends to lead to the formation of grain boundaries that typically do not match epitaxially. Therefore, distortions will occur at the interface to compensate for the mismatch, as also previously reported by Penn and Banfield [35]. This theory explains the common occurrence of dislocations in vaterite, as observed in crystal flakes (Fig. 3.9) and the offset between two overlapping hexagonal platelets, as revealed by the TEM diffraction pattern shown in Figure 3.5 D.

The aggregation from nanoparticles, rather than ions, and the resulting mismatching grain boundaries may also inhibit single crystals to grow. The size of the vaterite single crystals (hexagonal platelets), 1-2 μm, is probably the threshold, larger

than which the expansion of the continuously regular order of atoms is most likely to be interrupted.

3.4.4 Building blocks and growth path of vaterite grains of distinguished morphologies

Another interesting discovery is that the various vaterite shapes at *different growth stages* in this study are representatives of the distinctive morphologies that have been reported, such as small spheres [16, 30, 31], plates [27, 51], and layered flower-like morphologies [19, 32]. In addition to the similarities of reported shapes with the shapes at different growth stages in this study, the respective sizes of crystallites with specific morphologies reported in the literature are also similar to the sizes of the corresponding crystallites of different growth stages reported here. Specifically, most of the spherical balls are about a couple of microns, the plates are on the order of 20 μm, and the flower-like structures are 50 –100 μm in diameter.

Another unifying feature of the previously reported vaterite (as long as the published images are clear enough to reveal details at the sub-micron scale) and the ones shown in this study is that they are composed of nano-size clusters, independent of the crystal growth method and independent of the resulting vaterite morphologies. No matter if vaterite formation was induced by polymers [10, 14, 21, 24, 52], amino acids [15, 53], urea [54], bacteria [3], just from highly-supersaturated inorganic solutions [55], or by increasing pH [56], the vaterite surfaces are all rough and exhibit an appearance of an aggregation of nanoparticles. The reason for why vaterite fails to develop by growing continuously to form atomically flat faces but by assemblage of nanoparticles may be because the crystal structure of vaterite is disordered at short range. Kamhi [57] and

Wang and Becker [58] reported that the planar carbonate groups in vaterite may not have fixed positions but tend to randomly distribute over three orientations (the vectors normal to the carbonate plains are perpendicular to the c-axis and there is a 120° angle between these normal vectors). The uncertainty of carbonate-group orientation leads to inconsistent arrangements of atoms at the short range, which can easily result in other defects and structure mismatches, and hence interrupts the continuous growth of well-ordered larger single crystals of vaterite.

3.5 Conclusions

This paper reveals the development and the change of morphology and orientation in different growth stages of vaterite, which was cultivated by the ammonia diffusion method. The observations inspire the hypothesis that the nanoparticles are the common building blocks of most vaterite morphologies. In addition, various morphologies of vaterite may be just intermediate stages of same growth process, which is an assemblage of nanoparticles in an increasingly organized way. A small spheroidal structure (typically less than ten microns in diameter) is the initial stage of this process, composed of nanoparticles of random orientations. The hexagonal plate (≈20 μm) is the intermediate stage. The 6-fold flaky flower-like grain (larger than 50 microns) is the final stage, displaying a crystalline structure assembled by ordered nanoparticles. Due to the limitation caused by the growth environment, vaterite is not always able to develop into the final stage. For example, decreasing supersaturation, templates, growth inhibitors, and other factors can prevent vaterite from growing further. The morphology developed at a particular stage may be the ultimate shape that vaterite develops under a specific condition. The fact that the final growth stage is often a flower-like morphology

with *six* “leaves” is likely not to be a result of the hexagonal crystal structure of vaterite because the composing crystallites have more or less random orientation towards each other. We consider it more likely that this is the result of diffusion-limited growth as in the more macroscopic growth of snowflakes.

Imperfect assemblage of nano-clusters may inhibit single crystals of vaterite to expand to a larger scale and may produce a high density of dislocations inside of vaterite. The nano-crystalline vaterite forming in the early stage has a high resistance to electron bombardment of electron beam under the TEM characterization.

References

1. Braissant, O., et al., *Bacterially induced mineralization of calcium carbonate in terrestrial environments: the role of exopolysaccharides and amino acids.* Journal of sedimentary research, 2003. **73**(3): p. 485-490.
2. Wolf, S.E., et al., *Phase selection of calcium carbonate through the chirality of adsorbed amino acids.* Angewandte Chemie International Edition, 2007. **46**(29): p. 5618-5623.
3. Rodriguez-Navarro, C., et al., *Bacterially mediated mineralization of vaterite.* Geochimica et Cosmochimica Acta, 2007. **71**(5): p. 1197-1213.
4. Lian, B., et al., *Carbonate biomineralization induced by soil bacterium Bacillus megaterium.* Geochimica et Cosmochimica Acta, 2006. **70**(22): p. 5522-5535.
5. Addadi, L., et al., *Mollusk shell formation: A source of new concepts for understanding biomineralization processes.* Chemistry-a European Journal, 2006. **12**(4): p. 981-987.
6. Kanakis, J., et al., *The crystallization of calcium carbonate on porcine and human cardiac valves and the antimineralization effect of sodium alginate.* Journal of Crystal Growth, 2001. **223**(4): p. 557-564.
7. Lowenstam, H. and D. Abbott, *Vaterite: a mineralization product of the hard tissues of a marine organism (Ascidiacea).* Science, 1975. **188**(4186): p. 363-365.
8. Hadiko, G., et al. *Influence of inorganic ion on the synthesis of hollow calcium carbonate*. in *Asian International Conference on Advanced Materials*. 2005. Beijing, People's R China: Trans Tech Publications Ltd.
9. Fuchigami, K., Y. Taguchi, and M. Tanaka, *Synthesis of calcium carbonate vaterite crystals and their effect on stabilization of suspension polymerization of MMA.* Advanced Powder Technology, 2009. **20**(1): p. 74-79.

10. Kasuga, T., et al., *Preparation of poly(lactic acid) composites containing calcium carbonate (vaterite).* Biomaterials, 2003. **24**(19): p. 3247-3253.
11. Kitamura, M., *Crystallization and transformation mechanism of calcium carbonate polymorphs and the effect of magnesium ion.* Journal of Colloid and Interface Science, 2001. **236**(2): p. 318-327.
12. Ogino, T., T. Suzuki, and K. Sawada, *The formation and transformation mechanism of calcium carbonate in water.* Geochimica et Cosmochimica Acta, 1987. **51**(10): p. 2757-2767.
13. Kralj, D., L. Brecevic, and J. Kontrec, *Vaterite growth and dissolution in aqueous solution III. Kinetics of transformation.* Journal of Crystal Growth, 1997. **177**(3-4): p. 248-257.
14. Colfen, H. and M. Antonietti, *Crystal design of calcium carbonate microparticles using double-hydrophilic block copolymers.* Langmuir, 1998. **14**(3): p. 582-589.
15. Grasby, S.E., *Naturally precipitating vaterite (μ-$CaCO_3$) spheres: unusual carbonates formed in an extreme environment.* Geochimica et Cosmochimica Acta, 2003. **67**(9): p. 1659-1666.
16. Fujiwara, M., et al., *Encapsulation of Proteins into CaCO3 by Phase Transition from Vaterite to Calcite.* Crystal Growth & Design, 2010. **10**(9): p. 4030-4037.
17. Hosoda, N., A. Sugawara, and T. Kato, *Template effect of crystalline poly(vinyl alcohol) for selective formation of aragonite and vaterite $CaCO_3$ thin films.* Macromolecules, 2003. **36**(17): p. 6449-6452.
18. Didymus, J.M., et al., *Influence of low-molecular-weight and macromolecular organic additives on the morphology of calcium carbonate.* Journal of the Chemical Society-Faraday Transactions, 1993. **89**(15): p. 2891-2900.
19. Heywood, B.R., S. Rajam, and S. Mann, *Oriented crystallization of $CaCO_3$ under compressed monolayers. 2. morphology, structure and growth of immature crystals.* Journal of the Chemical Society-Faraday Transactions, 1991. **87**(5): p. 735-743.
20. Rieke, P.C., *Selection of phase and control of orientation during physisorption on surfaces of homogeneously formed calcium carbonate nuclei.* Materials Science & Engineering C-Biomimetic and Supramolecular Systems, 1995. **2**(3): p. 181-189.
21. Kun Park, H., I. Lee, and K. Kim, *Controlled growth of calcium carbonate by poly(ethylenimine) at the air/water interface.* Chemical Communications, 2004(1): p. 24-5.
22. Rudloff, J. and H. Colfen, *Superstructures of temporarily stabilized nanocrystalline $CaCO_3$ particles: Morphological control via water surface tension variation.* Langmuir, 2004. **20**(3): p. 991-996.
23. Lee, H.S., T.H. Ha, and K. Kim, *Fabrication of unusually stable amorphous calcium carbonate in an ethanol medium.* Materials Chemistry and Physics, 2005. **93**(2-3): p. 376-382.
24. Shen, Q., et al., *Crystallization and aggregation behaviors of calcium carbonate in the presence of poly(vinylpyrrolidone) and sodium dodecyl sulfate.* Journal of Physical Chemistry B, 2005. **109**(39): p. 18342-18347.
25. Jada, A. and A. Verraes, *Preparation and microelectrophoresis characterisation of calcium carbonate particles in the presence of anionic polyelectrolyte.* Colloids

and Surfaces A: Physicochemical and Engineering Aspects, 2003. **219**(1-3): p. 7-15.
26. Malkaj, P., J. Kanakis, and E. Dalas, *The effect of leucine on the crystal growth of calcium carbonate.* Journal of Crystal Growth, 2004. **266**(4): p. 533-538.
27. Gehrke, N., et al., *Superstructures of calcium carbonate crystals by oriented attachment.* Crystal Growth & Design, 2005. **5**(4): p. 1317-1319.
28. Liu, D.X. and M.Z. Yates, *Formation of rod-shaped calcite crystals by microemulsion-based synthesis.* Langmuir, 2006. **22**(13): p. 5566-5569.
29. Spanos, N. and P.G. Koutsoukos, *Kinetics of precipitation of calcium carbonate in alkaline pH at constant supersaturation. Spontaneous and seeded growth.* Journal of Physical Chemistry B, 1998. **102**(34): p. 6679-6684.
30. Watanabe, J. and M. Akashi, *Controlled deposition of calcium carbonate particles on porous membranes by using alternating current system.* Journal of Colloid and Interface Science, 2008. **327**(1): p. 44-50.
31. Han, Y., et al., *Influence of initial $CaCl_2$ concentration on the phase and morphology of $CaCO_3$ prepared by carbonation.* Journal of Materials Science, 2006. **41**(14): p. 4663-4667.
32. Fricke, M., et al., *Vaterite polymorph switching controlled by surface charge density of an amphiphilic dendron-calix[4]arene.* Crystal Growth & Design, 2006. **6**(5): p. 1120-1123.
33. Allison, J.D., D.S. Brown, and K.J. Novo-Gradac, *MINTEQA2/PRODEFA2, a geochemical assessment model for environmental systems: Version 3. 0 user's manual*, in *US Environmental Protection Agency, Athens, GA*. 1991. p. 117
34. Huang, F., H. Zhang, and J.F. Banfield, *Two-stage crystal-growth kinetics observed during hydrothermal coarsening of nanocrystalline ZnS.* Nano Letters, 2003. **3**(3): p. 373-378.
35. Penn, R.L. and J.F. Banfield, *Imperfect oriented attachment: dislocation generation in defect-free nanocrystals.* Science, 1998. **281**(5379): p. 969-971.
36. Teng, H.H., P.M. Dove, and J.J. De Yoreo, *Kinetics of calcite growth: surface processes and relationships to macroscopic rate laws.* Geochimica et Cosmochimica Acta, 2000. **64**(13): p. 2255-2266.
37. Davis, K.J., P.M. Dove, and J.J. De Yoreo, *The role of Mg^{2+} as an impurity in calcite growth.* Science, 2000. **290**(5494): p. 1134-1137.
38. Henriksen, K., et al., *Biological control on calcite crystallization: AFM investigation of coccolith polysaccharide function.* American Mineralogist, 2004. **89**(11-12): p. 1709-1716.
39. Teng, H.H., et al., *Thermodynamics of calcite growth: Baseline for understanding biomineral formation.* Science, 1998. **282**(5389): p. 724-727.
40. Larsen, K., K. Bechgaard, and S.L.S. Stipp, *Modelling spiral growth at dislocations and determination of critical step lengths from pyramid geometries on calcite {10-14} surfaces.* Geochimica et Cosmochimica Acta, 2010. **74**(2): p. 558-567.
41. Hillner, P.E., et al., *Atomic-scale imaging of calcite growth and dissolution in real time.* Geology, 1992. **20**(4): p. 359-362.

42. Walters, D.A., et al., *Modification of calcite crystal growth by abalone shell proteins: an atomic force microscope study.* Biophysical Journal, 1997. **72**(3): p. 1425-1433.
43. Murooka, Y. and J. Yuan. *Electron-beam-induced nanoscale chemical-reactions.* in *Electron Microscopy and Analysis*. 1993
44. Xu, G., et al., *Biomimetic synthesis of macroscopic-scale calcium carbonate thin films. Evidence for a multistep assembly process.* Journal of the American Chemical Society, 1998. **120**(46): p. 11977-11985.
45. Zhang, J.M., et al., *Enhanced radiation resistance of nanocrystalline pyrochlore $Gd_2(Ti0.65Zr0.35)_2O_7$.* Applied Physics Letters, 2009. **94**(24): p. 243110-3.
46. Shen, T.D., et al., *Enhanced radiation tolerance in nanocrystalline $MgGa_2O_4$.* Applied Physics Letters, 2007. **90**(26): p. 263115-3.
47. Chimi, Y., et al., *Accumulation and recovery of defects in ion-irradiated nanocrystalline gold.* Journal of Nuclear Materials, 2001. **297**(3): p. 355-357.
48. Meldrum, A., et al., *Heavy-ion irradiation effects in the ABO_4 orthosilicates: Decomposition, amorphization, and recrystallization.* Physical Review B, 1999. **59**(6): p. 3981.
49. Ewing, R., W. Weber, and J. Lian, *Nuclear waste disposal—pyrochlore ($A_2B_2O_7$): Nuclear waste form for the immobilization of plutonium and "minor" actinides.* Journal of Applied Physics, 2004. **95**: p. 5949-5971.
50. Lian, J., et al., *Nanoscale manipulation of pyrochlore: new nanocomposite ionic conductors.* Physical Review Letters, 2001. **87**(14): p. 145901.
51. Dupont, L., F. Portemer, and M. Figlarz, *Synthesis and study of a well crystallized $CaCO_3$ vaterite showing a new habitus.* Journal of Materials Chemistry, 1997. **7**(5): p. 797-800.
52. Kim, I.W., R.E. Robertson, and R. Zand, *Effects of some nonionic polymeric additives on the crystallization of calcium carbonate.* Crystal Growth & Design, 2005. **5**(2): p. 513-522.
53. Tong, H., et al., *Control over the crystal phase, shape, size and aggregation of calcium carbonate via a l-aspartic acid inducing process.* Biomaterials, 2004. **25**(17): p. 3923-3929.
54. Wang, L., I. Sondi, and E. Matijevic, *Preparation of uniform needle-like aragonite particles by homogeneous precipitation.* Journal of Colloid and Interface Science, 1999. **218**(2): p. 545-553.
55. Sohnel, O. and J.W. Mullin, *Precipitation of calcium carbonate.* Journal of Crystal Growth, 1982. **60**(2): p. 239-250.
56. Han, Y.S., et al., *Crystallization and transformation of vaterite at controlled pH.* Journal of Crystal Growth, 2006. **289**(1): p. 269-274.
57. Kamhi, S., *On the structure of vaterite $CaCO_3$.* Acta Crystallographica, 1963. **16**(8): p. 770-772.
58. Wang, J. and U. Becker, *Structure and carbonate orientation of vaterite ($CaCO_3$).* American Mineralogist, 2009. **94**(2-3): p. 380-386.

CHAPTER FOUR
TEMPLATED NUCLEATION OF CALCITE IMPOSED BY MHA AND MUA SELF-ASSEMBLED MONOLAYERS

ABSTRACT: Self-assembled monolayers (SAMs) made of alkanethiol molecules have been frequently used as a simple model to reproduce the function of natural templates. Although a mechanistic understanding of templating requires knowledge of the thermodynamic and kinetic barriers, no experimental work has been done to quantify these factors. Moreover, the importance of indirect nucleation pathways via amorphous precursors during templating remains unresolved. This study uses the relation between supersaturation and the nucleation rate to determine the interfacial energies between template-directed calcite nuclei and 16-mercaptohexadecanoic acid (MHA) and 11-mercaptoundecanoic acid (MUA) SAMs. Whether the nucleation occurs via the amorphous phase is also investigated. The results reveal that (1) MHA and MUA both significantly reduce the effective surface energy of calcite from about 97 mJ/m^2 in solution to about 45.3±2.9 and 47.2±2.4 mJ/m^2 on MHA and MUA, respectively, demonstrating that the bias towards nucleation on these films with (01x) orientations of calcite (such as (012) and (013)) is caused by reduction of the free energy barrier to nucleation, which is a thermodynamic driver; and (2) at solute activities below the solubility limit of amorphous calcium carbonate, or slightly above this limit, calcite forms directly.

4.1 Background

The need for carbon sequestration becomes increasingly significant with the growing threat of global warming. With CO_2 storage in underground geological settings to be one of the leading strategies to address this challenge, controlling and enhancing $CaCO_3$ deposition will take center stage in the coming decades [1]. Organic templates in living systems are believed to have strong effects on $CaCO_3$ precipitation, especially on its morphology, crystallographic orientation, and precipitation rate [2-7]. Due to the presence of microbial colonies, organic films are likely to be present in shallow to moderately deep reservoirs. Moreover, organic molecules that mimic proteins associated with carbonate mineralization and enhanced calcite growth rates are being considered as potential additives in sequestration environments (Chung et al., 2011). This suggests that efforts must be made towards a solid understanding of how organic substrates affect carbonate crystallization.

Due to the extreme complexities of real organic systems, in order to obtain a solid understanding of the bio-influence, a simple model of SAMs has been frequently used to reproduce the function of organic templates [9, 10]. In particular, SAMs made of alkanethiol molecules have demonstrated to effectively induce highly-oriented nucleation of calcite [9, 11-13].

A thorough understanding of the SAM-calcite system requires an accurate assessment of kinetic and thermodynamic origins of this effect, such as the nucleation energy barriers to calcite formation as determined by the interfacial energies between calcite nuclei and the SAMs.

However, no work has been done to estimate the interfacial energy. This study uses a unique method to evaluate the effective interfacial energy (α), by considering the dependence of the nucleation rate (J_n) on the supersaturation (σ) of the salt solution. σ is defined as $\ln(\frac{a(\mathrm{Ca^{2+}})\cdot a(\mathrm{CO_3^{2-}})}{\mathrm{Ksp}})$ where $a(\mathrm{Ca^{2+}})$ and $a(\mathrm{CO_3^{2-}})$ are the activities of Ca^{2+} and CO_3^{2-}, respectively.

The relation between α, J_n, and σ is derived from the first thermodynamic law that states when the nucleation takes place, the free energy change (positive) is the difference between the free energy per molecule of the bulk (Δg_b) and that of the surface (Δg_s):

$$\Delta \boldsymbol{g} = \Delta \boldsymbol{g_b} + \Delta \boldsymbol{g_s} \tag{4.1}$$

When the driving force, varying with supersaturation (σ), overcomes the maximum value of Δg, nucleation could happen, and the corresponding rate is the nucleation rate J_n. For heterogeneous nucleation, such as calcite nucleating on SAMs, there are two interfacial energies to consider, one between the crystal and solution, and the other between the crystal and the substrate, which could be written as:

$$\Delta g = -\frac{V}{\Omega}\Delta\mu + A_b(\alpha_{sc} - \alpha_{ls}) + \mathrm{A_s}\alpha_{lc} \tag{4.2}$$

where V is the volume of the nucleus, Ω is, in this case, the volume of one formula unit of $CaCO_3$ (*i.e.*, the molar volume of calcite divided by Avogadro's number), $\Delta\mu$ is the chemical potential of the crystallizing species, A_b is the contact area between the nuclei and the substrates, A_S is the contact area between the substrate and the liquid, the subscripts "sc", "lc", and "ls" refer to substrate-crystal, liquid-crystal, and liquid-

substrate, respectively. $\Delta\mu = k_B T \ln\sigma$ where k_B is the Boltzmann constant and T is temperature. If we assume, for simplicity, that the nucleus is a hemisphere of radius r, we have:

$$\Delta g = -\frac{\frac{2}{3}\pi r^3}{\Omega} k_B T \ln\sigma + \pi r^2 (2\alpha_{lc} + \alpha_{sc} - \alpha_{ls}). \quad (4.3)$$

This equation shows that the driving force, or the nucleation rate, depends the differences of interfacial energies the crystalline/liquid and crystalline/substrate interfaces. Δg reaches its maximum when $\frac{d\Delta g}{dr} = 0$, in which case the value of r is known as the critical radius, r_c, given by:

$$r_c = \frac{\Omega(2\alpha_{lc} + \alpha_{sc} - \alpha_{ls})}{k_B T \sigma}. \quad (4.4)$$

The solution will crystallize eventually if supersaturated, but the probability of nuclei forming within a certain time range varies with supersaturation state. If there is a nucleation barrier, the maximum value of Δg determines the kinetics of nucleation, and by combining Eqns. (4.3) and (4.4), Δg can be expressed as:

$$\Delta g = \frac{\frac{16}{3}\pi \alpha'^3 \Omega^2}{(k_B T \sigma)^2}, \quad (4.5)$$

where $\alpha' = \alpha_{lc} + \frac{\alpha_{sc} - \alpha_{ls}}{2}$. As with any kinetically-limited chemical process, the nucleation probability is proportional to the exponential of the barrier height (Δg_n), which can be written as:

$$J_n = A \exp\left(-\frac{\Delta g_n}{k_B T}\right), \quad (4.6)$$

or:

$$J_n = A\exp\left(-\mathrm{B}\frac{\alpha'^3}{\sigma^2}\right), \tag{4.7}$$

where *A* is a kinetic factor that governs nucleation frequency, *B* is a coefficient related to Ω, the value of k_BT, and the morphology of the nuclei, α' is the effective interfacial energy, and Ksp is the equilibrium solubility product.

By rearranging the Eqn. (4.7):

$$\ln\left(J_n\right) = -\mathrm{B}\alpha'^3\frac{1}{\sigma'^2} + \ln\mathrm{A}, \tag{4.8}$$

which shows that $\ln\left(J_n\right)$ has a linear relationship with $\frac{1}{\sigma'^2}$, and the effective interfacial energy (α') can be obtained from the slope, $-\mathrm{B}\alpha'^3$.

In order to obtain values for the interface energy, a series of solutions of different concentrations were prepared, measured the nucleation rates, and extracted the effective interfacial energy from the linear relationship in Eqn. (4.8).

We selected two intensively studied SAMs to be analyzed: 16-mercaptohexadecanoic acid (MHA) and 11-mercaptoundecanoic acid (MUA). MHA and MUA are both -COOH terminated, but of different lengths of the carbon chain with MHA having 16-carbons and MUA 11. MHA and MUA induce nucleation of calcite on the structurally distinct non-natural (012) and (013) faces, respectively [10], thus demonstrating the so-called odd/even effect of SAM templating. These planes are easily differentiated from the normal calcite (104) plane, which helps to assess whether nucleation is controlled by the SAMs.

The nucleation pathway, either directly to the crystalline phase or via amorphous calcium carbonate (ACC) as a transient phase, is another topic of this study. ACC plays a fundamental role in many $CaCO_3$ formation processes. For example, the isotropic nature of ACC allows it to be easily shaped in vesicles and aligned along certain directions to build up the organism [14]. It has been reported that growing sea urchin and bivalve larvae make ACC as a transient phase that transforms to crystalline calcium carbonate [15-19]. One ongoing debate is whether this strategy is widespread amongst organisms that form crystalline $CaCO_3$. More importantly, recent studies have argued that calcite *always* forms through this indirect pathway and does so through aggregation of pre-existing amorphous clusters (Gebauer and Coelfen, 2008; Pouget et al., 2009). However, both of these studies created solution conditions that were highly supersaturated with respect to ACC rather than most environmental conditions that result in supersaturation with respect to calcite, but not necessarily with respect to ACC. Finally, a previous study that explicitly looked at the initial $CaCO_3$ phase on alkyl thiol SAMs during mineralization by diffusing-in carbonate [20] reported that, indeed, a transient ACC phase formed prior to transformation into oriented calcite. However, the supersaturation state in that experimental configuration could not be quantified. In fact, among the many studies reporting ACC formation, most did not analyze the supersaturation of the salt solutions [12, 21-24]. For the studies mentioning the Ca^{2+} and CO_3^{2-} concentrations used, the solutions are highly supersaturated with respect to ACC [25-27], with supersaturations with respect to ACC higher than 1.3 as calculated by MINTEQ [28].

These observations raise the obvious question of whether transient ACC is a general precursor to calcite or whether its appearance requires supersaturations well in

excess of the ACC solubility limit. This study analyzed nucleation over a range of supersaturations from well below the solubility limit of ACC to well above, to determine whether ACC formation requires a supersaturation above a certain threshold.

4.2 Experimental procedure

4.2.1 SAMs preparation

A 100 nm-thick film of Au (111) was deposited under high vacuum on a Si (100) wafer that was first coated with 5 nm Cr as an adhesion promoter. The gold substrates were analyzed by AFM, which revealed a uniform and sufficiently flat film of gold particles about 1-2 nm in height. The MHA and MUA monolayers on gold surfaces were carried out by immersing gold substrates for 24 to 30 hours into 2 mM MHA or MUA solutions of 95% ethanol and 5% acetic acid. After removal from the ethanolic solutions, the gold substrates were thoroughly rinsed with the corresponding pure solvent, 5% acetic acid in ethanol, and then dried by flow of nitrogen gas. SAMs were covered by DI water to eliminate potential oxidization and then instantly placed in the flow cell.

4.2.2 Experimental setup and measurements

The schematic image of the experimental setup is illustrated in Figure 4.1. $CaCl_2$ was injected first and then mixed with $NaHCO_3$ of equivalent concentrations to give a better controlled face-selective nucleation [29]. The mixed solution was channeled through the flow cell through tubing. Different flow rates from 0.5 to 5 mL/min were tested, and it was found that $CaCO_3$ nucleates faster as the flow rate increases from 0.5 to 2 mL/min but does not change if the rate is higher since the supply exceeds the consummation of ions for crystal formation. Therefore, the flow rate was set to 2 mL/min, to yield nucleation rates independent of flow rate. This ensured that the

nucleation was not limited by diffusion but was controlled by the nucleation reaction at the SAM surface. Various lengths of tubing were applied for trail experiments for an appropriate value. Tubing that was too short would fail to provide a thoroughly mixed of salt solution and hence less precipitates, whereas too long of a tubing would lead to precipitation occurring in the tubing and would hence provide less ions for nucleation in the fluid cell. It turns out that under the same concentration, the tubing of around 38 cm length provided the highest number of nuclei in the fluid cell. SAMs and bare gold substrates were placed upside down in the flow cell, to ensure only the heterogeneous nuclei were bound to the substrates. The development of $CaCO_3$ crystals on the SAMs was imaged *in situ* using an inverted optical microscope. The large number of nuclei that occur in the working area ($0.65 \cdot 0.49$ mm^2) of the optical microscope bestows large data for statistical analysis. Because the critical radius of a $CaCO_3$ nucleus was well below the resolution limit of the optical system, the nuclei were too small to be observed by the optical microscope at the instant of formation, so we assume each nucleus develops into one crystal. This assumption is reasonable because in our study the nucleation density is so low that the average distance between neighboring nuclei is longer than 10 μm, which is well in excess of the size at which the nuclei become visible. Therefore, the rate of appearance of the crystals can be considered as the nucleation rate. As we show below, the linear dependence between number of nuclei and time after the onset of nucleation validates this assumption. For each concentration, the number of crystals in a fixed area was plotted vs. time, and the slope of the linearly increasing part of the curve was taken as the nucleation rate.

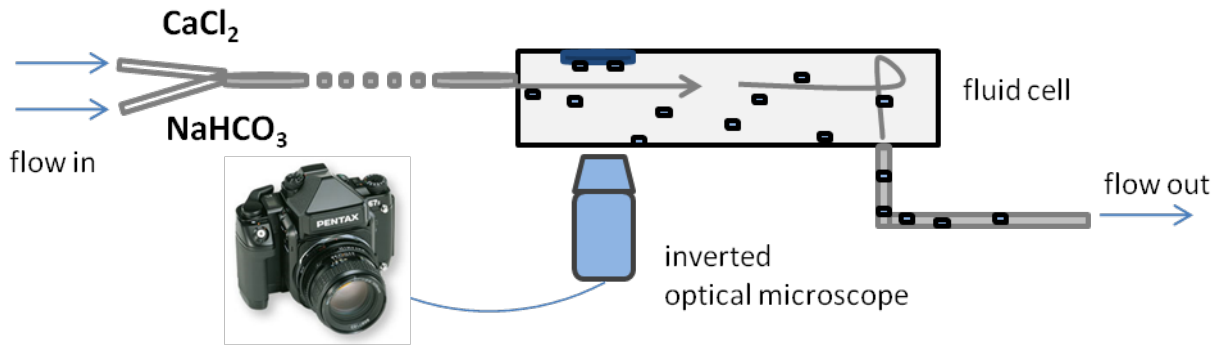

Figure 4.1 Schematic image of the experimental setup

Table 4.1 Polymorph compositions of $CaCO_3$ precipitates on MHA, MUA, bare gold, OH-terminated SAMs as studied by optical microscopy, SEM and Micro-Raman

	20- 29mM	**30mM**	**31-60mM**	**62.5mM and higher**
supersaturation* –calcite**	4.368—4.812	4.853	4.853—5.671	>5.720
supersaturation – ACC**	-0.437– 0.007	0.048	0.048—0.856	> 0.856
phase-on MHA	calcite	calcite	--	--
phase-on MUA	calcite	calcite	--	--
phase-on bare gold/OH-terminated SAM	calcite +aragonite +vaterite	calcite	calcite	ACC first, then calcite

*supersaturation: $\sigma = \log\left(\frac{a(Ca^{2+})\cdot a(CO_3{}^{2-})}{Ksp}\right)$

** $10^{-8.48}$ and $10^{-6.393}$ are used as solubility product of calcite and ACC [8].

A series of solutions of different concentrations were applied and three repeating runs were conducted for each concentration used in this study: 10 mM, 18 mM, 20 mM, 21 mM, 22.5 mM, 24 mM, 25 mM, 26 mM, 27 mM, 28 mM, 29 mM, and 30 mM. Beyond this concentration range, we found that nucleation rates were either too fast or too slow to be successfully analyzed. The activities of Ca^{2+} and CO_3^{2-}, and supersaturation of calcite and ACC were calculated using MINTEQ [28] (Table 4.1). The equilibrium solubility products (Ksp) of calcite and ACC were based on the values of $10^{-8.48}$ and $10^{-6.393}$ [8].

Two methods were used to examine whether ACC forms as the precursor to calcite. The first method involved centrifuging 50mL of 30 mM salt solution, collecting the $CaCO_3$ precipitates from the solutions right after the incubation time and immediately dehydrating them using pure alcohol. The phases of the precipitates were analyzed using a Micro-Raman technique.

Considering that the lifetime of ACC might be too short to be preserved at low pH (lower than 8 in our study), and since ACC precursor phase is often observed at pH higher than 10 [25, 27], we used a second method to stabilize the ACC if it was in fact being produced. We conducted crystallization at concentrations from 30 mM to 125 mM, using the experimental setup illustrated in Figure 4.1, but using OH-terminated SAMs of mercaptophenol (MP) on Au as the substrates. Reactions were quenched by ethanol in the very early stage, after 2-3 minutes, and then the precipitates on the SAMs were immediately dried by N_2 gas. Alkanethiols terminated in OH- groups are reported to favor the formation of ACC but suppresses the nucleation of calcite (Aizenberg et al., 2003), especially MP, which is able to stabilize ACC for a few hours [20]. Therefore, if

ACC did form on MP, it should be detected after the reaction was quenched in the first a couple of minutes. The morphology of the precipitates was determined by both SEM and optical microscopy. The polymorphic composition of the precipitates was analyzed using SEM and Micro-Raman. The areal densities of precipitates on the SAMs, on bare gold, and on the walls of the quartz fluid cell were analyzed using the optical microscopy and SEM.

4.3 Results and discussion

4.3.1 Direct crystallization of calcite at low concentrations

The saturation state with respect to ACC crosses over from being undersaturated to supersaturated at about 29 mM. Since the supersaturation value σ_{ACC} of ACC is negative when the concentration is less than 28 mM (σ_{ACC} = - 0.035), while at 30 mM, it is slightly positive (σ_{ACC} = +0.048). Nonetheless, the development of ACC was not observed in 30 mM solutions in our study. Precipitates collected right after the incubation time displayed three types of morphologies under the optical microscope: rhombohedron, sphere, and small dot (Fig. 4.2 A). The corresponding Raman patterns of all three morphologies (Fig. 4.2 B) display characteristic calcite peaks: 154 cm^{-1}, 284 cm^{-1},710 cm^{-1} and 1084 cm^{-1} [30, 31]. However, the distinctive broad peak of ACC at 150-300 cm^{-1} [14, 32] does not occur in any of the patterns. Since the volume of the "dots" reaches the lower detection limit of Micro-Raman, its peaks are not as sharp as the ones from the other two morphologies. (The 520 cm^{-1} peak is that of Si from silicon wafer.) The high-resolution SEM images (Figs. 4.2 C and D) further demonstrate that the "spheres" and "dots" observed in the optical images actually possess somewhat rhombohedral shapes, implying an underlying calcite structure.

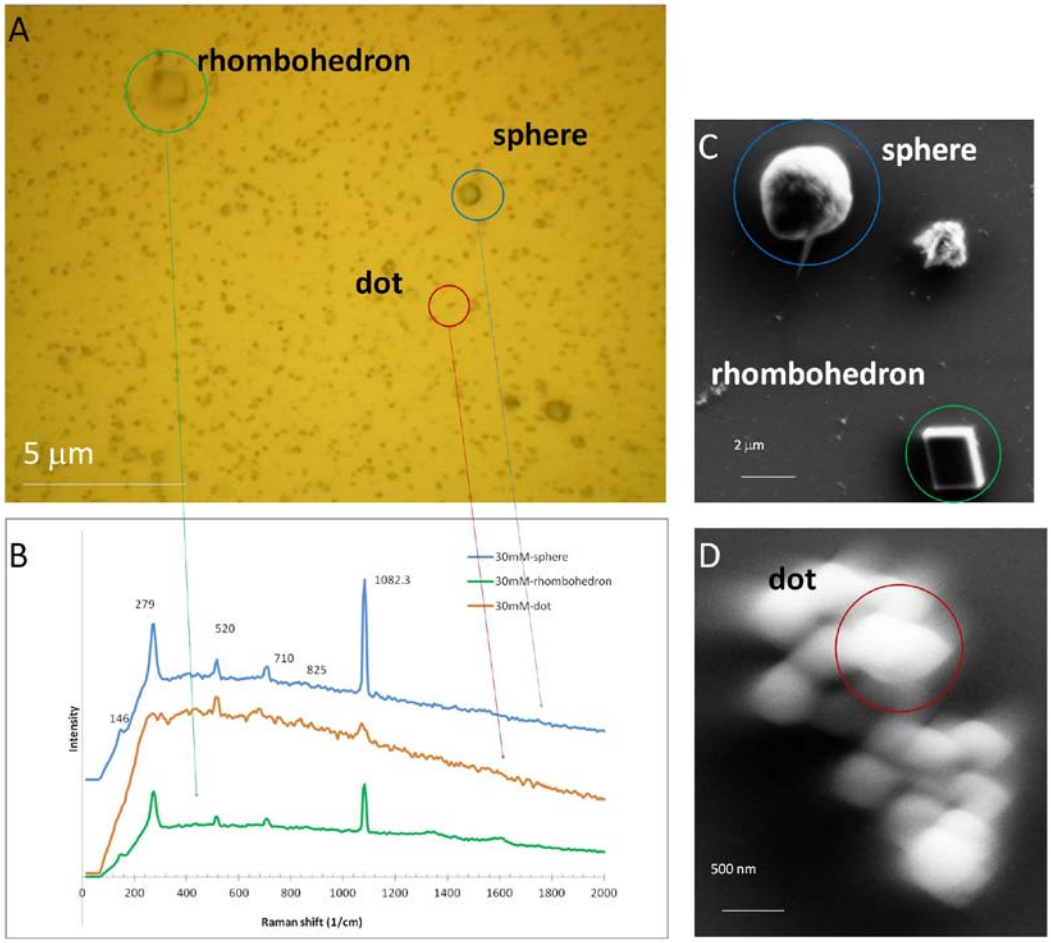

Figure 4.2 Typical micro-Raman patterns demonstrate that the particles forming immediately after the incubation time of 30mM solutions are crystalized calcite. (A) optical microscope image of Micro-Raman showing different types of $CaCO_3$ crystal particles collected on gold 1 minute 15 seconds after mixing 30mM Ca-CO_3 solutions, (B) corresponding Micro-Raman patterns analysis, (C) and (D) SEM images of different morphologies of $CaCO_3$.

When the concentration is equal or higher than 62.5 mM (σ_{ACC} = +0.397), ACC is identified by optical microscopy, SEM, and Micro-Raman (Fig. 4.3 C and D, Fig. 4.4). As was observed in the study of Lee et al., 2007, which created supersaturated conditions through diffusion-in of carbonate, the ACC formed a fairly uniform film in which calcite crystals nucleated and grew, creating a surrounding circular zone denuded of ACC. In the solutions with concentrations between 30 mM to 60 mM, ACC was not detected. Neither the film of ACC nor the denuded zone that surrounds the crystals formed at 62.5 mM or higher concentrations was observed under either the optical microscope or the SEM (Fig. 4.3 A and B). In addition, Micro-Raman patterns did not display characteristic ACC peaks (data not shown here).

The above results suggest that, in the range of pH used here (7-8.5), ACC does not form as a precursor to calcite in solutions that are undersaturated or slightly oversaturated with respect to ACC ($\sigma_{ACC} \leq +0.866$). This phenomenon might be due to the kinetic barriers of ACC nucleation. When supersaturation (σ) of ACC is very low, the energy barrier of nucleation, which is proportional to $1/\sigma^2$, would be sufficiently high to result in a tremendously low ACC nucleation probability [33]. Meanwhile, fast calcite nucleation consumes the Ca^{2+} and CO_3^{2-} ions in solution that reduces the σ of ACC even more. In addition, the formed crystallized calcite further destabilizes any amorphous phase forming temporarily.

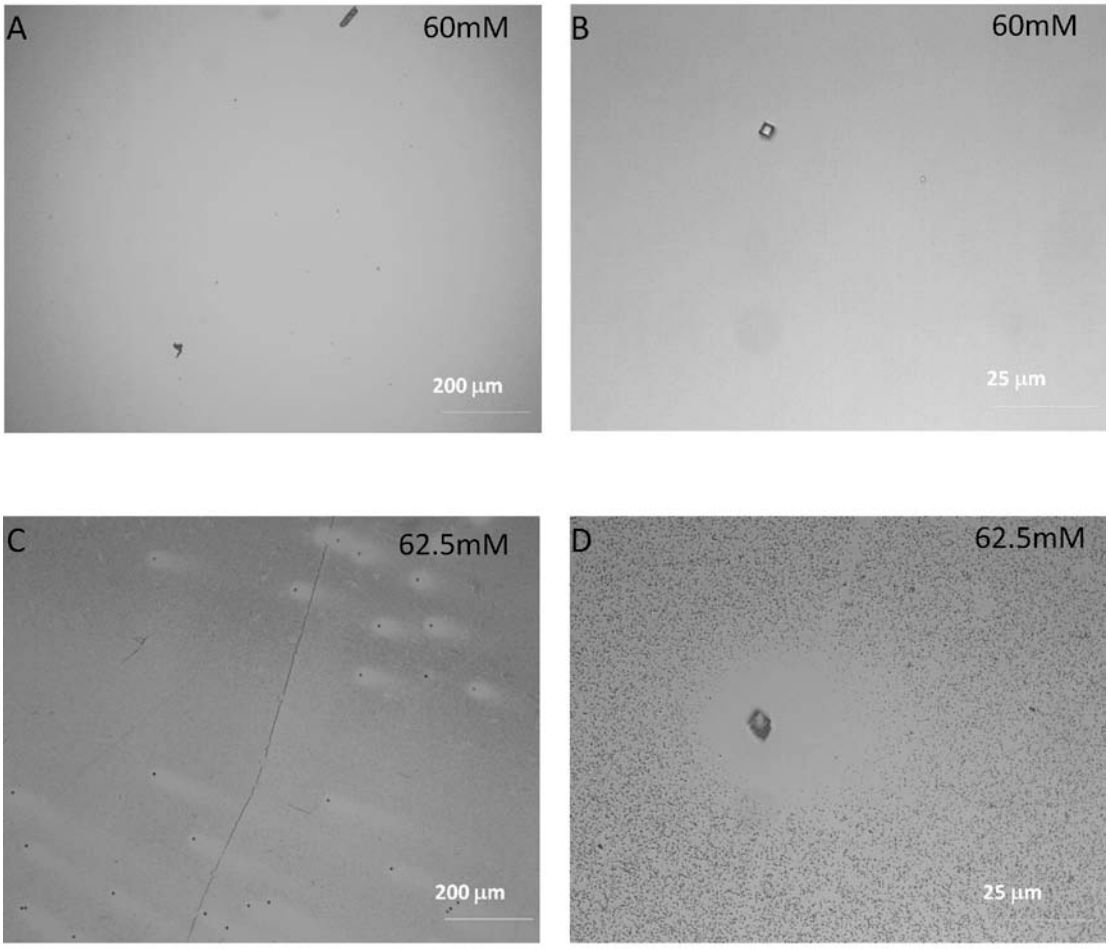

Figure 4.3 Typical optical images of $CaCO_3$ precipitates from the solutions of 60mM and 62.5 mM in the early stage on OH-terminated SAMs, mercaptophenol (MP). At the concentrations equal or lower than 60 mM, only calcite was observed. At the concentration of 62.5 mM or higher, ACC is detected as a fairly uniform film in which calcite crystals nucleated and grew, creating a surrounding circular zone denuded of ACC.

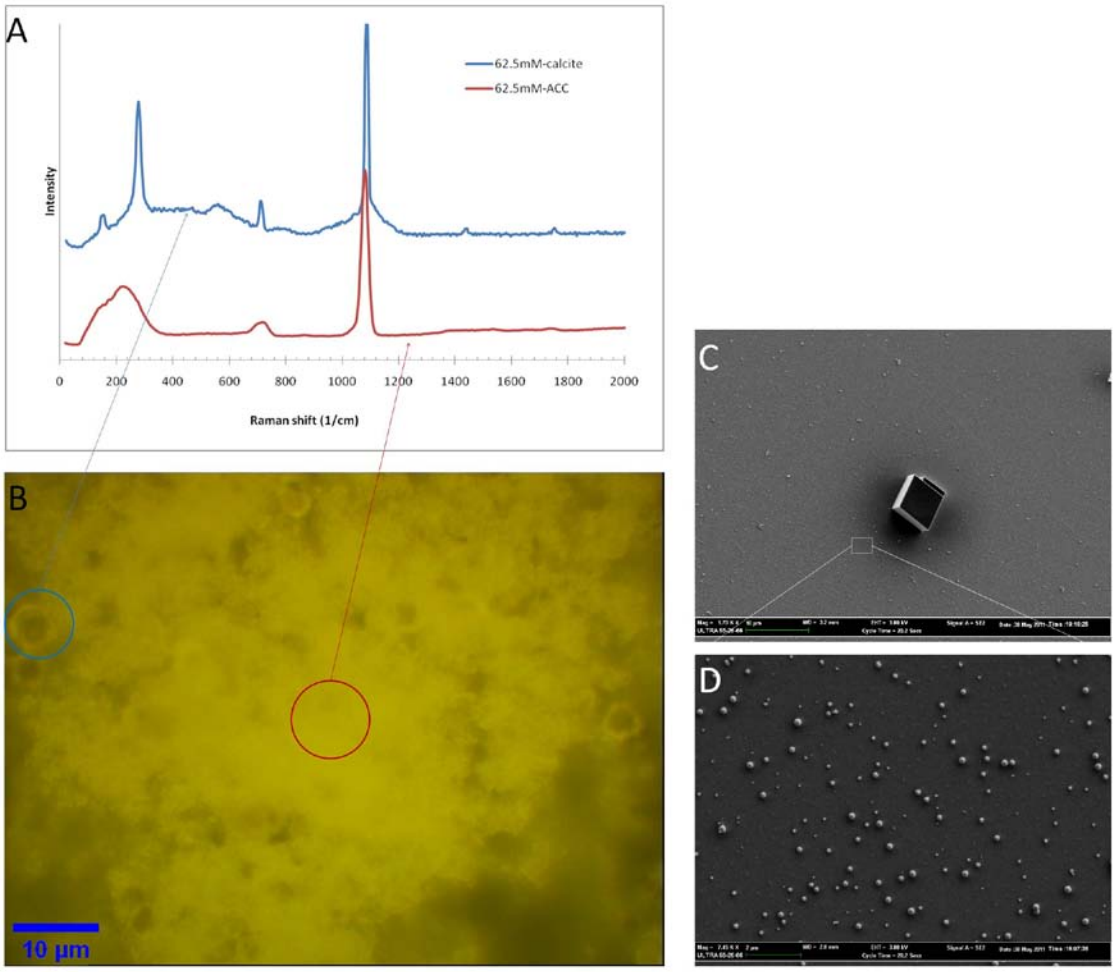

Figure 4.4 (A) Micro-Raman patterns of amorphous and crystalline particles collected on gold two minutes after the reaction from the solution of 62.5 mM, (B) the corresponding optical microscope image of the Micro-Raman, (C) and (D) SEM images displaying the uniform film of ACC and the circular zone denuded of ACC surrounding calcite crystal.

4.3.2 Crystal orientation and density

Calcite precipitates on SAMs exhibit higher areal density and are of much higher uniformity in orientation as compared to their counterparts on bare gold and quartz cuvettes. Most of the crystals that grow on quartz cuvette walls are rhombohedra exposing (104) faces. On bare gold, calcite crystals express random faces. In contrast, the >90% of the calcite crystals exhibit nucleation planes of (012) on MHA and (013) on MUA (Fig. 4.5 A and B). Another interesting phenomenon is that on bare gold, the phase is not exclusively that of calcite, but also includes that of vaterite and aragonite, as confirmed by SEM and Micro-Raman (Fig. 4.5 C and 4.6). This might be because the 7.06 Å lattice spacing of gold (111) [34] does not match that of calcite (104) and hence does not induce its epitaxial growth. Perhaps the planes of vaterite or aragonite make a better match and hence the interfacial energies are lower than that of calcite (104), allowing the other phases to develop.

The precipitate densities on both gold and quartz cuvettes are dramatically lower than those on MHA and MUA, indicating these two SAMs *promote* nucleation relative to the other substrates. To further discern the mechanism of template calcite nucleation by SAMs, their interfacial energies were evaluated.

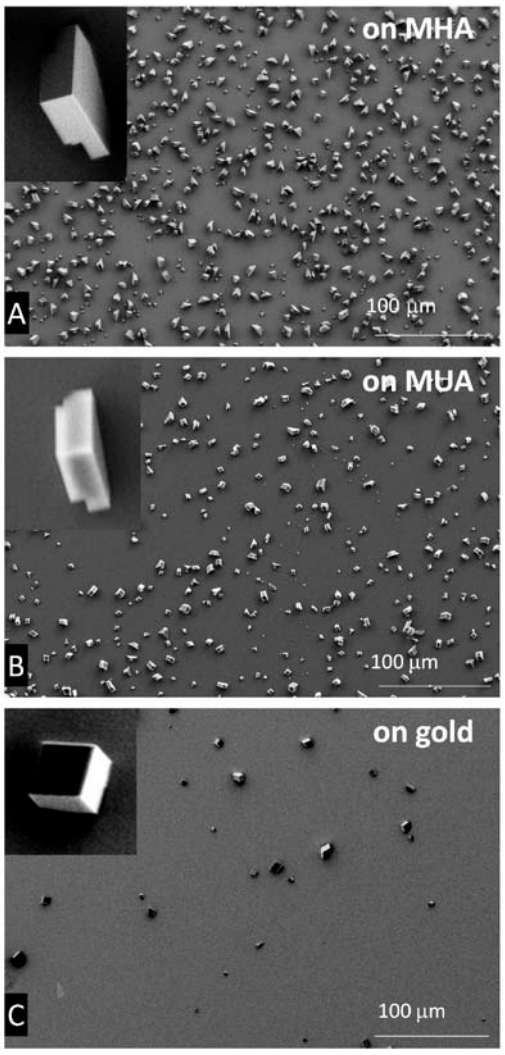

Figure 4.5 Representative SEM images showing calcite crystals with specific orientations and different precipitation densities of precipitates on MHA, MUA, and bare gold. The concentrations of the calcium carbonate solution in all three cases are 30 mM.

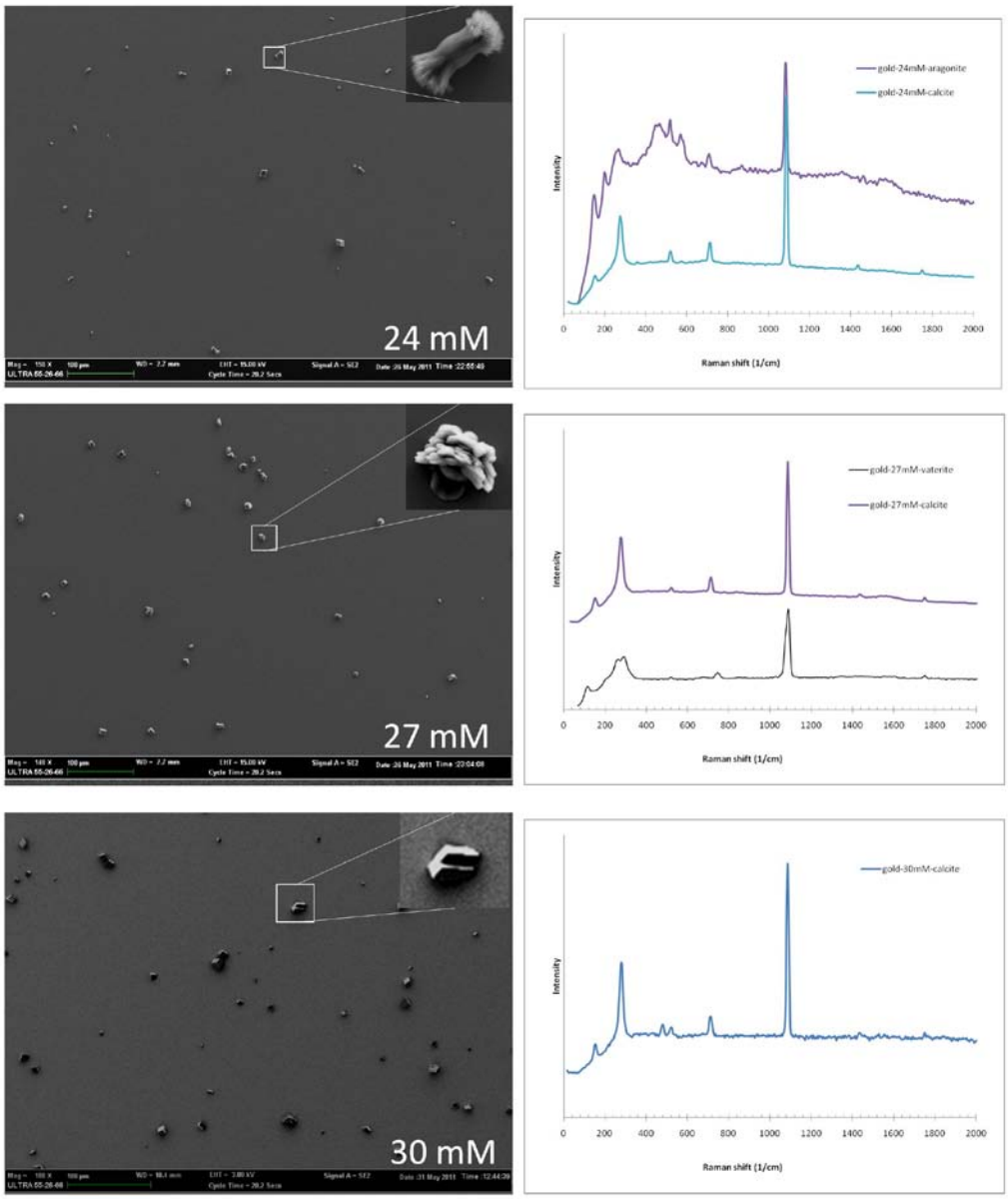

Figure 4.6 Characteristic SEM images and micro-Raman spectra display that on bare gold, calcite is not the only phase. Aragonite and vaterite also form in solutions of 20-29 mM. Calcite becomes the dominant phase in the solution of concentrations equal or higher than 30mM.

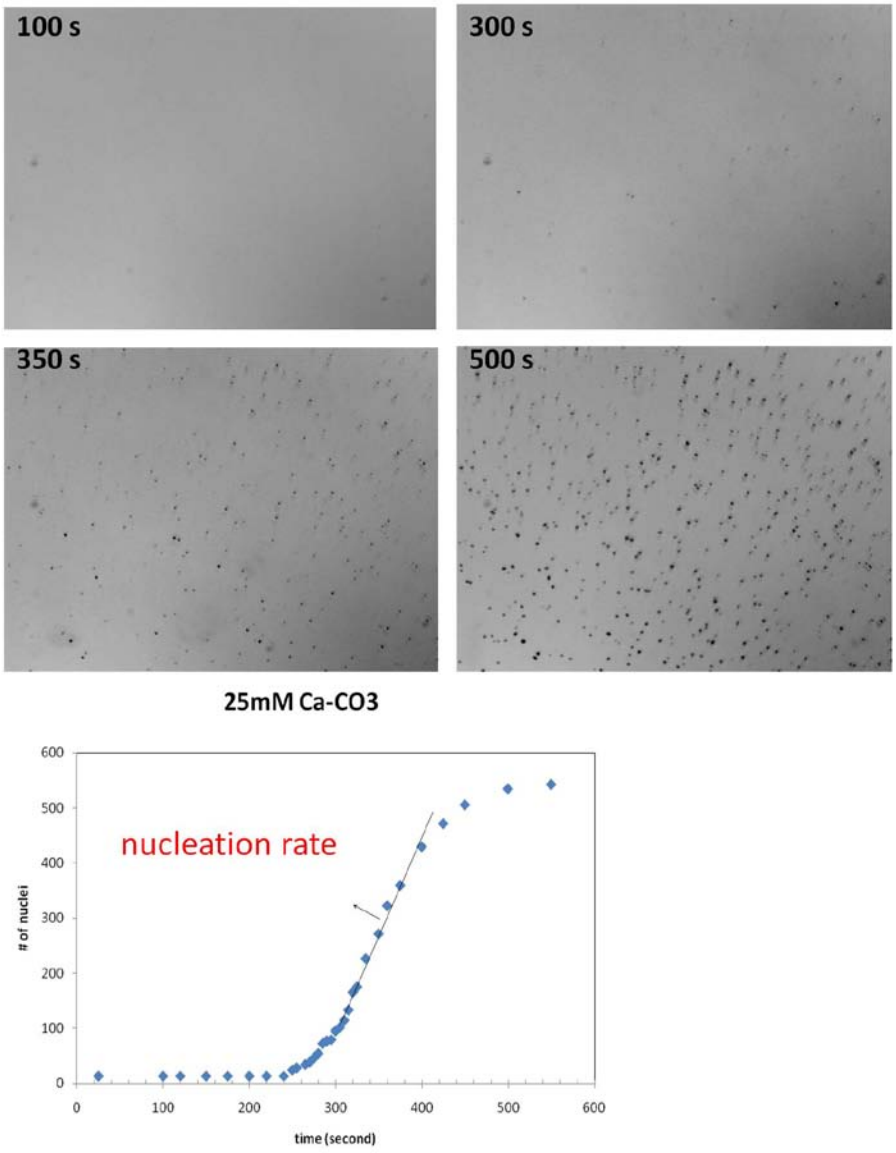

Figure 4.7 Aerial nucleation densities are obtained by counting nuclei in a given area in SEM images like the ones shown above. Nucleation rates are then obtained by the change of the number of nuclei per area over time in the time range that obeys Eqn. 4, that is before saturation leads to a slow-down of nucleation.

During the initial induction period, the solution entering the fluid cell was clear. After some period of time, the formation of crystals in the fluid cell was observed. At the same time, calcite crystals were observed to form on the MHA and MUA SAMs. Subsequently, the number of the crystals per unit area increased linearly with time before reaching saturation. The latter was a clear indication that the inter-crystal spacing had become small enough to inhibit nucleation in the intervening spaces, presumably due to overlap of diffusion fields. The slope of the increase of crystal number with time in the linear region provided the nucleation rate J_n (Fig. 4.7).

In this study, the start time was difficult to record precisely. This was because, sometimes after the reaction began, a couple of bubbles which formed inside the tubing needed to be expelled before recording could begin. Consequently, the first recorded image could be collected as much as 20 seconds after the real onsite time. Nonetheless, the trend of higher concentrations leading to shorter induction times is clearly shown in Figs. 4.8 and 4.9.

Faster nucleation rates and higher precipitate density were also observed in solutions with higher supersaturation (σ), and a negative linear correlation was found between $\ln(J_n)$ and $1/\sigma^2$, as expected from classical nucleation theory (Fig. 4.10). Nucleation rates measured for the MHA substrates were approximately 4× faster than those observed for MUA for cases where the nucleation rate was surface-promoted. However, the effective interfacial energies evaluated for the two SAMs had similar values (79.0 mJ/m^2 and 82.3 mJ/m^2 for MHA and MUA substrates, respectively). To our knowledge, these are the first direct measurements of calcite nucleation rates on self-assembled monolayer substrates and the first determinations of the interfacial energies of

these.

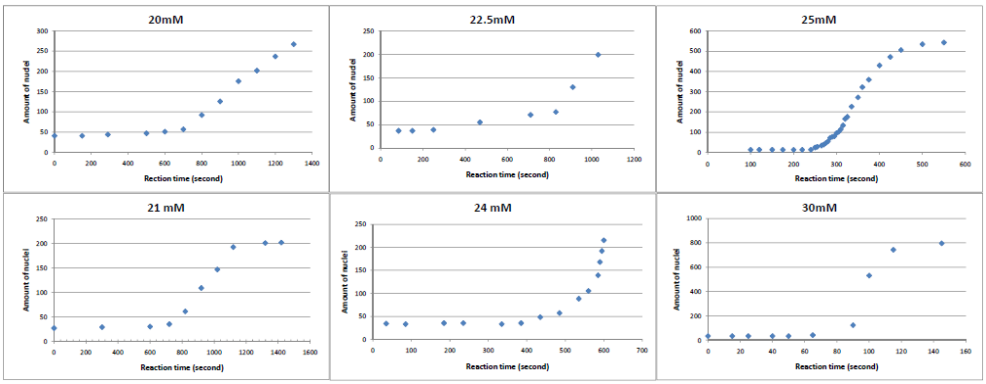

Figure 4.8 Nucleation events on MHA over time

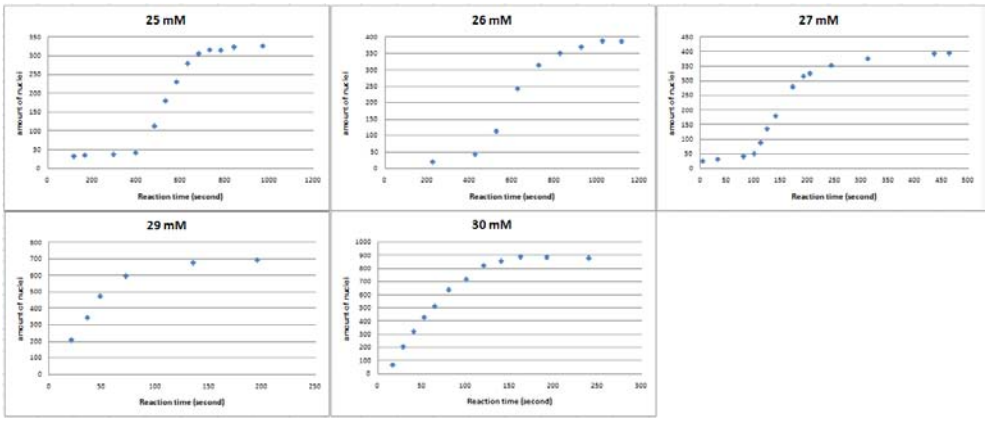

Figure 4.9 Nucleation events on MUA over time

We note that, in the process of learning how to make high-quality MUA films, the first results produced poor orientation control, although we still observed a few dominant orientations. When the nucleation rates were measured and analyzed for these films, we again found an inverse linear dependence between $\ln(J_n)$ and $1/\sigma^2$, but the value of the interfacial energy was distinctly larger. This result shows that, indeed, the SAM itself plays a critical role in determining the interfacial energy and orientation control is tied to the degree to which it is minimized.

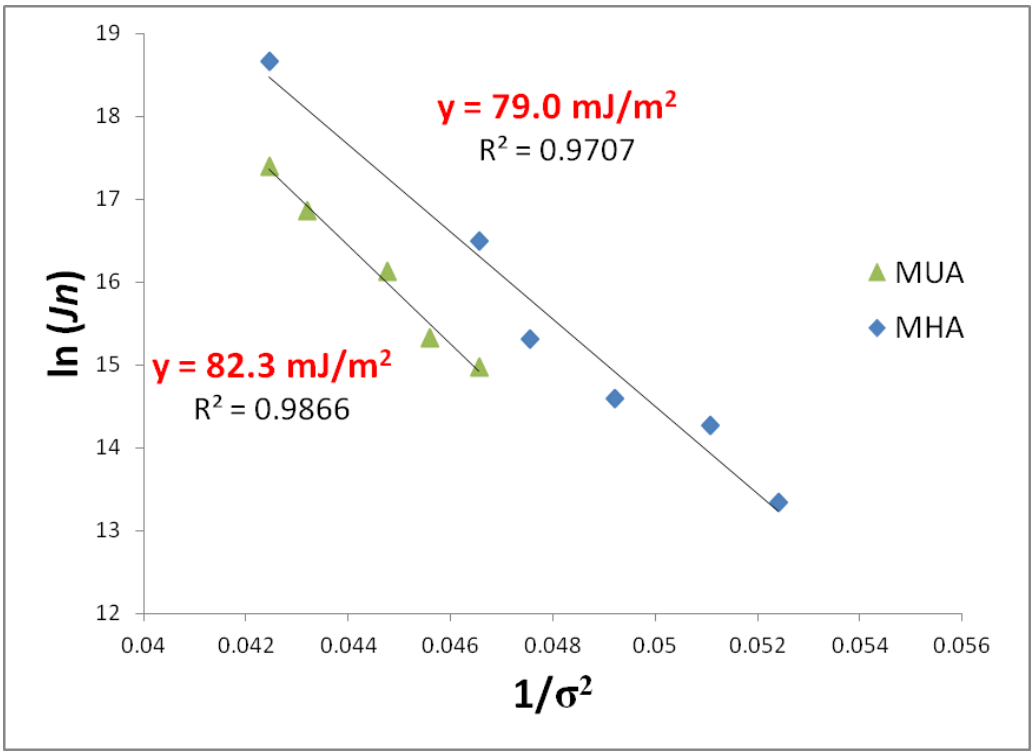

Figure 4.10 Plot showing the natural log of the nucleation rates on MHA and MUA versus the inverse square of supersaturation at room temperature. In the surface-assisted nucleation regime, the slope of the trend line yields effective interfacial energies (α), which is directly proportional to the free energy of nucleus formation Δg.

The values of interfacial energies for the two SAMs are quite similar. Considering the experimental errors and statistical quality of the linear fits (R^2=0.97 and 0.98 for MHA and MUA, a further statistical analysis reveals that the error of the interfacial energies determined here is on the order of 2-3 mJ/m^2), that there is not necessarily a quantifiable difference in the interfacial energy or consequent nucleation barrier for MHA and MUA. Therefore, the different nucleation rates imposed by these odd vs. even SAMs are more likely led by kinetic drivers. The kinetic variability which would affect the factor *A* might be due to (1) attachment and detachment of either ions or small clusters to and from the substrates, (2) rearrangement of clusters on the nuclei and substrates, and (3) differences in local pH and/or ion concentrations near nucleation sites due to the different densities of COO^- functional groups. A similar phenomenon has been reported by Wallace et al. [35], who found that NH^{3+}/COO^-- and COO^--functionalized substrates gave similar slopes for $\ln(J_n)$ and $1/\sigma^2$ but induced significantly different rates of SiO_2 nucleation.

The calculated effective interfacial energies between MHA/MUA and calcite are substantially lower than that between water and calcite on the most stable face (104) (97 mJ/m^2)[36]. This analysis provides a thermodynamic basis for the strong capacity of COOH- terminated SAMs to promote calcite mineralization in a quantitative way. It also suggests a strategy for mineral trapping of CO_2 sequestration based on the use of organic templates as media to accelerate the transformation from CO_2 to carbonate. This study may also help understand the dynamics of calcification widely occurring in calcifying organisms such as coral, oyster, mollusks, etc [37-40].

A number of structural mechanisms for control of orientation and precipitation

rate of crystals by SAMs have been proposed. A common one (1) is a match between the substrate and crystal lattices at the SAM-calcite interface. It is suggested that there is a best geometric match between the patterns of ions adsorbed on the organic surface and those in the nucleating crystal plane, and hence a reduction in the barrier to nucleation on the preferred crystal planes. This suggestion has been supported by both computational simulation and analysis of experimental studies [10, 41-43]. Another proposed mechanism (2) relies on a match of average charge/polarity density [44, 45]. One additional suggested mechanism (3) is that SAMs create a high local concentration near the surface. Aizenberg et al. [46] reported that the polar carboxylic groups exposed on the surface of SAMs could manipulate the gradient of concentrations: they may induce the mass transport of ions to SAMs surfaces, and hence result in faster nucleation rates. Because the results presented here show a clear correlation between interfacial energy and nucleation rate, they are consistent with the first two models, but do not support the third one.

4.4 Conclusions

The effective interfacial energy, which is the fundamental parameter governing nucleation, has been determined for calcite on SAMs for carboxyl- terminated SAMs of odd and even carbon chains by measuring the dependence of nucleation rate for solutions of various concentrations. The results show that MHA and MUA enhance calcite nucleation rates relative to those on bare gold and quartz substrates and induce calcite to nucleate on (012) and (013) faces, respectively. The evaluated effective interfacial energies are 79.0 mJ/m^2 for MHA and 82.3 mJ/m^2 for MUA. These values are significantly lower than that of calcite in bulk solution (97 mJ/m^2). This calculation

provides direct evidence that MHA and MUA enhance calcite nucleation through reducing the thermodynamic barrier to nucleation. Since the interfacial energies are almost the same for MHA and MUA, we have to conclude that the ~4-fold difference in nucleation rates for the two films are due to kinetic factors. In addition, at solute activities below a supersaturation of 0.866 with respect to amorphous calcium carbonate, calcite forms directly and ACC does not represent a precursor phase.

References

1. OBES, *Basic research needs for geosciences: facilitating 21st century energy systems* 2007, Department of Energy, Office of Basic Energy Sciences: Bethesda, Maryland.
2. Mann, S., *Molecular tectonics in biomineralization and biomimetic materials chemistry.* Nature, 1993. **365**(6446): p. 499-505.
3. Bunker, B.C., et al., *Ceramic thin-flim formation on functionalized interfaces through biomimetic processing* Science, 1994. **264**(5155): p. 48-55.
4. Stupp, S.I. and P.V. Braun, *Molecular manipulation of microstructures: Biomaterials, ceramics, and semiconductors.* Science, 1997. **277**(5330): p. 1242-1248.
5. Aizenberg, J., et al., *Crystal progein interactions studied by overgrowth of calcite on biogenic skeletal elements.* Journal of Crystal Growth, 1994. **142**(1-2): p. 156-164.
6. Berman, A., L. Addadi, and S. Weiner, *Interactions of sea-urchin skeleton macromolecules with growing calcite crystals - a study of intracrystalline proteins* Nature, 1988. **331**(6156): p. 546-548.
7. Segvich, S., et al., *Identification of Peptides with Targeted Adhesion to Bone-Like Mineral via Phage Display and Computational Modeling.* Cells Tissues Organs, 2009. **189**(1-4): p. 245-251.
8. Brecevic, L. and A.E. Nielsen, *Solubility of amorphous calcium carbonate.* Journal of Crystal Growth, 1989. **98**(3): p. 504-510.
9. Travaille, A.M., et al., *Aligned Growth of Calcite Crystals on a Self-Assembled Monolayer.* Advanced Materials, 2002. **14**(7): p. 492.
10. Han, Y.-J. and J. Aizenberg, *Face-Selective Nucleation of Calcite on Self-Assembled Monolayers of Alkanethiols: Effect of the Parity of the Alkyl Chain.* Angewandte Chemie International Edition, 2003. **42**(31): p. 3668-3670.
11. Travaille, A.M., et al., *Highly oriented self-assembled monolayers as templates for epitaxial calcite growth.* Journal of the American Chemical Society, 2003. **125**(38): p. 11571-11577.

12. Han, T.Y.-J. and J. Aizenberg, *Calcium carbonate storage in amorphous form and its template-induced crystallization.* Chemistry of Materials, 2007. **20**(3): p. 1064-1068.
13. Li, H. and L.A. Estroff, *Hydrogels coupled with self-assembled monolayers: an in vitro matrix to study calcite biomineralization.* Journal of the American Chemical Society, 2007. **129**(17): p. 5480-5483.
14. Addadi, L., S. Raz, and S. Weiner, *Taking advantage of disorder: Amorphous calcium carbonate and its roles in biomineralization.* Advanced Materials, 2003. **15**(12): p. 959-970.
15. Weiss, I.M., et al., *Mollusc larval shell formation: Amorphous calcium carbonate is a precursor phase for aragonite.* Journal of Experimental Zoology, 2002. **293**(5): p. 478-491.
16. Loosanoff, V.L., W.S. Miller, and P.B. Smith, *Growth and setting of larvae of venus-mercenaria in relation to temperature.* Journal of Marine Research, 1951. **10**(1): p. 59-81.
17. Beniash, E., et al., *Amorphous calcium carbonate transforms into calcite during sea urchin larval spicule growth.* Proceedings of the Royal Society of London Series B-Biological Sciences, 1997. **264**(1380): p. 461-465.
18. Politi, Y., et al., *Sea urchin spine calcite forms via a transient amorphous calcium carbonate phase.* Science, 2004. **306**(5699): p. 1161-1164.
19. Colfen, H. and S. Mann, *Higher-order organization by mesoscale self-assembly and transformation of hybrid nanostructures.* Angewandte Chemie-International Edition, 2003. **42**(21): p. 2350-2365.
20. Lee, J.R.I., et al., *Structural development of mercaptophenol self-assembled monolayers and the overlying mineral phase during templated CaCO3 crystallization from a transient amorphous film.* Journal of the American Chemical Society, 2007. **129**(34): p. 10370-10381.
21. Raz, S., et al., *The transient phase of amorphous calcium carbonate in sea urchin larval spicules: The involvement of proteins and magnesium ions in its formation and stabilization.* Advanced Functional Materials, 2003. **13**(6): p. 480-486.
22. Tester, C.C., et al., *In vitro synthesis and stabilization of amorphous calcium carbonate (ACC) nanoparticles within liposomes.* Crystengcomm, 2011. **13**(12): p. 3975-3978.
23. Xu, G.F., et al., *Biomimetic synthesis of macroscopic-scale calcium carbonate thin films. Evidence for a multistep assembly process.* Journal of the American Chemical Society, 1998. **120**(46): p. 11977-11985.
24. Johnston, J., H.E. Merwin, and E.D. Williamson, *The several forms of calcium carbonate.* American Journal of Science, 1916. **41**(246): p. 473-512.
25. Koga, N., Y.Z. Nakagoe, and H. Tanaka, *Crystallization of amorphous calcium carbonate.* Thermochimica Acta, 1998. **318**(1-2): p. 239-244.
26. Huang, S.C., K. Naka, and Y. Chujo, *A carbonate controlled-addition method for amorphous calcium carbonate spheres stabilized by poly(acrylic acid)s.* Langmuir, 2007. **23**(24): p. 12086-12095.
27. Kitamura, M., *Crystallization and transformation mechanism of calcium carbonate polymorphs and the effect of magnesium ion.* Journal of Colloid and Interface Science, 2001. **236**(2): p. 318-327.

28. Allison, J.D., D.S. Brown, and K.J. Novo-Gradac, *MINTEQA2/PRODEFA2, a geochemical assessment model for environmental systems: Version 3. 0 user's manual,* in *US Environmental Protection Agency, Athens, GA*. 1991. p. 117
29. Aizenberg, J., A.J. Black, and G.M. Whitesides, *Oriented growth of calcite controlled by self-assembled monolayers of functionalized alkanethiols supported on gold and silver.* Journal of the American Chemical Society, 1999. **121**(18): p. 4500-4509.
30. Rull Perez, F. and J. Martinez-Frias, *Identification of calcite grains in the Vaca Muerta mesosiderite by Raman spectroscopy.* Journal of Raman Spectroscopy, 2003. **34**(5): p. 367-370.
31. Urmos, J., S.K. Sharma, and F.T. Mackenzie, *Characterization of some biogenic carbonates with Raman spectroscopy.* American Mineralogist, 1991. **76**(3-4): p. 641-646.
32. Raz, S., et al., *Stable amorphous calcium carbonate is the main component of the calcium storage structures of the Crustacean Orchestia cavimana.* Biol Bull, 2002. **203**(3): p. 269-274.
33. De Yoreo, J.J. and P.G. Vekilov, *Principles of Crystal Nucleation and Growth.* Reviews in Mineralogy and Geochemistry, 2003. **54**(1): p. 57-93.
34. Cossaro, A., et al., *X-ray diffraction and computation yield the structure of alkanethiols on gold(111).* Science, 2008. **321**(5891): p. 943-946.
35. Wallace, A.F., J.J. DeYoreo, and P.M. Dove, *Kinetics of silica nucleation on carboxyl- and amine-terminated surfaces: insights for biomineralization.* American Chemical Society, 2009. **131**: p. 5244–5250.
36. Söhnel, O., *Electrolyte Crystal-Aqueous Solution Interfacial Tensions from Crystallization Data.* Journal of Crystal Growth, 1982. **57**(1): p. 101-108.
37. Kleypas, J.A., et al., *Geochemical consequences of increased atmospheric carbon dioxide on coral reefs.* Science, 1999. **284**(5411): p. 118-120.
38. Meldrum, F.C., *Calcium carbonate in biomineralisation and biomimetic chemistry.* International Materials Reviews, 2003. **48**(3): p. 187-224.
39. Addadi, L., et al., *Mollusk shell formation: A source of new concepts for understanding biomineralization processes.* Chemistry-a European Journal, 2006. **12**(4): p. 981-987.
40. Gazeau, F., et al., *Impact of elevated CO_2 on shellfish calcification.* Geophysical Research Letters, 2007. **34**(7).
41. Pokroy, B., V.F. Chernow, and J. Aizenberg, *Crystallization of Malonic and Succinic Acids on SAMs: Toward the General Mechanism of Oriented Nucleation on Organic Monolayers†.* Langmuir, 2009. **25**(24): p. 14002-14006.
42. Duffy, D.M., et al., *Effect of Bicarbonate Ions on the Crystallization of Calcite on Self-Assembled Monolayers.* The Journal of Physical Chemistry B, 2005. **109**(12): p. 5713-5718.
43. Kuther, J., et al., *Templated crystallisation of calcium and strontium carbonates on centred rectangular self-assembled monolayer substrates.* Chemistry-a European Journal, 1998. **4**(9): p. 1834-1842.
44. Volkmer, D., et al., *Elucidating the role of charge density on the growth of CaCO3 crystals underneath calix 4 arene monolayers.* Materials Science & Engineering C-Biomimetic and Supramolecular Systems, 2005. **25**(2): p. 161-167.

45. Fricke, M. and D. Volkmer, *Crystallization of calcium carbonate beneath insoluble monolayers: Suitable models of mineral-matrix interactions in biomineralization?*, in *Biomineralization I: Crystallization and Self-Organization Process*, K. Naka, Editor. 2007, Springer-Verlag Berlin: Berlin. p. 1-41.
46. Aizenberg, J., A.J. Black, and G.M. Whitesides, *Control of crystal nucleation by patterned self-assembled monolayers.* Nature, 1999. **398**(6727): p. 495-498.

CHAPTER FIVE
CONCLUSIONS

This thesis addresses how different factors affect the formation process and properties of $CaCO_3$, the most common biogenetic mineral, in order to obtain a better understanding of biomineralization and industry applications of $CaCO_3$ in general. The results reveal that both inorganic additives (ammonium) and organic templates (SAMs) can control the polymorphism, morphology, and formation rate of $CaCO_3$ precipitates. Ammonium is capable of promoting the formation of vaterite over calcite but only if its concentration in the growth solution is above a certain threshold. The material of the reaction container, *e.g.*, Petri dish, also affects the polymorph composition of $CaCO_3$ precipitates. In the presence of ammonium, Petri dishes made of polystyrene promote the development of vaterite more than that of glass does. This is one indication how the interplay between growth substrate and solution composition together influence the formation of specific polymorphs (neither ammonium nor polystyrene substrates alone result in a high yield of vaterite formation). Therefore, when applying the NH_3-diffusion method to form only calcite, the experiments have to be carefully designed to minimize the amount of ammonium, especially if the influence of other growth modifiers is studied. Otherwise, it may be difficult to differentiate the actual reason for the formation of vaterite, be it the presence of ammonium, or of other modifiers that were actually studied.

The results of this study indicate that it may be worth exploring whether ammonium plays a similar role in carbonate precipitation in nature, for example in soils with extensive protein decomposition and in or near plants that nitrifying bacteria frequently associate with. In addition, the results imply that other species of ions comparable to ammonium might possess the same functions, *e.g.*, potassium that has the same charge and similar ionic radius as ammonium.

Vaterite was typically considered to develop various morphologies under different growth conditions. The work presented here on the growth sequence, however, suggests that (1) vaterite grains are always polycrystals composed of nano-clusters and that (2) the numerous morphologies may be just intermediate stages of the same growth process, which is an assemblage of nano-clusters in an increasingly organized way. Because of certain limitations caused by the growth environment, such as the change in supersaturation and growth inhibitor composition and concentration, vaterite is not always able to develop into the final stage, which in this case was typically a hexagonal flower-like array. The imperfect assemblage of nano-clusters might be the reason for inhibiting single crystals of vaterite to expand to a larger scale and for causing a high dislocation density inside vaterite. This study provides a method of vaterite design to have some control over specific morphologies and of different densities of dislocations, which lead to certain properties that can be important in specific industrial applications (*e.g.*, cement and paper manufacturing).

SAMs, a simple model of organic template, have proven to be able to control the nucleation rate and orientation of calcite precipitates. Specifically, MHA and MUA enhance calcite nucleation on (012) and (013) faces, respectively, by minimizing the

interfacial energy. However, the difference in nucleation rates between MHA and MUA are caused by kinetic factors. This analysis provides a thermodynamic basis for the strong capacity of COOH- terminated SAMs to promote calcite mineralization in a quantitative way; specifically, these SAMs reduce the interface free energy by about a factor of two compared to the water-calcite interface. This finding may aid in the design of optimized mineral trapping during CO_2 sequestration that applies organic templates as media to accelerate the transformation from CO_2 to carbonate. Another significant discovery of this research is that amorphous calcium carbonate (ACC) does not always form as the precursor of crystallized $CaCO_3$ phases on SAMs. At solute activities below or slightly above the solubility limit of amorphous calcium carbonate, calcite forms directly. This result may help understand the pathway of carbonate mineralization on organic matrices, for example, the calcification occurring widely in calcifying organisms such as corals, oysters, and mollusks.